




This is to certify that the
dissertation entitled
**THREE-LEVEL AND FOUR-LEVEL INFRARED-INFRARED
DOUBLE RESONANCE SPECTROSCOPY IN CH₃F**

presented by

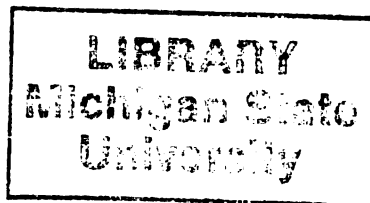
QUAN SONG

has been accepted towards fulfillment
of the requirements for

Ph. D. degree in CHEMISTRY


Major professor

Date May 28, 1992



**PLACE IN RETURN BOX to remove this checkout from your record.
TO AVOID FINES return on or before date due.**

DATE DUE	DATE DUE	DATE DUE
_____	_____	_____
_____	_____	_____
_____	_____	_____
_____	_____	_____
_____	_____	_____
_____	_____	_____
_____	_____	_____

MSU is An Affirmative Action/Equal Opportunity Institution

c:\circ\datedue.pm3-p.1

**THREE-LEVEL AND FOUR-LEVEL INFRARED-INFRARED
DOUBLE RESONANCE SPECTROSCOPY IN CH₃F**

By

Quan Song

A DISSERTATION

Submitted to
Michigan State University
in partial fulfillment of the requirements
for the degree of

DOCTOR OF PHILOSOPHY

Department of Chemistry

1992

1998-0661

ABSTRACT

THREE-LEVEL AND FOUR-LEVEL INFRARED-INFRARED DOUBLE RESONANCE SPECTROSCOPY IN CH₃F

By

Quan Song

A series of three-level and four-level infrared-infrared (IR-IR) double resonance experiments have been carried out to study saturation spectroscopy, to characterize various features of collisionally-induced transitions, to determine the vibration rotation energies of a highly excited vibrational state, and to measure the precise frequencies of rovibrational transitions in methyl fluoride. In these experiments, either a fundamental rovibrational transition, or a hot band transition in the ν_3 vibrational mode of CH₃F was pumped by a CO₂ laser coincidence while rovibrational transitions, involving excitation of either the ν_3 or the ν_6 vibrational mode, were probed by an infrared microwave sideband laser system.

Dynamic Stark splitting (Rabi splitting) has been observed in three-level IR-IR double resonance in CH₃F. The line shape has been fit to theoretical expressions that were derived from a semi-classical treatment of a three-level system. A very good agreement between theory and experiment has been obtained.

Rotation and vibration-rotation transitions in CH₃F induced by collision with foreign gases such as H₂, He, Ar, Xe or isotopically-labeled CH₃F have been studied by the method of four-level IR-IR double resonance. All of the observed transitions obey selection rules. It has been found that Ar or Xe can collisionally-induce direct vibrational transitions in CH₃F more readily than CH₃F itself.

Classical elastic scattering theory has been used to calculate one-dimensional collision kernels with Lennard-Jones and Buckingham-Slater intermolecular potential functions. The results of the calculations demonstrate most of the qualitative features observed in experiments.

Initial velocity dependence of the collisionally-induced rotational energy transfer in CH_3F has been studied. It has been found that the r.m.s. velocity change increases as the relative r.m.s. velocity of the colliding molecules increases. Velocity dependence of the rates of rotational energy transfer has also been observed.

IR-IR double resonance spectroscopy has been used to observe vibration-rotation transitions in the $3\nu_3 - 2\nu_3$ hot band of $^{12}\text{CH}_3\text{F}$. Six transitions in this band have been observed and assigned. The Doppler-free feature of IR-IR double resonance line shapes has been employed to obtain precise center frequencies for a number of transitions in CH_3F .

DEDICATION

TO

My parents and my family

ACKNOWLEDGMENTS

I would like to thank Professor Richard H. Schwendeman for his kindly help and encouragement throughout these studies and during the preparation of the thesis.

My thanks are extended to the members of this group for their stimulating discussions and friendship.

Finally, I would like to thank my parents and my family for their support and encouragement.

TABLE OF CONTENTS

CONTENT	PAGE
LIST OF TABLES	vi
LIST OF FIGURES	vii
CHAPTER 1. OVERVIEW	1
References	8
 CHAPTER 2. OBSERVATION OF THE DYNAMIC STARK SPLITTING IN THREE-LEVEL INFRARED-INFRARED DOUBLE RESONANCE	10
I. Introduction	10
II. Theoretical Part	12
III. Experimental Part	18
IV. Results and Discussion	22
A. Observation of the dynamic Stark splitting	22
B. Determination of Rabi frequency	26
C. The criteria for observing the dynamic Stark splitting	28
D. Precise determination of a laser offset frequency	31
V. Conclusion	34
VI. Appendix: Algebraic Solution For A Three-level System	35
References	44

CHAPTER 3. COLLISIONALLY INDUCED ROTATIONAL AND VIBRATIONAL ENERGY TRANSFER OF METHYL FLUORIDE IN FOREIGN GASES	46
I. Introduction	46
II. Experimental Details	50
III. Theoretical Detail	51
IV. Experimental Results	57
A. Foreign gas effects on the double resonance lineshape	57
B. Selection rule for direct rotational energy transfer	61
C. Vibrational energy transfer from $v_3=1$ to $v_6=1$ vibrational state	65
D. Center frequency shift in double resonance spectra	72
V. Theoretical Collision Kernels	74
A. Collision kernel for dipolar-dipolar collision	76
B. Collision kernels for dipolar-nonpolar collision	78
References	82
 CHAPTER 4. THE EFFECT OF INITIAL VELOCITY ON ROTATIONAL ENERGY TRANSFER IN $^{13}\text{CH}_3\text{F}$	 86
I. Introduction	86
II. Theoretical Part	89
A. Relative velocity of the colliding molecule	89
B. Velocity change upon collision	90
III. Experimental Detail	92
IV. Results and Discussion	96

A. Three-level double resonance at different pump laser offsets	96
B. Initial velocity dependence of the r.m.s. velocity change upon collision	99
C. Velocity dependence of rates of energy transfer	104
D. Calculation from classical scattering theory	107
References	109
 CHAPTER 5. STUDY OF THE $3\nu_3 - 2\nu_3$ BAND IN $^{12}\text{CH}_3\text{F}$ AND DOPPLER-FREE FREQUENCIES IN $^{12}\text{CH}_3\text{F}$ AND $^{13}\text{CH}_3\text{F}$	110
I. Introduction	110
II. Theoretical Background	113
A. Energy levels in a non-degenerate vibrational mode in $^{12}\text{CH}_3\text{F}$	113
B. Precise measurement of pump laser offset frequency	114
III. Experimental Detail	116
IV. Results and Discussion	120
A. Observation and assignment of the $3\nu_3 - 2\nu_3$ band in $^{12}\text{CH}_3\text{F}$	120
B. Rotational constants in the $\nu_3=3$ vibrational state of $^{12}\text{CH}_3\text{F}$	127
C. Collisionally induced energy transfer in the $\nu_3=2$ state	131
D. Precise frequencies in CH_3F	134
V. Conclusion	137
References	139

LIST OF TABLES

TABLE	PAGE
2.1. Pump and probe transitions used for double resonance in Chapter 2.	23
3.1. Pump and probe transitions used for double resonance in Chapter 3.	52
4.1. Pump and probe transitions used for double resonance in Chapter 4.	97
4.2. Transferred spikes for different pumping offsets in $^{13}\text{CH}_3\text{F}$.	103
4.3. Velocity change during state change upon collision in $^{13}\text{CH}_3\text{F}$.	105
4.4. Relative intensities for collisionally-induced transitions in $^{13}\text{CH}_3\text{F}$.	106
5.1. Pump and probe transitions in the $2\nu_3 - \nu_3$ band of $^{12}\text{CH}_3\text{F}$.	117
5.2. Comparison of observed and calculated frequencies in $^{12}\text{CH}_3\text{F}$.	123
5.3. Vibration-rotation parameters for the $3\nu_3 - 2\nu_3$ band in $^{12}\text{CH}_3\text{F}$.	130
5.4. Precise frequencies of transitions in CH_3F .	136
5.5. Comparison of frequencies of transitions in CH_3F .	138

LIST OF FIGURES

FIGURE		PAGE
2.1.	Four possible energy arrangements for three-level double resonance. In each case the bold arrow represents the pump beam of frequency ν_1 and the light arrow represents the probe beam of the frequency ν_2 . The s_1 and s_2 are sign factors used in the equations in the appendix.	14
2.2.	Block diagram of infrared-infrared double resonance spectrometer. M = mirror; L = lens; PZT = piezoelectric translator; STAB = fluorescence detector and laser stabilization circuitry; BS = beam splitter; MOD = CdTe electro-optic modulator crystal; POL = polarizer; TWTA = traveling wave tube microwave amplifier; PIN = PIN diode electronically-controlled modulation attenuator; DET = infrared detector; PSD = phase sensitive detector; MOD = 33 kHz square-wave generator; A/D = analog digital converter	20
2.3.	Three-level double resonance spectra for $^{13}\text{CH}_3\text{F}$ recorded at three different sample pressures and 2.2 W infrared power. The $^Q\text{R}(4,3)$ transition in the ν_3 band was pumped and the $^Q\text{P}(5,3)$ transition in the $2\nu_3 - \nu_3$ band was probed. The lasers used are given in Table 2.1. The horizontal axis is the probe laser frequency minus 30093553.09 MHz. The residuals from the least squares fittings of the lineshapes are shown at the bottom of the figure.	25
2.4.	Three-level double resonance spectra for $^{13}\text{CH}_3\text{F}$ recorded at two different infrared powers and a sample pressure of 2.5 mTorr. The pump and probe transitions, the lasers and the horizontal axis are the same as in Fig. 2.3. The residuals from the least squares fittings of the lineshapes are shown at the bottom of the figure.	27

- 2.5. Plot of the vibrational contribution to the Rabi frequency x_p for the spectra shown in Fig. 2.4. and three additional spectra for the same transition recorded at different powers. The straight line is the least-squares fit of the five points constrained to go through zero. The slope of the line is 5.47 MHz W^{-1/2}. 29
- 2.6. Three level double resonance spectrum for ¹²CH₃F. The ^QQ(12, 2) transition in the ν_3 band was pumped and the ^QR(12, 2) transition in the $2\nu_3 - \nu_3$ band was probed. The lasers used are given in Table 2.1. The horizontal axis is the probe laser frequency minus 31556028.88 MHz. The pump power density was ~ 4 W/cm² and the sample pressure was 6 mTorr. The residual from the least squares fitting is shown below the spectrum. 30
- 2.7. Three-level double resonance spectrum for ¹²CH₃F. The ^QR(11,9) transition in the ν_3 band was pumped and the ^QQ(12, 9) transition in the $2\nu_3 - \nu_3$ band was probed. The lasers used are given in Table 2.1. The horizontal axis is the probe laser frequency minus 30913915.43 MHz. The pump power density was ~ 3 W/cm² and the sample pressure was 2 mTorr. 32
- 2.8. Three-level double resonance spectrum for ¹²CH₃F. The ^QR(11,9) transition in the ν_3 band was pumped and the ^QR(12, 9) transition in the $2\nu_3 - \nu_3$ band was probed. The lasers used are given in Table 2.1. The horizontal axis is the probe laser frequency minus 31558028.88MHz. The pump power density was ~ 3 W/cm² and the sample pressure was 2 mTorr. 32
- 2.9. Two-level double resonance spectrum for ¹³CH₃F. The ^QR(4, 3) transition in the ν_3 band was both pumped and probed. The pump and probe lasers used are given in Table 2.1. The horizontal axis is the probe laser frequency minus 31043009.23 MHz. The pump power

density was $\sim 4 \text{ W/cm}^2$ and the sample pressure was 3.5 mTorr. The residual from a least squares fitting of the lineshape is shown at the bottom of the figure.

33

- 3.1 Diagram of the scattering plane for a single scattering event between an active molecule (a) and a perturber (p). The curved path of the active molecule is symmetric about the line that makes an angle θ_m with the -z axis. In the figure, $\Theta = \pi - 2\theta_m$ is the scattering angle; r^0 is the initial separation of a and p; v^0 is the initial relative velocity; b, which is parallel to the y axis, is the magnitude of the impact parameter; and χ is the angle between b and a line (N) that is parallel to the line of nodes.

54

- 3.2 Spectra of the $Q_P(6,3)$ transition in the $2\nu_3 - \nu_3$ band in $^{13}\text{CH}_3\text{F}$ taken for a variety of collision partners; the spike and Gaussian components for each lineshape are also shown. Trace (a) is a single resonance spectrum in a pure sample at 7 mTorr; Traces (b) - (f) are double resonance spectra recorded while the $Q_R(4,3)$ transition in the ν_3 band was pumped. The samples for the double resonance spectra were 3 mTorr of $^{13}\text{CH}_3\text{F}$ in 50 mTorr of foreign gas, as follows: (b) $^{12}\text{CH}_3\text{F}$; (c) H_2 ; (d) He; (e) Ar; (f) Xe. The infrared frequencies for each spectrum are the horizontal axis values shown for (e) plus 30 041 529 MHz.

59

- 3.3. Energy level diagram for $^{13}\text{CH}_3\text{F}$ for the double resonance transitions shown in Fig. 3.4. Only the levels for $4 \leq J \leq 8$ and $0 \leq K \leq 6$ in $\nu_3 = 1$ are shown.

63

- 3.4. Single resonance (a) and double resonance (b-d) spectra of the $Q_P(7,K)$ transitions for $K \leq 6$ in the $2\nu_3 - \nu_3$ band of $^{13}\text{CH}_3\text{F}$. The $Q_R(4,3)$ transition in the ν_3 band of $^{13}\text{CH}_3\text{F}$ was pumped for the double resonance. The samples were: (a) $^{13}\text{CH}_3\text{F}$ at 30 mTorr; (b) $^{13}\text{CH}_3\text{F}$ at 17 mTorr; (c) 1 mTorr $^{13}\text{CH}_3\text{F}$ in 100 mTorr $^{12}\text{CH}_3\text{F}$; and (d) 1 mTorr $^{13}\text{CH}_3\text{F}$ in 100 mTorr Ar. The infrared frequencies for each spectrum

are the horizontal axis value plus 29 989 650 MHz.

64

- 3.5. Single resonance (a) and double resonance (b) spectra of the $Q_P(14,K)$ transitions for $K \leq 5$ in the $2\nu_3 - \nu_3$ band of $^{12}\text{CH}_3\text{F}$. The $Q_Q(12,1)$ and $Q_Q(12,2)$ transitions in the ν_3 band of $^{12}\text{CH}_3\text{F}$ were simultaneously pumped for the double resonance. The samples were: (a) 30 mTorr $^{12}\text{CH}_3\text{F}$; and (b) 1% $^{12}\text{CH}_3\text{F}$ in Ar at 140 mTorr total pressure. The infrared frequencies for each spectrum are the horizontal axis values plus 30 199 026 MHz.

66

- 3.6. Single resonance (a) and double resonance (b-d) spectra of the $Q_R(9,3,1)$ and $Q_R(10,2,-1)$ transitions in the $\nu_3 + \nu_6 - \nu_6$ band of $^{12}\text{CH}_3\text{F}$. The $Q_Q(12,1)$ and $Q_Q(12,2)$ transitions in the ν_3 band of $^{12}\text{CH}_3\text{F}$ were simultaneously pumped for the double resonance in (b) and (d), whereas the $Q_R(11,9)$ transition in the ν_3 band of $^{12}\text{CH}_3\text{F}$ was pumped for (c). The samples were: $^{12}\text{CH}_3\text{F}$ at 500 mTorr for (a); 1% $^{12}\text{CH}_3\text{F}$ in 63 mTorr total pressure of Ar for (b) and (c); and 1% $^{12}\text{CH}_3\text{F}$ in 63 mTorr total pressure of $^{13}\text{CH}_3\text{F}$ for (d). The infrared frequency for the $Q_R(9,3,1)$ transition is 31 632 843 MHz minus the horizontal axis value, whereas the infrared frequency for the $Q_R(10,2,-1)$ transition is 31 660 843 MHz plus the horizontal axis value.

68

- 3.7. Single resonance (a) and double resonance spectra (b) of the transitions shown in Fig. 7. The spectrum in (a) is the same as that in Fig. (7a). The spectrum in (b) was recorded for 60 mTorr of $^{12}\text{CH}_3\text{F}$ while the $Q_Q(12,1)$ and $Q_Q(12,2)$ transitions in the ν_3 band of $^{12}\text{CH}_3\text{F}$ were simultaneously pumped.

70

- 3.8. Single resonance (a) and double resonance (b) spectra of the $Q_R(7,1,-1)$ transition in the $\nu_3 + \nu_6 - \nu_6$ band and the $Q_R(12,K)$ transitions for $K \leq 9$ in the $2\nu_3 - \nu_3$ band of $^{12}\text{CH}_3\text{F}$. The $Q_Q(12,1)$ and $Q_Q(12,2)$ transitions in the ν_3 band of $^{12}\text{CH}_3\text{F}$ were simultaneously pumped for (b). The sample pressures were 250 mTorr (a) and 60 mTorr (b). The infrared frequencies for the $Q_R(12,K)$ transitions are the horizontal axis

values plus 31 556 029 MHz, whereas the infrared frequency for the $Q_R(7,1,-1)$ transition is 31 532 029 MHz minus the horizontal axis value.

71

- 3.9. Single resonance (a) and double resonance (b) spectra of the $Q_P(5,3)$ transition in the ν_3 band of $^{13}\text{CH}_3\text{F}$. The $Q_R(4,3)$ transition in $^{13}\text{CH}_3\text{F}$ was pumped for the double resonance. The samples were 5 mTorr of $^{13}\text{CH}_3\text{F}$ in 5 Torr of Ar for both spectra. The infrared frequencies for each spectrum are the horizontal axis value plus 31 089 492 MHz.

73

- 3.10. (a) One-dimensional collision kernel as a function of final velocity calculated as the sum of two Keilson-Storer functions. The β values for the two functions are 19.1 m/s and 140.5 m/s and the ratio of the A values is $A(\text{broad})/A(\text{narrow}) = 0.185$. (b) One-dimensional classical collision kernel calculated by the procedure described in the text, The parameters for the calculation are: $m = 35$ u for the active molecule and the perturber; $\epsilon/k_B = 300$ K; $r_e = 3.5 \text{ \AA}$; $0 \leq b \leq 10 \text{ \AA}$; number of collisions = 20 000. The initial velocity for both kernels was 234 m/s. The vertical axes have been scaled for convenient plotting and comparison.

77

- 3.11. One-dimensional classical collision kernels as a function of final velocity calculated by the procedure described in the text. The parameters are: $\epsilon/k_B = 100$ K; $r_e = 4 \text{ \AA}$; $0 \leq b \leq 4 \text{ \AA}$; number of collisions = 40 000; $m(\text{active molecule}) = 35$ u; $m(\text{perturber}) = 4$ u (a) or 131.3 u (b). The initial velocity for both kernels was 234 m/s. The vertical axes have been scaled for plotting, but are relatively correct for the two plots.

79

- 3.12. One -dimensional classical collision kernels as a function of final velocity calculated by the procedure described in the text. The parameters are: $\epsilon/k_B = 100$ K; $0 \leq b \leq 4 \text{ \AA}$; $m(\text{active molecule}) = 35$ u; $m(\text{perturber}) = 4$ u; number of collisions = 40 000; and $r_e = 4 \text{ \AA}$ (a) or

- 3.5 Å⁰ (b). The initial velocity for both kernels was 234 m/s. The vertical axes have been scaled for plotting, but are relatively correct for the two plots. 80
- 3.13. One-dimensional classical collision kernel as a function of final velocity calculated by the procedure described in the text. The parameters are: $\epsilon/k_B = 100$ K; $r_e = 4$ Å⁰; $0 \leq b \leq 3$; $m(\text{active molecule}) = 35$ u; $m(\text{perturber}) = 131.3$ u; initial velocity = 234 m/s; number of collisions = 30 000. The vertical axis has been scaled. 81
- 4.1. Set up for stabilization of CO₂ laser to a Stark Lamb dip. M = mirror; PZT = piezoelectric translator and laser output coupling mirror; B.S. = beam splitter; FG1, FG2 = function generators; S.M.B. = signal mixing box; HVA = high voltage amplifier; HVP = high voltage power supply; PRM = 90% partially reflecting mirror; DET = detector; PREAMP = preamplifier; OPS = operational power supply; OSC = oscilloscope. 94
- 4.2. Comparison of three-level double resonance effects observed with three different pump laser offsets. The $Q_{R(4,3)}$ transition in the ν_3 hot band was pumped and the $Q_{P(5,3)}$ transition in $2\nu_3 - \nu_3$ band was probed. The lasers used are given in Table 4.1. The horizontal axis is the probe laser frequency minus 30093553.09 MHz. 98
- 4.3. Comparison of four-level double resonance effects observed with different pump laser offsets (8.6, 23.1 and 37.8 MHz from left to right). The $Q_{R(4,3)}$ transition in the ν_3 band was pumped and the $Q_{P(7,3)}$ transition in $2\nu_3 - \nu_3$ hot band was probed. The lasers used are given in Table 4.1. The horizontal axis is the probe laser frequency minus 29988650.09 MHz. 100
- 4.4. Comparison of the line shape of the transferred spike observed with pump laser offset at 37.8 MHz (upper) to that at 8.6 MHz (lower). The

- Gaussian part was removed. The $Q_R(4,3)$ transition in the ν_3 band was pumped and the $Q_P(7,3)$ transition in the $2\nu_3 - \nu_3$ hot band was probed. The lasers used are given in Table 4.1. The upper spectrum has been shifted in frequency for comparison. The horizontal axis is the probe laser frequency minus 30041528.73 MHz. 101
- 5.1. The geometry for the copropagating double resonance experiment. M = mirror; POL = polarizer; DET = detector. The planes of polarization of the pump and probe lasers were perpendicular to one another. 119
- 5.2. Four level double resonance spectrum for the $Q_R(8,6)$ transition in the $3\nu_3 - 2\nu_3$ band in $^{12}\text{CH}_3\text{F}$. The $Q_R(13,6)$ transition in the $2\nu_3 - \nu_3$ band was pumped. The horizontal axis is the offset frequency of the probe laser with the GHz part removed. The pump and probe lasers used are given in Table 5.2. 122
- 5.3. Four level double resonance spectrum for the $Q_R(10,6)$ transition in the $3\nu_3 - 2\nu_3$ band in $^{12}\text{CH}_3\text{F}$. The $Q_R(13,6)$ transition in the $2\nu_3 - \nu_3$ band was pumped. The horizontal axis is the offset frequency of the probe laser with the GHz part removed. The pump and probe lasers used are given in Table 5.2. 124
- 5.4. Double resonance spectrum for the $Q_R(8,0)$, $Q_R(8,3)$ and $Q_R(8,6)$ transitions in the $3\nu_3 - 2\nu_3$ band in $^{12}\text{CH}_3\text{F}$. The $Q_R(7,3)$ transition in the $2\nu_3 - \nu_3$ band was pumped. The horizontal axis is the offset frequency of the probe laser with the GHz part removed. The pump and probe lasers used are given in Table 5.2. The $Q_R(8,6)$ transition is overlapped with the $Q_R(9,9)$ transition in the $2\nu_3 - \nu_3$ band. 125
- 5.5. Four level double resonance spectrum for the $Q_R(10,0)$, $Q_R(10,3)$ and $Q_R(10,6)$ transitions in the $3\nu_3 - 2\nu_3$ band in $^{12}\text{CH}_3\text{F}$. The $Q_R(7,3)$ transition in the $2\nu_3 - \nu_3$ band was pumped. The horizontal axis is the offset frequency of the probe laser with GHz part removed. The pump

- and probe lasers used are given in Table 5.2. 126
- 5.6. Three-level double resonance spectrum for the $Q_R(7,3)$ pump transition in the $2\nu_3 - \nu_3$ band and the $Q_R(8,3)$ probe in the $3\nu_3 - 2\nu_3$ band in $^{12}\text{CH}_3\text{F}$. The spectrum was recorded with a setup with which double resonance effects for both counter-propagating and copropagating pump beams could be seen in the same scan. The horizontal axis is the offset frequency of the probe laser with the GHz part removed. The pump and probe lasers used are given in Table 5.2. 128
- 5.7. Double resonance spectrum for the $Q_Q(9,K)$ ($K=3, 4, 5, 6$) transitions in the $2\nu_3 - \nu_3$ band in $^{12}\text{CH}_3\text{F}$. The $Q_R(7,3)$ transition in the $2\nu_3 - \nu_3$ band was pumped. The horizontal axis is the offset frequency of the probe laser with the GHz part removed. The pump and probe lasers used are given in Table 5.1. 133
- 5.8. Counterpropagating and copropagating three-level double resonance spectra for the $Q_R(12,1)$ and $Q_R(12,1)$ transitions in the $2\nu_3 - \nu_3$ band when the $Q_Q(12,1)$ and the $Q_Q(12,2)$ transitions in the ν_3 fundamental in $^{12}\text{CH}_3\text{F}$ are simultaneously pumped by 9P(20) laser. The horizontal axis is the offset frequency of the probe laser with the GHz part removed. 135

Chapter 1

Overview

Double resonance involves the simultaneous application to a sample of two radiation sources both resonant or near-resonant with transitions in the molecules of the sample. One of the radiation sources, usually referred to as the pump, has to be sufficiently intense to produce a change in the population distribution between the two levels of the pumped transition. The other radiation source, which may be weak and is known as the probe, is used to monitor the effect of the pump, and the resulting spectrum is called the double resonance spectrum. There are two types of double resonances, one of which is three-level double resonance in which one of the pumped levels is also one of the probed levels. The other is four-level double resonance in which the pumped and probed levels are entirely separated.

Three-level double resonance can be used to simplify the assignment of a complicated spectrum. Since the two transitions have a common energy level, knowledge of one transition helps to assign the other. Four-level double resonance in gaseous samples can be used to study collisionally-induced transitions. Since the population has to be transferred from the pumped to the probed levels via intermolecular collision, this type of experiment provides information about the interaction between the colliding molecules.

The study of collisionally-induced transitions by the four-level double resonance technique was pioneered by Oka (1-2) in the microwave region. Since that time, double resonance techniques have been used to study various properties of collisionally-induced energy transfer in almost every range of the electromagnetic spectrum. Examples includes studies of selection rules for

vibrational energy transfer (3-4), studies of the mechanisms for rotational and vibrational energy transfer (4-10), measurement of rates and channels for rotational energy transfer (7-9, 11-20) and vibrational redistribution (3-5, 21), and studies of velocity changes resulting from both elastic and inelastic collisions (22-30).

Infrared-infrared double resonance has unique advantages for the study of velocity changing collisions. Because the Doppler width in the mid-infrared region is large compared to both the available resolution and the homogeneous width for low-pressure gases, a strong monochromatic infrared laser can prepare molecules in a specific vibration-rotation state with a specific velocity component in the direction of the radiation. A second monochromatic, but continuously tunable infrared laser can then probe states that are collisionally-related to the pumped state and provide detailed information about the correlation between velocity change and state change upon collision. Unfortunately, mainly because of the lack of highly monochromatic tunable sources, studies of this type were very limited until recently.

An infrared-infrared double resonance experiment employing the above concept was carried out first by Bischel and Rhodes (27). In their study, the qualitative features of the velocity change during rotationally inelastic collisions in CO₂ molecules were characterized. However, due to the lack of accuracy of the recorded data, quantitative analysis of the velocity change upon collision was not carried out. Also, because of the limited tunability of their probe source (CO₂ laser within the laser gain curve), they could not use their system to study molecules other than CO₂.

The first quantitative characterizations of the velocity changes during rotational energy transfer were reported for ¹⁵NH₃ and ¹³CH₃F by Matsuo *et al* from this laboratory (28, 29). In these studies, a single transition in a fundamental vibration-rotation band was pumped by radiation from a single-mode CO₂ laser

while a transition in a hot band was probed by a tunable infrared microwave sideband laser source. The achievements of these studies were in providing experimental observations of what we called “transferred spikes” and in laying a theoretical foundation for analysis of the transferred spikes to extract information about the velocity change during the collisionally-induced transitions. The uniqueness of the experimental strategy was that the pumping power was relatively low (c.w. CO₂ laser) and the probe source had an extremely high resolution. Low pumping power guaranteed the excitation of molecules with a narrow velocity distribution while a high resolution probe source made it possible to examine the detailed velocity distribution after collision. This was in contrast to the infrared-infrared double resonance experiments employing either a pulsed high-power pump laser, or a relatively lower resolution probe source (e.g. infrared diode laser), such as the work from Steinfeld’s group at MIT (15-17, 20). In their work, the pumping power density was so high that the power broadening was sufficient to cause pumping of nearly all velocity groups.

This thesis is an extension of the infrared-infrared double resonance technique employed by Matsuo *et al* to broader applications. We concentrate on infrared-infrared double resonance spectroscopy in methyl fluoride. For convenience, we briefly describe here the terminology of the rovibrational transitions in methyl fluoride that are used in this thesis.

Methyl fluoride is a symmetric top molecule with six vibrational modes, all of which are infrared active. There are three non-degenerate vibrational modes ν_1 , ν_2 , ν_3 and three degenerate vibrational modes ν_4 , ν_5 and ν_6 . We are only interested in rovibrational transitions in ν_3 and ν_6 .

The energy levels in the ν_3 vibrational mode can be specified with three quantum numbers (in the ground electronic state): v ($v=0, 1, 2, 3, \dots$), the quantum numbers for vibrational motion; J ($J=0, 1, 2, 3, \dots$), the quantum number for total rotational angular momentum; and K ($K=0, 1, 2, \dots, J$), the absolute value of the

quantum number for the projection of rotational angular momentum in the direction of the molecular axis (C-F bond in CH₃F). The selection rules for the vibration-rotation transitions in the ν_3 mode are $\Delta\nu_3 = 1$ (only absorption is concerned); $\Delta K = 0$; and $\Delta J = 0, \pm 1$, which corresponds to three different branches: P ($\Delta J = -1$), Q ($\Delta J = 0$) and R ($\Delta J = 1$). We usually call rovibrational transitions from vibrational state $\nu_3=0$ to $\nu_3=1$ the ν_3 fundamental band and from $\nu_3=n$ to $\nu_3=m$ the $m\nu_3 - n\nu_3$ hot band. The symbol for a transition is ${}^{\Delta K}_{\Delta J}(J, K)$, where J and K are quantum numbers of the lower state of the transition, ΔJ is P, Q or R depending on whether ΔJ equals -1, 0, or 1, respectively, and ΔK is always Q since $\Delta K = 0$. Thus, the ${}^Q_R(4,3)$ fundamental transition represents a transition from the state with $\nu_3=0$, $J=4$ and $K=3$ to the state with $\nu_3=1$, $J=5$ and $K=3$; and the ${}^Q_P(14,2)$ transition in the $2\nu_3 - \nu_3$ hot band represents a transition from the state with $\nu_3=1$, $J=14$ and $K=2$ to the state with $\nu_3=2$, $J=13$ and $K=2$.

A few transitions in the $\nu_3 + \nu_6 - \nu_6$ vibrational band are also used in the thesis. This band contains rovibrational transitions from the vibrational state $\nu_6=1$ and $\nu_3=0$ to the vibrational state $\nu_6=1$ and $\nu_3=1$. These vibrational states are doubly degenerate and an additional quantum number l is necessary to specify a rotational energy level; l is the quantum number for the projection of vibrational angular momentum on the molecular axis ($l = \pm 1$ in either $\nu_3=0$, $\nu_6=1$ or $\nu_3=1$, $\nu_6=1$). Since only the transitions with selection rule $\Delta l = 0$ are used in this thesis, the symbol ${}^{\Delta K}_{\Delta J}(J, K, l)$ is used to represent a transition in this band. For example, the ${}^Q_R(9,3,1)$ transition in the $\nu_3 + \nu_6 - \nu_6$ band stands for a transition from the rotational level with $J=9$, $K=3$ and $l=1$ in the $\nu_6=1$ vibrational state to the rotational level with $J=10$, $K=3$ and $l=1$ in the $\nu_3=1$ and $\nu_6=1$ vibrational state.

Chapter 2 contains studies of three-level double resonance line shapes in methyl fluoride. During the analysis of four-level double resonance spectra, Matsuo (29) found that the three-level double resonance line shape calculated by a semi-classical treatment showed a splitting which was apparent in the observed

spectrum, but not resolved. The problem was left unsolved. During our study of effects of initial velocity on the rotational energy transfer in $^{13}\text{CH}_3\text{F}$ (Chapter 4), we found that some of our three-level double resonance spectra had flat tops. To our surprise, when we reduced or eliminated several possible factors that could wipe out the splitting in the spectra, we started to get spectra that looked like the calculated line shape. In these studies, a rovibrational transition in the ν_3 fundamental band was pumped by a CO_2 laser while another rovibrational transition, either in the $2\nu_3 - \nu_3$ hot band or in the ν_3 fundamental band, was probed by a tunable CO_2 sideband laser source. Dynamic Stark splitting in infrared-infrared three-level double resonance in methyl fluoride was observed. Although dynamic Stark splitting was a well-known phenomenon in the radio-frequency and microwave region, and even a few observations had been reported in the optical region, this work represented the first observation in the infrared region for molecules in thermal equilibrium. By using the method of least squares, we fit the theoretical line shape based on the density matrix formalism to the observed spectrum. The numerical comparison provided a check for the validity of the current theory of three-level double resonance line shapes. The results of the fitting provided information on the sample molecule itself, such as the Rabi frequency and the relaxation rates. Although we were not able to determine reliable relaxation rates in the current studies, mainly because our present apparatus was not good enough, the problems associated with their measurement were extensively studied. Therefore, these studies can be viewed as a promising first step toward such measurements.

The topics in Chapter 3 are applications of four-level double resonance to the study of collisionally-induced rotational and vibrational energy transfer in methyl fluoride colliding with different foreign gas molecules, including isotopically-labelled methyl fluoride. For this purpose, a rovibrational transition in the ν_3 band was pumped by a CO_2 laser while another rovibrational transition, either in the

$2\nu_3 - \nu_3$ band or in the $\nu_3 + \nu_6 - \nu_6$ band, was probed by our infrared sideband system. The former double resonance combination allowed the study of rotational energy transfer and the latter the study of vibrational energy transfer. While recording double resonance spectra for methyl fluoride in an excess of different foreign gases, the properties of the energy transfer for different colliding pairs could be investigated. The major findings from these experiments included (i) the correlations between translational momentum change and angular momentum change during rotational energy transfer for methyl fluoride colliding with H_2 , He, Ar, Xe and CH_3F ; (ii) evidence of direct vibrational energy transfer in methyl fluoride and the corresponding symmetry selection rules; (iii) evidence of a recoil effect when methyl fluoride collides with Ar atoms. For theoretical interpretation of these results, we employed classical elastic scattering theory and the procedures used by Borenstein and Lamb to calculate one-dimensional collision kernels with Lennard-Jones and Buckingham-Slater intermolecular potential functions. The theoretical calculations were able to demonstrate most of the qualitative features for the collisionally-induced rotational transitions observed in experiments. This study indicated the possibility of obtaining quantitative information on the intermolecular interaction potential of the colliding molecules through comparison between more sophisticated calculations (e.g. semi-classical inelastic scattering theory) and experimental observations.

Chapter 4 concerns the effect of initial velocity on collisionally-induced rotational energy transfer in methyl fluoride. The velocity component of the pumped molecules in the direction of the pump laser depends on the difference between the frequency of the pump laser and the center frequency of the pump transition. Varying the pump laser frequency changes the relative r.m.s. speed of the colliding molecules. We stabilized a CO_2 laser to Lamb dips in Stark spectra in a cell outside of the laser cavity. With this stabilization scheme, we were able to lock the laser at different frequencies within the laser gain curve. This technique

provided a tunability of about 30 MHz for each laser line. By using the laser stabilized with this scheme as a pumping source, we were able to pump molecules with different relative r.m.s. speed to their colliding partners. This allowed us to study the initial velocity dependence of the collisionally-induced rotational energy transfer. It was found that r.m.s. velocity change increased as the relative r.m.s. velocity of the colliding molecules increased. We used classical elastic scattering theory to calculate the one-dimensional collision kernel at different initial velocities. The results of the calculation failed to represent the qualitative features of the observation.

Finally, Chapter 5 contains the applications of double resonance techniques to assign weak transitions in the $3\nu_3 - 2\nu_3$ hot band of $^{12}\text{CH}_3\text{F}$, to measure precise center frequencies of a few transitions in both $^{12}\text{CH}_3\text{F}$ and $^{13}\text{CH}_3\text{F}$, and to obtain additional information about collisionally-induced transitions. Transitions in the $3\nu_3 - 2\nu_3$ band are very weak since the lower vibrational state of the band is a highly excited vibrational state and the population is extremely small. Transitions in this band had not been observed previously. We used strong CO_2 laser radiation to pump near-coincident transitions in the $2\nu_3 - \nu_3$ hot band of $^{12}\text{CH}_3\text{F}$ while searching for transitions in the $3\nu_3 - 2\nu_3$ hot band. This unique technique allowed us to observe six transitions in the $3\nu_3 - 2\nu_3$ band. Molecular constants for the $\nu_3=3$ vibrational state were determined from the frequencies of the transitions. This work demonstrated the usefulness of the double resonance technique for observing and assigning very weak transitions. In order to obtain precise center frequencies of transitions with infrared-infrared double resonance, we took the advantage of the Doppler-free feature of the double resonance spectra. For this purpose, a series of counterpropagating and copropagating three-level and four-level double resonance spectra were recorded to determine the precise center frequencies for a number of transitions in both $^{12}\text{CH}_3\text{F}$ and $^{13}\text{CH}_3\text{F}$. The absolute accuracy for the transitions determined in this work is ~ 0.1 MHz which was about

one order of magnitude better than the previously measured values.

References

1. T. Oka, J. Chem. Phys. 45, 754-755 (1966); T. Oka, J. Chem. Phys. 47, 13-26 (1967); T. Oka, J. Chem. Phys. 47, 4852- 4853 (1967); T. Oka, J. Chem. Phys. 48, 4919-4928 (1968); T. Oka, J. Chem. Phys. 49, 3135-3145 (1968).
2. T. Oka, Adv. At. Mol. Phys. 9, 127-206 (1973).
3. F. Menard-Bourcin and L. Doyennette, J. Chem. Phys. 88, 5506-5511 (1988).
4. J. G. Haub and B. J. Orr, J. Chem. Phys. 86, 3380-3409 (1987).
5. C. P. Bewick and B. J. Orr, J. Chem. Phys. 93, 8634-8642 (1990).
6. S. Kano, T. Amano, and T. Shimizu, J. Chem. Phys. 64, 4711-4718 (1976).
7. R. I. McCormick, F. C. De Lucia, and D. D. Skatrud, IEEE J. Quantum Electron. QE-23, 2060-2067 (1987).
8. H. O. Everitt and F. C. De Lucia, J. Chem. Phys. 90, 3520-3527 (1989).
9. H. O. Everitt and F. C. De Lucia, J. Chem. Phys. 92, 6480-6491 (1990).
10. C. P. Bewick, J. F. Martin, and B. J. Orr, J. Chem. Phys. 93, 8643-8657 (1990).
11. N. Morita, S. Kano, Y. Ueda, and T. Shimizu, J. Chem. Phys. 66, 2226-2228 (1977).
12. N. Morita, S. Kano, and T. Shimizu, J. Chem. Phys. 69, 277-280 (1978).
13. W. A. Kreiner, A. Eyer, and H. Jones, J. Mol. Spectrosc. 52, 420-438 (1974).
14. R. M. Lees, C. Young, J. Van der Linde, and B. A. Oliver, J. Mol. Spectrosc. 75, 161-167 (1979).
15. J. I. Steinfeld, I. Burak, D. G. Sutton, and A. V. Nowak, J. Chem. Phys. 52, 5421-5434 (1970).
16. D. Harradine, B. Foy, L. Laux, M. Dubs, and J. I. Steinfeld, J. Chem. Phys. 81, 4267-4280 (1984).

17. B. Foy, L. Laux, S. Kable and J. I. Steinfeld, Chem. Phys. Lett. 118, 464-467 (1985).
18. Y. Honguh, F. Matsushima, R. Katayama, and T. Shimizu, J. Chem. Phys. 83, 5052-5059 (1985).
19. K. Veeken, N. Dam, and J. Reuss, Chem. Phys. 100, 171-191 (1985).
20. B. Foy, J. Hetzler, G. Millot, and J. I. Steinfeld, J. Chem. Phys. 88, 6838-6852 (1988).
21. H. K. Haugen, W. H. Pence, and S. R. Leone, J. Chem. Phys. 80, 1839-1852 (1984).
22. E. Arimondo, P. Glorieux, and T. Oka, Phys. Rev. A 17, 1375-1393 (1978); P. Glorieux, E. Arimondo, and T. Oka, J. Phys. Chem. 87, 2133-2141 (1983).
23. R. G. Brewer, R. L. Shoemaker, and S. Stenholm, Phys. Rev. Lett. 33, 63-66 (1974).
24. R. L. Shoemaker, S. Stenholm, and R. G. Brewer, Phys. Rev. A 10, 2037-2050 (1974).
25. J. W. C. Johns, A. R. W. McKellar, T. Oka, and M. Römheld, J. Chem. Phys. 62, 1488-1496 (1975).
26. P. R. Berman, J. M. Levy, and R. G. Brewer, Phys. Rev. A 11, 1668-1688 (1975).
27. W. K. Bischel and C. K. Rhodes, Phys. Rev. A 14, 176-188 (1976).
28. Y. Matsuo, S. K. Lee, and R. H. Schwendeman, J. Chem. Phys. 91, 3948-3965 (1989).
29. Y. Matsuo and R. H. Schwendeman, J. Chem. Phys. 91, 3966-3975 (1989).
30. U. Shin, Q. Song, and R. H. Schwendeman, J. Chem. Phys. 95, 3964-3974 (1991).

Chapter 2

Observation of Dynamic Stark Splitting in Three-Level Infrared-Infrared Double Resonance

I. Introduction

Theoretical and experimental studies of three-level double resonance line shapes have been presented many times (1-18). One of the most interesting phenomena in these studies is dynamic Stark splitting (Rabi splitting; the Autler-Townes effect (1)) which shows a doublet in the probe transition while two of the three energy levels are pumped by fairly strong monochromatic radiation. The phenomenon can easily be observed in the radiofrequency or microwave region of the spectrum (2) in which it is relatively easy to obtain radiant power densities and dipole transition moments large enough to create a Rabi frequency that is greater than either the homogenous or inhomogeneous broadening (3). It is more difficult to see the phenomenon at optical frequencies where the Doppler averaging tends to wash out the effect. Although a few observations of the phenomenon have been reported in the visible region (4-6), the splitting has not, to our knowledge, been reported for infrared-infrared double resonance involving vibration-rotation spectra of gaseous molecules, except in molecular beams in which Doppler effects are greatly suppressed (18). In this chapter studies of dynamic Stark splitting in three-level infrared-infrared double resonance spectra in $^{12}\text{CH}_3\text{F}$ and $^{13}\text{CH}_3\text{F}$ are discussed.

Our three-level double-resonance experiment was prompted at first by the

need to estimate the infrared power density of the output from a CO₂ laser that was used as the pumping source for a series of infrared-infrared four-level double resonance measurements in methyl fluoride (19-21). We found that dynamic Stark splitting could be observed in ¹³CH₃F at low sample pressure when the Q_R(4,3) transition in the ν_3 fundamental was pumped while the Q_P(5,3) transition in the $2\nu_3 - \nu_3$ hot band was probed. Then we investigated three other combinations of pump and probe in ¹²CH₃F. For the combination of the Q_Q(12,2) pump in the ν_3 fundamental with the Q_R(12,2) probe in the $2\nu_3 - \nu_3$ hot band, no splitting was observed. By contrast, for the combinations of the Q_R(11,9) pump in the ν_3 fundamental with either the Q_Q(12,9) or the Q_R(12,9) probe in the $2\nu_3 - \nu_3$ hot band, the splitting was clearly seen.

Dynamic Stark splitting can be predicted from the semi-classical treatment of a three-level system interacting with two monochromatic electro-magnetic fields. Although both theoretical and experimental studies of three-level double resonance line shapes have been the subject of many papers in the literature, a quantitative numerical comparison between the full semi-classical calculation and the experimental observation has not been found for the case where both spatial degeneracy of the energy levels and Doppler effects of the molecules have to be considered. An interesting question is: How well does the semi-classical double resonance theory predict the line shapes recorded in the laboratory, especially when dynamic Stark splitting is observed? In order to answer the question, we numerically calculated the double-resonance spectra with a computer program that solved the 8x8 linear system of equations that results from a density matrix treatment of the three-level system (13). The program solved these equations for many values of the component of the molecular velocity in the direction of the pump beam, multiplied each of these solutions by the appropriate Boltzmann factor, and summed the result. The spatial degeneracy was treated by calculating

the contribution from each component of the spatially degenerate state and then summing the results. In order to improve the speed of the calculation, an algebraic solution of the linear system, valid for all pump and probe powers, was worked out and incorporated into the program (14). Finally, the spectral generation program was incorporated into a full least-squares fitting routine in which the amplitude and center frequency of the probe transition, the Rabi frequency for the pump radiation, and the population and coherence relaxation rates are all adjusted to provide a best fit of the observed spectrum. It was found that the complete semi-classical treatment represents all the observed line shapes very well.

As a result of the least squares fitting of the observed line shapes, the Rabi frequency for the pump radiation, and the population and coherence relaxation rates for sample molecules can be obtained. These parameters were found to be much more sensitive to the three-level double resonance spectra that showed a dynamic Stark splitting. We were surprised to find that for nearly all of the double-resonance combinations examined, the dependences on population and coherence relaxation rates are not extremely highly correlated, so that it should be possible to obtain these rates separately from high-quality spectra. As will be seen below, we are not able to determine these rates with our present apparatus. The reason is traced to the fact that a number of effects can broaden the observed line shapes. These effects are analyzed and numerically simulated, and strategies to reduce or eliminate these effects are proposed. Thus, the present work is best regarded as a promising first step toward such measurements.

II. Theoretical Part

The density matrix equations for a three-level system have been given many times (e.g., Refs. 4-6, 13-17, and additional references cited in these papers). In the

present work we are concerned with energy levels in both a “stacked” or “cascade” configuration, in which the levels are arranged such that $E_a < E_b < E_c$, and two “folded” configurations in which the levels are arranged such that $E_a < E_b > E_c$ or $E_a > E_b < E_c$ (Fig. 2.1). Steady-state algebraic solutions were worked out by Schwendeman for all of the possible stacked and folded configurations and were included in computer programs to calculate spectra for the general case and to fit spectra for the case of saturating pump power and low probe power. The algebraic solutions, which are given in the Appendix, have been checked against the results obtained by numerical solution of the linear system and against the algebraic solution given by Takami (15). The programs include numerical integration over the Doppler shift and summation over the components of the projection of the angular momentum on the space-fixed Z axis (m components).

The algebraic solution given in the Appendix is limited to the special case in which the collisional relaxation of the two combinations of diagonal density matrix elements, $(\rho_{aa} - \rho_{bb})$ and $(\rho_{bb} - \rho_{cc})$, and the three off-diagonal elements, ρ_{ba} , ρ_{cb} , and ρ_{ca} , all occur independently. Normally, the off-diagonal elements are expected to relax independently, since transfer of coherence, especially for very different frequencies, should be very weak. However, the relaxation of the diagonal elements should include collisional transfer of population from one state to another, which couples the time dependence of the diagonal elements. In the present case, however, in which state a is in the ground vibrational state, b is in $v_3 = 1$, and c is in $v_3 = 2$, the rate of collisional transfer of population between these states is very small because of the generally low rate of vibrational energy transfer. It is shown in the Appendix that under these conditions, there is no collisional interaction between $(\rho_{aa} - \rho_{bb})$ and $(\rho_{bb} - \rho_{cc})$ if the relaxation rates for ρ_{aa} , ρ_{bb} , and ρ_{cc} are the same. We make this assumption, which leads to identical

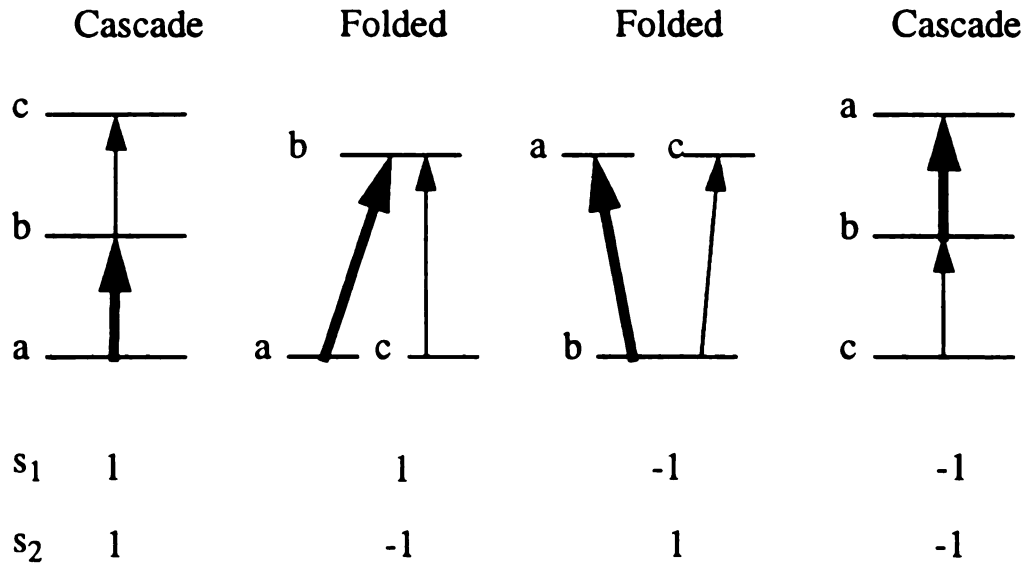


Figure 2.1. Four possible energy arrangements for three-level double resonance. In each case the bold arrow represents the pump beam of frequency ν_1 and the light arrow represents the probe beam of the frequency ν_2 . The s_1 and s_2 are sign factors used in the equations in the appendix.

rates for $(\rho_{aa} - \rho_{bb})$ and $(\rho_{bb} - \rho_{cc})$. However, the fitting program does not require equal rates; it assumes that the two diagonal relaxation rates are each proportional to a single population rate (referred to as γ_p) and that the three off-diagonal rates are each proportional to a single coherence relaxation rate (referred to as γ_c). Each of the five proportionality constants may be selected independently, but in all of the fittings reported here they have been set equal to one.

For the summation over the m states, the Rabi frequency for the pumping radiation was assumed to be

$$x_m = x_p \langle J', k, m | \phi_{ZZ} | J'', k, m \rangle$$

in which $x_p = \mu_p \epsilon_o / h$ where μ_p is the vibrational contribution to the transition moment and ϵ_o is the amplitude of the electric field of the radiation

$\epsilon = \epsilon_o \cos 2\pi \nu_p t$; ϕ_{ZZ} is a direction cosine. The electric field of the pump was taken to be in the space-fixed Z direction in which case the electric field of the probe in our apparatus is perpendicular to Z. The Rabi frequencies for the probe transitions were shown to be small enough that the only effect of changing their values was to change the intensity of the double resonance. Thus, even though each pump transition participated in two double resonances, the intensities could be simply added so that only one double resonance calculation was required for each $M = |m|$.

For the least-squares fitting, the algebraic solution of the density matrix equations was differentiated with respect to the center frequency of the probe transition, x_p , γ_p , and γ_c , and routines were written to calculate these derivatives as needed. The difference between the fixed frequency of the pump laser and the center frequency of the pump transition was assumed in the calculation, even

though these values are not extremely well-known for the transitions of interest in this work. However, there is a strong correlation between the pump frequency offset and the center frequency of the probe (i.e., the probe frequency offset) so that these two values could not be determined separately. At the same time, the results of the calculations (except for the center frequency of the probe transition) were unchanged by small changes in the assumed value of the offset. (A two-level double resonance technique for precise determination of the pump frequency offset is described below.) The amplitude, background, and a linear slope of the background were additional parameters included in the least-squares fitting.

As will be discussed below, the relaxation rates obtained from the least-squares fittings were not very reproducible. In order to determine reasons for this situation, three theoretical tests were performed. One of these was a test of the effect of the intentional frequency modulation applied to the pump and probe lasers for stabilization. The effect of frequency modulation on the lineshapes of saturation dips was derived by Borde' et al. (22) by introducing a time-dependent phase into the electric field of the beam. We chose to test this effect by performing a time-averaging of the radiation. For this test a theoretical lineshape was calculated at closely-spaced intervals in frequency of the probe laser. The amplitude of the frequency modulation was assumed to be $n + 1/2$ frequency intervals, where n is an integer. To calculate the effect of modulation for the k th point, the computed intensities for the points $k - n \leq j \leq k + n$ were weighted by the factor $\pi^{-1} [(n + 1/2)^2 - j^2]^{-1/2}$ and summed. This may be shown to be equivalent to the effect of sinusoidal frequency modulation of the probe or pump laser frequency. The final computed lineshape was then subjected to the usual least-squares fitting.

The second theoretical test was a check of the effect of a small misalignment of

the pump and probe beams. Because the beam directions were determined over several meters path, the actual misalignment should be small. On the other hand, it is difficult to avoid some divergence in the beam size, which for beams traveling in opposite directions should appear as a misalignment in part of the beam. To reduce this effect the probe beam was sampled at the center of its profile with a detector that is only 1 mm square. Nevertheless, the results of the theoretical calculations suggest that misalignment is an important contributor to the unreliable relaxation parameters. To perform these calculations, the pump beam was assumed to be traveling in the negative X space-fixed direction. Then, the Doppler correction for molecules with X-component of velocity, v_X , and arbitrary components in the other two directions is $k_p v_X$, where k_p is the magnitude of the wave vector for the pump beam. The probe beam was assumed to be oriented in the space-fixed XY plane at an angle θ to the pump beam. The Doppler correction for the probe beam is then $k(v_X \cos \theta + v_Y \sin \theta)$, where k is magnitude of the wave vector for the probe beam and v_Y is the component of molecular velocity in the space fixed y direction. The double resonance was calculated at intervals in v_X and v_Y , multiplied by the appropriate combined Boltzmann factor and summed. The resulting lineshape was then used as input for the usual least-squares fitting.

The third theoretical test was a check of the effect of a possible contribution of four-level double resonance to the three-level spectrum. A four-level contribution would arise from collisionally-induced transitions out of one of the probe states followed by transitions back into the state. These transitions have been shown to occur without much change in velocity so that they produce a peak similar to the three-level double resonance, but without any dynamic Stark splitting (19-21). We have found that under the conditions of our three-level experiments, with the $Q_R(4,3)$ pump in the v_3 band of $^{13}\text{CH}_3\text{F}$, the maximum amplitude of the transferred

spike for the $Q_P(7,3)$ transition in the $2\nu_3 - \nu_3$ band is $\sim 10\%$ of the maximum amplitude of the three-level effect on the $Q_P(5,3)$ transition in the $2\nu_3 - \nu_3$ band. If the principal contribution to the transferred spike in the $Q_P(7,3)$ lineshape is the result of two collisionally-induced transitions within $\nu_3 = 1$, one from the pumped $(5,3)$ state to the $(6,3)$ state and a second from $(6,3)$ to $(7,3)$, then the contribution to the apparent three-level double resonance spectrum of the $Q_P(5,3)$ transition from four-level effects should be $\sim 10\%$ (since two collisionally-induced transitions, from $(5,3)$ to $(6,3)$ and back again will produce a four-level effect on the $(5,3)$ level). To estimate the result of four-level effects on the three-level lineshapes, collisionally-transferred spikes were computed by using Eq. (42) in Ref. 19 and added to theoretical three-level lineshapes. As described in Refs. (19, 20), the transferred spikes were calculated by using a collision kernel that is the sum of two Keilson-Storer functions (23). The parameters selected for the present calculations were those for the $Q_P(7,3)$ transition in Table I of the Ref. 20. The amplitude of the transferred spike for each composite lineshape was adjusted to be 10% or 15% of the maximum amplitude of the three-level contribution. The composite lineshape was then subjected to the usual least-squares fitting.

III. Experimental Part

Figure 2.2 is a block diagram of the infrared-infrared double resonance spectrometer used in this work. Two single-mode CO_2 lasers were used, one of which is a flowing gas system that can only be operated with $^{12}\text{C}^{16}\text{O}_2$ gas. The flowing gas system is useful for operating at high J laser lines and has a larger available laser power. The other laser has a semi-sealed plasma tube which can use

an isotopic CO₂ sample. Both lasers are frequency stabilized by means of fluorescence Lamb dips in CO₂ samples in cells outside the laser cavity (24). The overall frequency stability, including the intentional frequency modulation for stabilization purposes, is ± 150 kHz. A CO₂ laser stabilized to a fluorescence Lamb dip of CO₂ molecules emits radiation at the center frequency of the laser transition. As will be described in Chapter 4, many CO₂ laser lines can be also stabilized to a Stark Lamb dip of molecules other than CO₂, in which case the laser radiation does not have to be at the center frequency of the laser transition. The application and advantage of this frequency stabilization scheme will be discussed in more detail in Chapter 4.

The pump radiation source uses a CO₂ laser line with a fixed frequency which is near-coincident with one of the vibration rotation transitions in CH₃F. The probe radiation source is a continuously tunable infrared microwave sideband laser that is generated by mixing CO₂ laser and microwave radiation within a CdTe electro-optic modulator crystal that is mounted in a matched waveguide (25). There are three frequency components in the beam after the modulator: the carrier, which is at the original CO₂ laser frequency, and two sidebands, whose frequencies are the sum and the difference of the frequencies of the CO₂ laser and microwave sources. The carrier is horizontally polarized and the sidebands are vertically polarized, so it is easy in principle to separate them simply by a polarizer. However, the carrier power is more than three orders of magnitude greater than the sideband power, so complete suppression of the carrier is extremely difficult. The configuration of the pump and probe in this study was counter-propagating, in which the pump and the probe radiations propagate in the same spatial region but in opposite directions. Two polarizers are placed on each side of the sample cell in order to pass one beam selectively and block the other beam. Polarizer POL 1 (Fig. 2.2)

allows the sidebands to pass through while reflecting the carrier to a fluorescence cell for frequency stabilization. Polarizer POL2, however, lets the pumping laser enter the sample cell while reflecting the probe beam to the detector so that the double resonance signal can be recorded. The probe laser is 100% amplitude modulated at 33 kHz, by chopping the microwaves applied to the modulator crystal, while the pump laser beam is 100% amplitude modulated at 300 Hz by means of a mechanical chopper. In order to stabilize the amplitude of the probe laser, a second detector is used to monitor the laser power in front of the sample cell. The output of the detector drives a feedback circuit which controls the microwave power applied to the modulator crystal so that any change in probe power will be compensated by an appropriate change in microwave power. Typical pump powers at the entrance of the sample cell are ~1-2 W while probe powers are ~20 μ W. The microwave frequency for the IMSL source is provided by a synthesizer (± 3 kHz accuracy) and is stepped by the microcomputer that records the spectrum.

We use a double modulation scheme to analyze the double resonance signal. The signal detector output is first demodulated by a lock-in amplifier at the chopping frequency of the probe; the output of this amplifier, which contains the sum of the single-resonance and double-resonance effects, is sent to a second lock-in amplifier for an additional demodulation at the chopping frequency of the pump laser. The output of the second amplifier which contains only the double-resonance effect is digitized and recorded by the microcomputer. The detector-preamplifier combination has been shown to provide an essentially linear output by determining that single resonance spectra recorded at low pressure are Gaussian with the expected Doppler width to high accuracy (<0.5%) (26).

The sample cell for most of the work was a Pyrex tube, 1 m long and 25 mm

in diameter. The $^{13}\text{CH}_3\text{F}$ sample was obtained from Merck & Co., while the $^{12}\text{CH}_3\text{F}$ sample was obtained from Peninsular Chemical Research, Inc. Except for the usual freeze-pump-thaw cycling, the samples were used as received. All spectra were recorded at room temperature ($\sim 297\text{ K}$) at pressures in the range 2-20 mTorr; sample pressures were measured by a capacitance manometer.

The frequencies for the spectral lines shown in Table 2.1 were calculated from the molecular constants in Refs. (27-28), and the laser frequencies were calculated from the constants in Refs. (29-30).

IV. Results and Discussion

A. Observation of the dynamic Stark splitting

Dynamic Stark splitting in the vibration-rotation spectrum of methyl fluoride was first observed in $^{13}\text{CH}_3\text{F}$ for the R(4,3) pump in the ν_3 fundamental and the QP(5,3) probe in the $2\nu_3 - \nu_3$ hot band. Although the spectra recorded at the beginning showed evidence of the splitting, the lineshapes did not seem to fit very well with calculation, especially for the lower parts of the trace which seemed to be broadened by some artificial effects. The causes were analyzed and tested experimentally. We found that several factors contributed to the broadening of the experimental line shapes. These factors were frequency modulation of CO_2 lasers; divergences and misalignment of the pump and probe beams; and four-level double resonance effects. Frequency modulation is necessary for CO_2 lasers stabilized to the fluorescence Lamb dip in this laboratory. However, decreasing the amplitude of the modulation during the laser locking reduces the effect on the

Table 2.1. Pump and probe transitions used for double resonance

Sample	Transition	Band	Frequency ^a	Offset ^b	Laser
Pump Transitions					
¹² CH ₃ F	Q _Q (12,2)	ν_3	31 383 940.1	-39.6	¹² C ¹⁶ O ₂ 9P(20)
¹² CH ₃ F	Q _R (11,9)	ν_3	31 998 588.1	26.1	¹² C ¹⁸ O ₂ 9P(22)
¹³ CH ₃ F	Q _R (4,3)	ν_3	31 042 692.2	24.26 ^c	¹² C ¹⁶ O ₂ 9P(20)
Probe Transitions					
¹² CH ₃ F	Q _R (12,2)	$2\nu_3 - \nu_3$	31 557 000.3	-12 971.4	¹² C ¹⁶ O ₂ 9P(14)
¹² CH ₃ F	Q _Q (12,9)	$2\nu_3 - \nu_3$	30 913 528.6	9 386. 8	¹² C ¹⁶ O ₂ 9P(36)
¹² CH ₃ F	Q _R (12,9)	$2\nu_3 - \nu_3$	31 558 480.5	-14 451.6	¹² C ¹⁶ O ₂ 9P(14)
¹³ CH ₃ F	Q _P (5,3)	$2\nu_3 - \nu_3$	30 092 976.1	14 557.0	¹³ C ¹⁶ O ₂ 9P(16)
¹³ CH ₃ F	Q _R (4,3)	$2\nu_3 - \nu_3$	31 042 692.2	16 317.0	¹² C ¹⁶ O ₂ 9R(26)

^aCenter frequency of transition in MHz calculated from the molecular constants in Refs. (27, 28)

^bLaser frequency - center frequency in MHz. Laser frequencies obtained from Refs. (29, 30)

^cMeasured offset frequency (see text). Offset from Ref. 27 is 25.8 MHz

double resonance line shapes. Divergences and misalignment of the pump and probe beams are effectively reduced by a more careful experiment, although the effects could not be eliminated completely. Finally, the contributions of four-level double resonance effects are reduced by decreasing the sample pressure and increasing the pump modulation frequency. After improving the experimental conditions by taking into account all of the above factors, we were able to obtain spectra that fit theoretical line shapes very well by adjusting the Rabi frequency and the relaxation parameters in calculations. As mentioned above, although the factors which broaden the experimental line shapes can be effectively reduced, it is not easy to eliminate them from our present experimental apparatus. Thus, the relaxation parameters obtained from the least squares fitting of the spectra are not reliable indicators of the rates of collisionally-induced changes in the density matrix elements. Numerical tests have been carried out to see how the above factors affect the relaxation parameters from the fitting (see Theoretical section). However, the quality of the spectra is good enough to test the current theory of three-level double resonance line shapes. As will be seen, all of the features of three-level double resonance line shapes can be predicted by theoretical calculation. Figure 2.3 shows a comparison of observed and calculated double resonance line shapes in $^{13}\text{CH}_3\text{F}$ for the R(4,3) pump in the $v_3 = 1 \leftarrow v_3 = 0$ fundamental band (v_3 band) and the QP(5,3) probe in the $v_3 = 2 \leftarrow v_3 = 1$ hot band at three different sample pressures. As can be seen from the spectra, the splitting is more clearly resolved at lower pressure as a result of the decrease in the relaxation parameters. As can also be seen from the residuals, very good agreement is obtained between experimental observations and theoretical calculations.

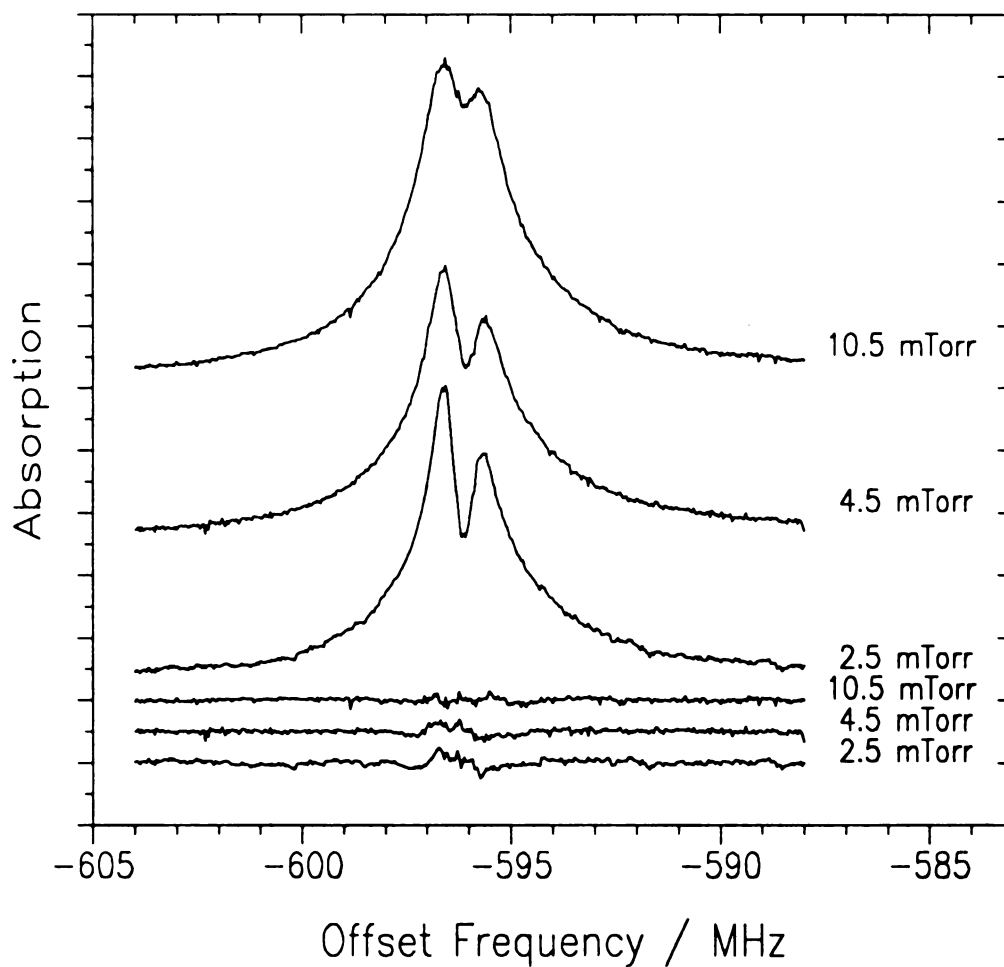


Fig. 2.3. Three-level double resonance spectra for $^{13}\text{CH}_3\text{F}$ recorded at three different sample pressures and 2.2 W infrared power. The $\text{QR}(4,3)$ transition in the ν_3 band was pumped and the $\text{QP}(5,3)$ transition in the $2\nu_3-\nu_3$ band was probed. The lasers used are given in Table 2.1. The horizontal axis is the probe laser frequency minus 30093553.09 MHz. The residuals from the least squares fittings of the lineshapes are shown at the bottom of the figure.

B. Determination of Rabi frequency

The vibrational contribution to the Rabi frequency is defined as $x_p = \frac{2\pi\mu_{ab}E}{h}$, where μ_{ab} is the vibrational transition moment for the pump transition and E is the amplitude of the electric field of the pump radiation. The value of x_p is needed in the studies of collisionally-induced transferred spikes in this laboratory. Because of the difficulties in measuring accurate laser power density, we first estimated the Rabi frequency from the Lorentz width that was obtained by least squares fitting of observed and calculated three-level double resonance spectra to a Lorentz function. Since the line shape of three-level double resonance can be very different from a Lorentz function (as in the case where a dynamic Stark splitting is seen), the Rabi frequency obtained by this procedure was not always reliable. The computer program was then modified to fit the observed spectrum to a theoretical equation derived from semi-classical density matrix theory, as shown in the Appendix. This allowed us to obtain the Rabi frequency with much higher reliability. One of the features of the Rabi frequency is its linear dependence on the amplitude of the electric field of the pump radiation, which is proportional to the square root of the pump power. In order to see how well the Rabi frequencies that we obtained obeyed this linear dependence, we recorded the spectra for the R(4,3) pump in the ν_3 fundamental and the $Q_P(5,3)$ probe in the $2\nu_3 - \nu_3$ hot band in $^{13}\text{CH}_3\text{F}$ at five different pump powers. In this experiment the pump power was controlled by putting an additional polarizer in front of the polarizer (POL2 in Fig. 2.2) that allows the pump beam to enter the sample cell. By rotating the additional polarizer away from the horizontal, the pump power could be reduced. Figure 2.4 shows the spectra and their residuals from the least squares fitting for two different pump

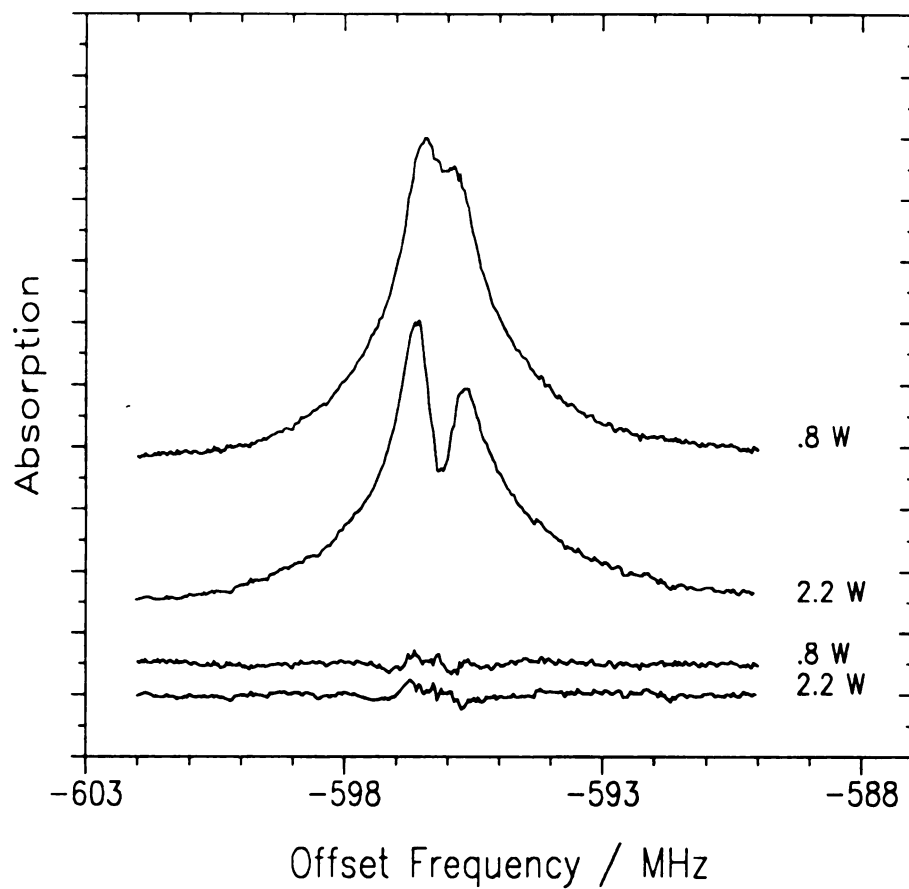


Fig. 2.4. Three-level double resonance spectra for $^{13}\text{CH}_3\text{F}$ recorded at two different infrared powers and a sample pressure of 2.5 mTorr. The pump and probe transitions, the lasers and the horizontal axis are the same as in Fig. 2.3. The residuals from the least squares fittings of the lineshapes are shown at the bottom of the figure.

powers. The Rabi frequencies obtained at five different pump powers are plotted against the square root of the pump power and shown in Fig. 2.5. The straight line in the figure has been constrained to go through zero and it is apparent that the data agree very well with the expected proportionality of the Rabi frequency to the amplitude of the electric field of the pump laser.

C. The criteria for observing dynamic Stark splitting

Many years ago, Delsart and Keller (5) listed the criteria for observation of splitting in three-level double resonance in Doppler averaged spectra: the pump frequency should be greater than the probe frequency if the pump and probe beams are in the counterpropagating configuration. The argument was that when the former is true, the relative Doppler effects tend to expand the splitting and if the latter is not true there is uncompensated Doppler broadening in the two-photon contribution to the double resonance. It is very interesting to see how well the criteria describe the spectra in our experiment where both the Doppler effect and the spatial-degeneracy affect the line shapes. For the spectra shown in Fig. 2.3 the criteria are satisfied (Table 2.1), so the splitting is observed. To test the validity of the criteria more examples seemed to be needed, including a case for which the criteria are not satisfied. For this purpose, we examined three other pump and probe combinations in $^{12}\text{CH}_3\text{F}$, all in counterpropagating geometry. For the $^{\text{Q}}\text{Q}(12,2)$ pump in the ν_3 fundamental band and the $^{\text{Q}}\text{R}(12,2)$ probe in the $2\nu_3 - \nu_3$ hot band the frequency of the pump is less than that of the probe (Table 2.1), so no dynamic Stark splitting should be observed. The recorded spectrum for this pump and probe, shown in Fig. 2.6, shows no splitting and fits the theoretical lineshape

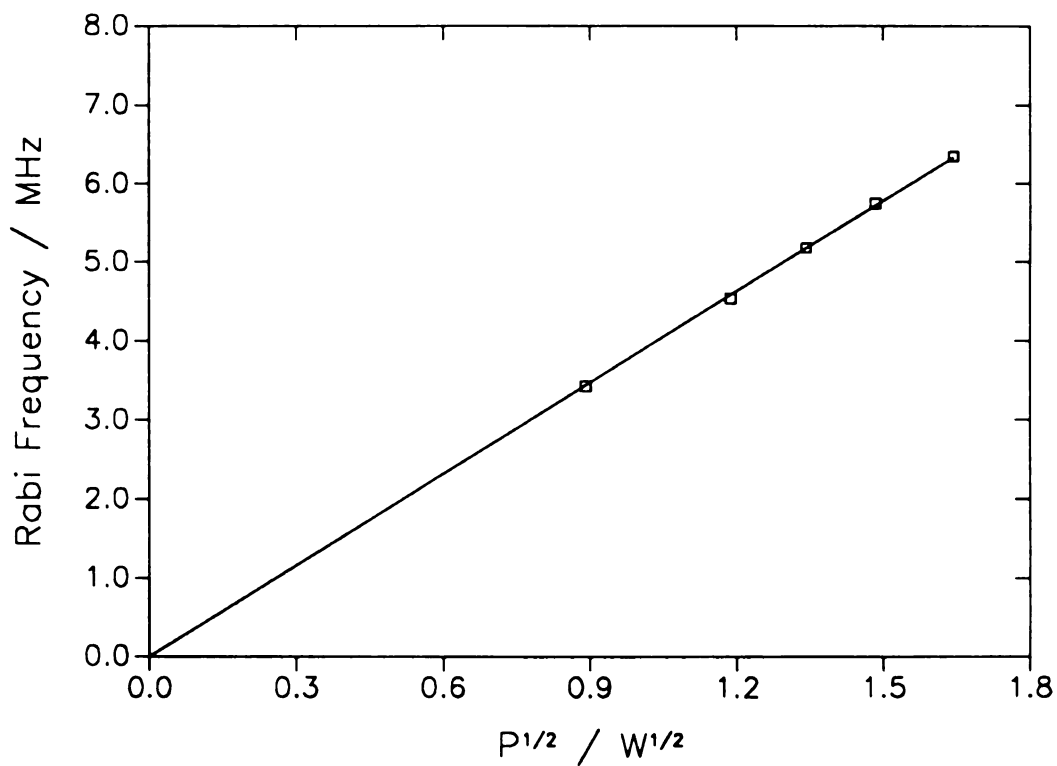


Fig. 2.5. Plot of the vibrational contribution to the Rabi frequency x_p for the spectra shown in Fig. 2.4. and three additional spectra for the same transition recorded at different powers. The straight line is the least-squares fit of the five points constrained to go through zero. The slope of the line is $5.47 \text{ MHz } W^{-1/2}$.

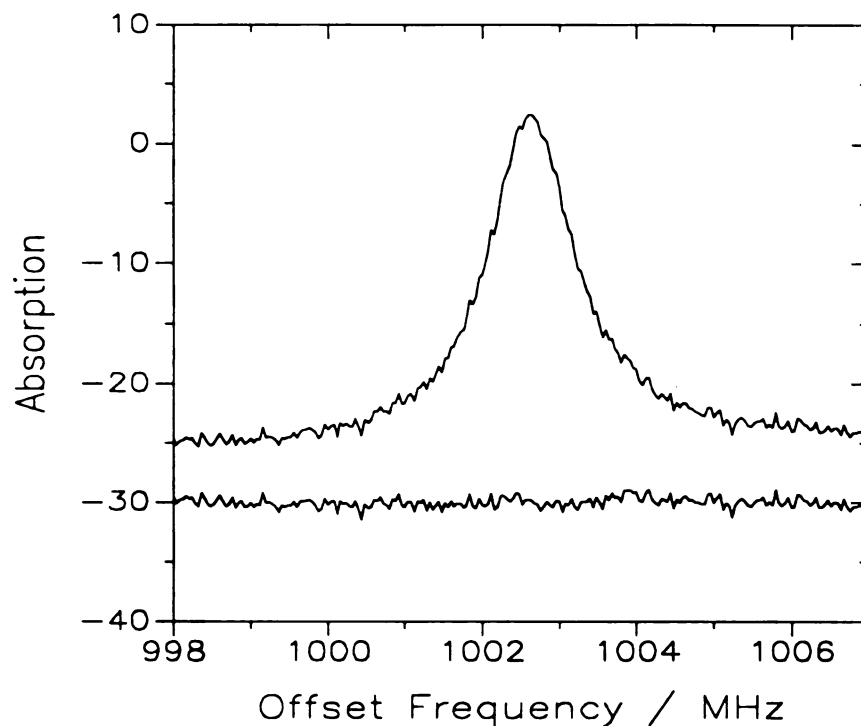


Fig. 2.6. Three level double resonance spectrum for $^{12}\text{CH}_3\text{F}$. The $\text{QQ}(12, 2)$ transition in the ν_3 band was pumped and the $\text{QR}(12, 2)$ transition in the $2\nu_3-\nu_3$ band was probed. The lasers used are given in Table 2.1. The horizontal axis is the probe laser frequency minus 31556028.88 MHz. The pump power density was $\sim 4 \text{ W/cm}^2$ and the sample pressure was 6 mTorr. The residual from the least-squares fitting is shown below the spectrum.

exceptionally well. The other two systems examined use the $Q_R(11,9)$ pump in the ν_3 fundamental, and either the $Q_Q(12,9)$ or the $Q_R(12,9)$ probe in the $2\nu_3 - \nu_3$ hot band. Although the criteria for observing the splitting are satisfied for both systems, the frequency of the $Q_R(12,9)$ probe is closer to the pump transition than that of the $Q_Q(12,9)$ probe (Table 2.1). This predicts a larger splitting in the $Q_Q(12,9)$ probe than in the $Q_R(12,9)$ probe when all the other conditions are the same. Figure 2.7 and Fig. 2.8 show the spectra recorded for these two systems at the same pump power and sample pressure. As can be seen, the spectra show exactly what is expected.

D. Precise determination of a laser offset frequency

It turns out that the $Q_R(4,3)$ transition in the ν_3 fundamental of $^{13}\text{CH}_3\text{F}$ can not only be pumped with the $9P(32)$ $^{12}\text{C}^{16}\text{O}_2$ laser, but can also be probed with the IMSL system driven by the $9R(26)$ $^{13}\text{C}^{16}\text{O}_2$ laser. Figure 2.9 shows the spectrum for this double resonance combination. This is an example of a “two-level” double resonance. In fact, it should be viewed as a three-state double resonance in terms of the degenerate m states, since the planes of polarization of the pump and probe beams are orthogonal so that if the selection rule for the pump beam is $\Delta m = 0$, the corresponding selection rule for the probe is $\Delta m = \pm 1$. One of the applications of the two-level double resonance configuration is to determine a precise offset frequency of the pump laser from the center frequency of the pump transition. As will be seen below, accurate knowledge of the pump offset is essential for studying velocity changing collisions (Chapter 4). In the least squares fitting procedure for three-level double-resonance spectra we assume a value for the offset of the pump

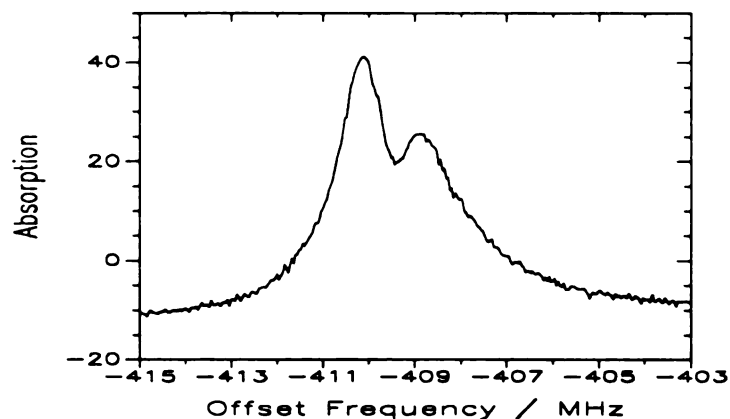


Fig. 2.7. Three-level double resonance spectrum for $^{12}\text{CH}_3\text{F}$. The $\text{QR}(11,9)$ transition in the ν_3 band was pumped and the $\text{QQ}(12, 9)$ transition in the $2\nu_3\text{-}\nu_3$ band was probed. The lasers used are given in Table 2.1. The horizontal axis is the probe laser frequency minus 30913915.43 MHz. The pump power density was $\sim 3 \text{ W/cm}^2$ and the sample pressure was 2 mTorr.

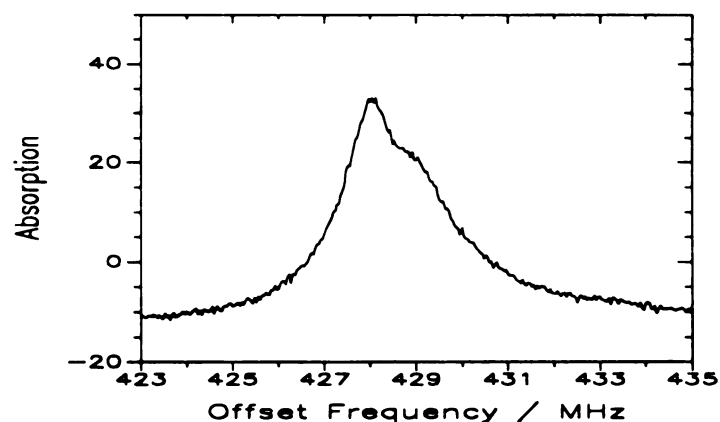


Figure. 2.8. Three-level double resonance spectrum for $^{12}\text{CH}_3\text{F}$. The $\text{QR}(11,9)$ transition in the ν_3 band was pumped and the $\text{QR}(12, 9)$ transition in the $2\nu_3\text{-}\nu_3$ band was probed. The lasers used are given in Table 2.1. The horizontal axis is the probe laser frequency minus 31558028.88 MHz. The pump power density was $\sim 3 \text{ W/cm}^2$ and the sample pressure was 2 mTorr.

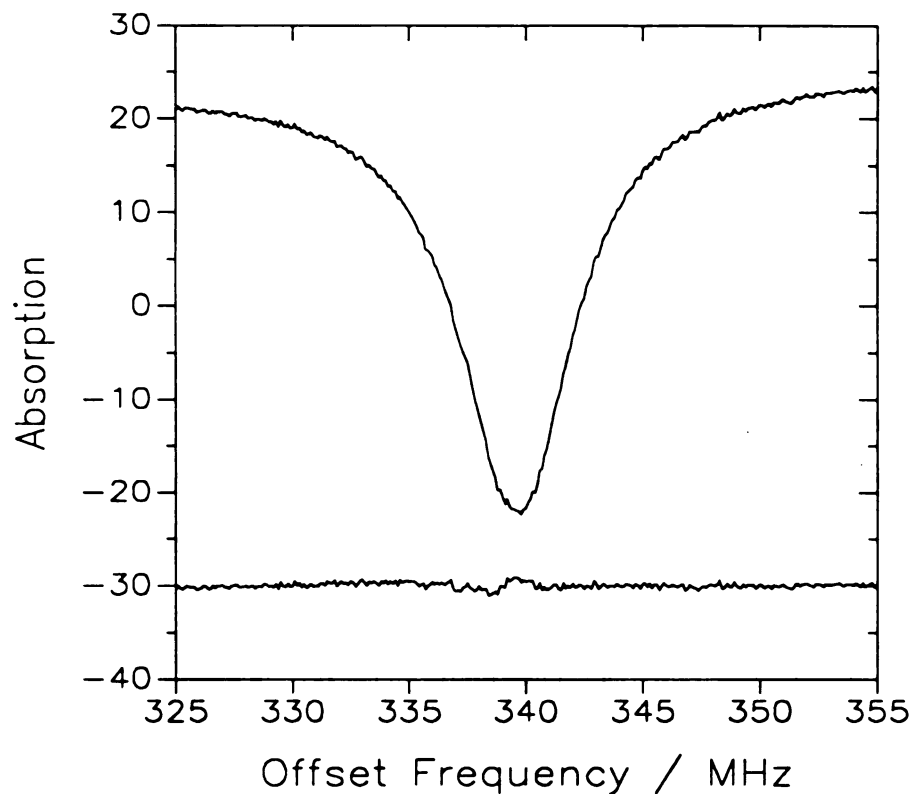


Fig. 2.9. Two-level double resonance spectrum for $^{13}\text{CH}_3\text{F}$. The $\text{QR}(4, 3)$ transition in the ν_3 band was both pumped and probed. The pump and probe lasers used are given in Table 2.1. The horizontal axis is the probe laser frequency minus 31043009.23 MHz. The pump power density was $\sim 4 \text{ W/cm}^2$ and the sample pressure was 3.5 mTorr. The residual from a least squares fitting of the lineshape is shown at the bottom of the figure.

laser frequency from the center frequency of the pump transition and fit the center frequency of the probe transition. In two-level double resonance the two center frequencies are the same, so that it is a simple matter to adjust the assumed offset until the fitted center frequency is consistent with the assumed value. The accuracy of the offset obtained in this way is mainly determined by the three-level double resonance line shape, which is Doppler free. If the laser frequencies are taken from Ref. (29-30), the resulting offset of the 9P(32) $^{12}\text{C}^{16}\text{O}_2$ laser from the center frequency of the $^{\text{Q}}\text{R}(4,3)$ transition in the ν_3 band of $^{13}\text{CH}_3\text{F}$ is 24.26 MHz. The overall accuracy of the value is estimated to be better than 0.1 MHz. Compared with the previously measured value the accuracy is increased by more than one order of magnitude. A more systematic method for measurement of accurate pump laser offsets will be discussed in Chapter 4 where counterpropagating and copropagating three-level double resonance techniques are used.

V. Conclusion

We have observed dynamic Stark splitting in three-level infrared-infrared double-resonance spectra for vibration rotation transitions of gas phase molecules. The line shapes have been found to be very well represented by calculation by means of a semi-classical density matrix treatment of a three level system including spatial degeneracy and Doppler effects interacting with two monochromatic radiations. The criteria for observation of dynamic Stark splitting in Doppler-averaged spectra have been tested and found to agree with our observations very well. It has been shown that population and coherence relaxation rates can probably be obtained independently by least squares fitting

the observed line shapes of high quality spectra. We have also pointed out the problems associated with frequency modulation of the lasers, such as that used for frequency stabilization, as well as the problems that result from beam misalignment or beam divergence and from four-level double resonance effects. These problems have to be solved in order to get reliable relaxation rates. Frequency modulation effects can be reduced by using the stabilization scheme of Schupita *et al* (31), or by using a Lamb dip in a laser Stark spectrum for stabilization as described in Chapter 4. Beam misalignment and divergence effects can be reduced significantly by using samples at higher pressure (>15 mTorr). Four-level double-resonance effects may be more difficult to eliminate. It may be possible to reduce or eliminate four-level effects by increasing the chopping frequency of the pump radiation or by using some form of polarization modulation.

VI. Appendix

Algebraic solution for a three-level system

The purpose of this appendix is to present our algebraic solution of the density matrix equations for a three-level system under the influence of two sources of radiation. The equations differ from those given by Takami (15) by including different relaxation rates for the two population differences and for the three coherences and by including factors to make them useful for the four possible energy-level configurations numbered arbitrarily in Fig. 2.1. The method of

solution has been described in a previous paper from this laboratory and will not be repeated here (14). The derivation begins by writing

$$H = H^{(0)} + H^{(r)} + H^{(\gamma)} \quad (A1)$$

in which $H^{(0)}$ is the Hamiltonian for an individual molecule in the absence of any fields, $H^{(r)}$ is the interaction that results from the applied radiation, and $H^{(\gamma)}$ is the effective Hamiltonian for molecular collision; the effect of $H^{(\gamma)}$ is included as empirical relaxation terms in the density matrix equations. As shown in Fig. 2.1, we assume a 3-level system with energy levels E_a , E_b , and E_c that are eigenvalues of $H^{(0)}$; the corresponding eigenfunctions are used as the basis functions for expansion of the density matrix. The matrix elements of $H^{(r)}$ are

$$H_{jk}^{(r)} = -\mu_{jk} (\epsilon_1 \cos 2\pi \nu_1 t + \epsilon_2 \cos 2\pi \nu_2 t), \quad (A2)$$

where ϵ_1 , ν_1 and ϵ_2 , ν_2 are the electric fields and frequencies of the two radiation sources. We assume that $\mu_{ab} = \mu_{ba}$ and $\mu_{bc} = \mu_{cb}$ are the only non-zero elements of the transition dipole moment μ , that

$$s_1 \nu_1 - \nu_{ba} = (E_b - E_a)/h \quad (A3)$$

and that

$$s_2 \nu_2 - \nu_{cb} = (E_c - E_b)/h. \quad (A4)$$

The sign factors s_1 and s_2 are ± 1 , as in Fig. 2.1. The equation of motion for the density matrix ρ is taken to be

$$\dot{\rho} = -\frac{2\pi i}{h} [H^{(0)} + H^{(r)}, \rho] - \Gamma_\rho (\rho - \rho^{(0)}) \quad (A5)$$

in which $[H^{(0)} + H^{(r)}, \rho]$ is the commutator of $H^{(0)} + H^{(r)}$ with ρ , Γ_ρ is a super-matrix of relaxation coefficients, and $\rho^{(0)}$ is the thermal equilibrium value of ρ .

Eq. (A5) is solved in the steady-state limit by application of the rotating-wave approximation. First, we substitute

$$\rho_{ba} = d_{ba} e^{-2\pi i s_1 v_1 t}, \quad (A6)$$

$$\rho_{cb} = d_{cb} e^{-2\pi i s_2 v_2 t}, \quad (A7)$$

and

$$\rho_{ca} = d_{ca} e^{-2\pi i (s_1 v_1 + s_2 v_2) t} \quad (A8)$$

into the expanded form of Eq.(A5) and then write the resulting equation as a time derivative of ρ_{aa} , ρ_{bb} , ρ_{cc} , d_{ba} , d_{cb} or d_{ca} on the left-hand side of the equals sign. On the right-hand side all terms that oscillate at frequency $v_1 - v_2$ or higher are eliminated. The resulting equations are then set to zero to obtain the steady-state solutions.

When the procedure just described is carried out, it is found that the terms proportional to ϵ_1 or ϵ_2 contain only two linear combinations of the diagonal density matrix elements, $\rho_{aa} - \rho_{bb}$ and $\rho_{bb} - \rho_{cc}$. It is therefore useful to transform the diagonal elements as follows:

$$d = Sp \quad (A9)$$

where ρ here is a column vector containing the diagonal elements of the density matrix,

$$\mathbf{d} = \begin{pmatrix} d_1 \\ d_2 \\ d_3 \end{pmatrix} = \begin{pmatrix} \rho_{aa} - \rho_{bb} \\ \rho_{bb} - \rho_{cc} \\ \rho_{aa} + \rho_{bb} + \rho_{cc} \end{pmatrix}, \quad (\text{A10})$$

and

$$\mathbf{S} = \begin{pmatrix} 1 & -1 & 0 \\ 0 & 1 & -1 \\ 1 & 1 & 1 \end{pmatrix}. \quad (\text{A11})$$

Then, if the relaxation dependence of ρ is written

$$\dot{\rho} = -\Gamma_{\rho} (\rho - \rho^{(0)}), \quad (\text{A12})$$

after transformation

$$\dot{\mathbf{d}} = -\Gamma_{\mathbf{d}} (\mathbf{d} - \mathbf{d}^{(0)}) \quad (\text{A13})$$

where

$$\Gamma_{\mathbf{d}} = \mathbf{S} \Gamma_{\rho} \mathbf{S}^{-1}. \quad (\text{A14})$$

For our system, in which levels a, b, and c are in different vibrational states, we assume that Γ_{ρ} is an ordinary diagonal matrix with elements γ_a , γ_b , and γ_c . Then,

$$\Gamma_d = -\frac{1}{3} \begin{pmatrix} -(2\gamma_a + \gamma_b) & \gamma_b - \gamma_a & \gamma_b - \gamma_a \\ \gamma_b - \gamma_c & -(\gamma_b + 2\gamma_c) & \gamma_c - \gamma_b \\ -2\gamma_a + \gamma_b + \gamma_c & -\gamma_a - \gamma_b + 2\gamma_c & -(\gamma_a + \gamma_b + \gamma_c) \end{pmatrix}. \quad (A15)$$

If $\gamma_a = \gamma_b = \gamma_c = \gamma_p$, which should be approximately true for methyl fluoride, Γ_d is diagonal with diagonal elements γ_p . In this case, d_3 is decoupled from d_1 and d_2 . This is the approximation that was employed here, though for slightly greater generality, d_1 and d_2 are allowed to have different relaxation parameters, γ_1 and γ_2 . As a final point concerning the relaxation matrix, we assume that collisions cause only loss of coherence; i.e., there is no collisional coherence transfer. Therefore, d_{ba} , d_{cb} , and d_{ca} decay with collisional relaxation parameters γ_{ba} , γ_{cb} , and γ_{ca} respectively.

The result of all this is to produce a system of 8 linear equations for the density matrix elements, as follows:

$$Ad = \Gamma d^0 \quad (A16)$$

in which the transposes of d and d^0 are

$$\tilde{d} = \begin{pmatrix} d_1 & d'_{ba} & d''_{ba} & d'_{ca} & d''_{ca} & d_2 & d'_{cb} & d''_{cb} \end{pmatrix}, \quad (A17)$$

and

$$\tilde{d}^0 = \begin{pmatrix} d_1^0 & 0 & 0 & 0 & 0 & d_2^0 & 0 & 0 \end{pmatrix}; \quad (A18)$$

the matrix A is

$$A = \begin{pmatrix} \gamma_1 & 0 & 2x_1 & 0 & 0 & 0 & 0 & -x_2 \\ 0 & \gamma_{ba} & \delta_1 & 0 & \frac{x_2}{2} & 0 & 0 & 0 \\ -\frac{x_1}{2} & -\delta_1 & \gamma_{ba} & -\frac{x_2}{2} & 0 & 0 & 0 & 0 \\ 0 & 0 & \frac{x_2}{2} & \gamma_{ca} & \delta_3 & 0 & 0 & -\frac{x_1}{2} \\ 0 & -\frac{x_2}{2} & 0 & -\delta_3 & \gamma_{ca} & 0 & \frac{x_1}{2} & 0 \\ 0 & 0 & -x_1 & 0 & 0 & \gamma_2 & 0 & 2x_2 \\ 0 & 0 & 0 & 0 & -\frac{x_1}{2} & 0 & \gamma_{cb} & \delta_2 \\ 0 & 0 & 0 & \frac{x_1}{2} & 0 & -\frac{x_2}{2} & -\delta_2 & \gamma_{cb} \end{pmatrix}; \quad (A19)$$

and Γ is a diagonal matrix whose non-zero values are equal to the diagonal values of A . Also,

$$d_{jk} = d'_{jk} + id''_{jk}, \quad (A20)$$

$$x_1 = \frac{\mu_{ba} \epsilon_1}{h}, \quad (A21)$$

$$x_2 = \frac{\mu_{cb} \epsilon_2}{h}, \quad (A22)$$

$$\delta_1 = s_1 v_1 \left(1 - \frac{v_z}{c} \right) - v_{ba}, \quad (A23)$$

and

$$\delta_2 = s_2 v_z \left(1 - p \frac{v_z}{c} \right) - v_{cb}. \quad (\text{A24})$$

In these equations v_z is the component of the molecular velocity in the direction of beam 1, c is the speed of light, and $p = \pm 1$ for copropagating or counterpropagating beams, respectively.

If we assume that beam 2 is the probe beam that is detected and analyzed, then the absorption coefficient is proportional to the velocity average of d''_{cb} or to

$$f_2 = \frac{s_2}{\sqrt{\pi}u} \int_{-\infty}^{\infty} e^{-\left(v_z/u\right)^2} d''_{cb} dv_z \quad (\text{A25})$$

in which $u^2 = 2k_B T/m$ where k_B is the Boltzmann constant, T is the temperature, and m is the molecular mass. For our work, the integration in eq. (A25) is performed numerically. Normally, the summation is carried out to $v_z = \pm 3u$ with $(v_1/c) \delta v_z$ smaller than the smallest of the relaxation parameters.

The linear system in eq. (A16) may be solved for d''_{cb} algebraically by a technique previously described (14). The result is to give d''_{cb} as a ratio of determinants,

$$d''_{cb} = \frac{\begin{vmatrix} a_{11} & c_1 \\ a_{21} & c_2 \end{vmatrix}}{\begin{vmatrix} a_{11} & a_{12} \\ a_{21} & a_{22} \end{vmatrix}} \quad (\text{A26})$$

in which

$$a_{11} = G_a + \frac{x_1^2}{\gamma_1} + D_n [A_a (B_b D_a - G_a A_a) - D_a (G_b D_a - A_b)] \quad , \quad (\text{A27})$$

$$a_{12} = -B_b - \frac{x_1 x_2}{2\gamma_1} + D_n [A_a (G_a D_b - A_b) - D_a (B_b D_b - G_b A_a)] , \quad (A28)$$

$$a_{21} = -B_b - \frac{x_1 x_2}{2\gamma_2} + D_n [A_a (G_b D_a - A_b) - D_b (B_b D_a - G_a A_a)] , \quad (A29)$$

$$a_{22} = G_b + \frac{x_2^2}{\gamma_2} + D_n [A_a (B_b D_b - G_b A_a) - D_b (G_a D_b - A_b)] . \quad (A30)$$

In these equations,

$$c_i = \frac{x_i d_i^0}{2} \quad i = 1, 2 \quad (A31)$$

$$D_n = (B_b^2 - G_a G_b)^{-1} , \quad (A32)$$

$$A_a = \alpha x_1 x_2 , \quad (A33)$$

$$B_b = \beta x_1 x_2 , \quad (A34)$$

$$A_b = A_a B_b , \quad (A35)$$

$$D_a = \delta_1 + \alpha x_2^2 , \quad (A36)$$

$$D_b = \delta_2 + \alpha x_1^2 , \quad (A37)$$

$$G_a = \gamma_{ba} + \beta x_2^2 , \quad (A38)$$

$$G_b = \gamma_{cb} + \beta x_1^2 , \quad (A39)$$

$$\alpha = -\frac{(\delta_1 + \delta_2)}{4[(\delta_1 + \delta_2)^2 + \gamma_{ca}^2]}, \quad (\text{A40})$$

$$\beta = \frac{\gamma_{ca}}{4[(\delta_1 + \delta_2)^2 + \gamma_{ca}^2]}. \quad (\text{A41})$$

Although not needed for the work described here, the absorption coefficient for beam 1 is proportional to

$$f_1 = \frac{s_1}{\sqrt{\pi}u} \int_{-\infty}^{\infty} e^{-(v_z/u)^2} d_{ba}'' dv_z \quad (\text{A42})$$

for which

$$d_{ba}'' = \left| \begin{array}{cc} c_1 & a_{12} \\ c_2 & a_{22} \end{array} \right| / \left| \begin{array}{cc} a_{11} & a_{12} \\ a_{21} & a_{22} \end{array} \right|. \quad (\text{A43})$$

The lineshape functions f_1 and f_2 contain the sum of single resonance and double resonance contributions. The single resonance contribution for detection of beam 2 may be computed from the usual two-level lineshape, which follows from the three-level equations by setting $x_1=0$. The result is

$$f_2^{(S)} = \frac{s_2 c_2 \gamma_{cb}}{\delta_2^2 + \gamma_{cb}^2 + \gamma_{cb} (x_2^2/\gamma_2)}. \quad (\text{A44})$$

The corresponding result for $f_1^{(S)}$ is

$$f_1^{(S)} = \frac{s_1 c_1 \gamma_{ba}}{\delta_1^2 + \gamma_{ba}^2 + \gamma_{ba} \left(x_1^2 / \gamma_1 \right)}. \quad (\text{A45})$$

The pure double-resonance lineshape is then obtained by subtracting the appropriate $f_1^{(S)}$ from f_1 . If the calculation includes a summation over m states, it is necessary to recall that the formula for the absorption coefficient for beam 2 is

$$\alpha_{\text{abs}} = 16\pi^2 N v_{\text{cb}} \mu_{\text{cb}} \left(f_2 - f_2^{(S)} \right) / c \epsilon_2. \quad (\text{A46})$$

Therefore, the $f_2 - f_2^{(S)}$ for each m state must be multiplied by the appropriate value of μ_{cb} before performing the summation.

REFERENCES

1. S. H. Autler and C. H. Townes, *Phys. Rev.* **100**, 703-722 (1955).
2. A. P. Cox, G. W. Flynn, and E. B. Wilson, Jr., *J. Chem. Phys.* **42**, 3094 (1965).
3. H. Jones, in *Modern Aspects of Microwave Spectroscopy*, edited by G. Chantry (Academic, New York, 1979), pp. 123-216.
4. Th. Hansch and P. Toschek, *Z. Physik* **236**, 213-244 (1970).
5. C. Delsart and J.-C. Keller, *J. Phys. (Paris)* **9**, 350-360 (1978).
6. C. Delsart and J.-C. Keller, *J. Phys. B*, **9**, 2769-2775 (1976).
7. M. S. Feld and A. Javan, *Phys. Rev.* **177**, 540 (1969).
8. N. Skribanowitz, M. J. Kelly, and M. S. Feld, *Phys. Rev. A* **6**, 2302-2311 (1976).
9. R. M. Whitley and C. R. Stroud, *Phys. Rev. A* **14**, 1498-1513 (1976).
10. P. R. Berman, P. F. Liao, and J. E. Bjorkholm, *Phys. Rev. A* **20**, 2389-2404 (1979).
11. V. P. Kaftandjian, C. Delsart, and J. C. Keller, *Phys. Rev. A* **23**, 1365-1374 (1979).
12. P. R. Berman and R. Salomaa, *Phys. Rev. A* **25**, 2667-2692 (1982).

13. C. Feuillade, J. G. Baker, and C. Bottcher, *Chem. Phys. Lett.* **40**, 121-125 (1976).
14. S. T. Sandholm and R. H. Schwendeman, *J. Chem. Phys.* **78**, 3476-3482 (1983).
15. M. Takami, *Japan J. Appl. Phys.* **15**, 1063-1071 (1976); **15**, 1889-1897 (1976); **17**, 125-133 (1978).
16. H. W. Galbraith, M. Dubs, and J. I. Steinfeld, *Phys. Rev. A* **26**, 1528-1538 (1982).
17. C. Feuillade and P. R. Berman, *Phys. Rev. A* **29**, 1236-1257 (1984).
18. N. Dam, L. Oudejans, and J. Reuss, *Chem. Phys.* **140**, 217-231 (1990).
19. Y. Matsuo, S. K. Lee, and R. H. Schwendeman, *J. Chem. Phys.* **91**, 3948-3965 (1989).
20. Y. Matsuo and R. H. Schwendeman, *J. Chem. Phys.* **91**, 3966-3975 (1989).
21. U. Shin, Q. Song, and R. H. Schwendeman, *J. Chem. Phys.* **95**, 3964-3974 (1991).
22. C. J. Borde', J. L. Hall, C. V. Kunasz and D. G. Hummer, *Phys. Rev. A* **14**, 236-263 (1976).
23. J. Keilson and J. E. Storer, *Q. Appl. Math.* **10**, 243-253 (1952).
24. C. Freed and A. Javan, *Appl. Phys. Lett.* **17**, 53-56 (1970).
25. G. Magerl, W. Schupita, and E. Bonek, *IEEE J. Quantum Electron.* **QE-18**, 1214-1220 (1982).
26. H.-G. Cho and R. H. Schwendeman, unpublished work.
27. S. K. Lee, R. H. Schwendeman, and G. Magerl, *J. Mol. Spectrosc.* **117**, 416-434 (1986).
28. S. K. Lee, R. H. Schwendeman, R. L. Crownover, D. D. Skatrud, and F. C. DeLucia, *J. Mol. Spectrosc.* **123**, 145-160 (1987).
29. F. R. Petersen, E. C. Beaty, and C. R. Pollock, *J. Mol. Spectrosc.* **102**, 112-122 (1983).
30. C. Freed, L. C. Bradley, and R. G. O'Donnell, *IEEE J. Quantum Electron.* **QE-16**, 1195-1206 (1980).
31. W. Schupita, A. Ullrich, and G. Magerl, *IEEE J. Quantum Electron.* **QE-25**, 2154-2160 (1989).

Chapter 3

Collisionally Induced Rotational and Vibrational Energy Transfer of Methyl Fluoride in Foreign Gases

I. Introduction

Knowledge of the properties of state-to-state collisionally-induced transitions among molecular energy levels is of fundamental importance for understanding the nature of the collisional process and of the intermolecular potentials. Because of the experimental difficulty and the theoretical complexity, much less is known about the principles and mechanisms for collisionally-induced transitions than for radiation-induced transitions. However, recent advances in experimental techniques and the rapid increase in the available speed of numerical computation have opened up new prospects for study in this field. Among the various methods that have been used for the study of collisionally-induced transitions is the technique of four-level double resonance that was pioneered in the microwave region by Oka (1-2) and that has been used since in almost every range of the electromagnetic spectrum. Examples include four-level double resonance experiments that have been performed by combining infrared techniques with techniques in the radiofrequency region (3-5), through the microwave (6-12), millimeter-wave (13-15), and infrared (16-38) regions to the visible and ultraviolet regions (39-44).

A very important advantage of infrared-infrared double resonance is related to the fact that the Doppler width at the infrared frequencies is large compared to both the available resolution and the inhomogeneous width for low-pressure gases. This makes it possible to monitor double resonance effects as a function of the component of the velocity of the molecules in the direction of the beam and therefore provide information about changes in velocity upon collision. Recently, infrared-infrared double resonance experiments of the type just described were reported for $^{15}\text{NH}_3$ (35), $^{13}\text{CH}_3\text{F}$ (36) and $^{12}\text{CH}_3\text{F}$ (38) from this laboratory. In these experiments, a rovibrational transition in a fundamental band was pumped while a rovibrational transition in a hot band was probed. The lineshape of the probing transition was found to be a superposition of a broad Gaussian and a sharp spike. The Gaussian component was interpreted to be the result of the near resonant vibration-vibration (V-V) energy transfer, in which the pumped molecule swapped vibrational energy with a molecule in the ground vibrational state. In this process, the molecules transferred to the probed level were not the molecules that were pumped. These molecules came from a near thermal equilibrium distribution and the resulting contribution to the probe transition was a Gaussian function with the expected Doppler width. The spike component was assumed to be the result of the direct collisionally-induced transition, where the pumped molecules find themselves at the lower state of the probe as a result of collisions. Since the pumped molecules had a very narrow distribution of the velocity component in the direction of the beam and the collisionally-induced transitions occur without much change in velocity for the system investigated, the resulting contribution to the line shape of the probe transition was a sharp spike.

In the experiments just described the spike components were observed only when the K quantum numbers of the lower level of the probe transition and the

upper level of the pump transition satisfied the selection rule $K(\text{probe}) - K(\text{pump}) = 3n$, where n is a positive or negative integer or zero. This is the selection rule found by Oka many years ago (1,2) for collisionally-induced rotational transitions in C_{3v} molecules. It was found that a phenomenological collision kernel that was a sum of two Keilson-Storer kernels (Ref.(45); equation given below on P. 57) represented the velocity changes during the collisionally-induced transition very well. One of the parameters in the K-S kernel can be interpreted to be the r.m.s. change in speed upon collision. By numerical fitting of the theoretical lineshape obtained from the phenomenological kernel to the observed spectrum, values of the r.m.s. speed change for several transitions were determined.

The previous studies from this laboratory of velocity change during collisionally-induced transitions were the results of self-collisions between dipolar molecules (35-38). In the present study, we describe the results of energy transfer in CH_3F when colliding with different foreign gases. There were three motivations for undertaking this work. First, we wanted to learn more about the correlations of velocity change and state change for collisions in which the dipole-dipole interaction was not the dominant effect. We also wanted to find out how the mass of the perturber would affect the velocity change of the active molecule during the collision. Both of these questions could be answered by studying samples of dilute methyl fluoride in different monatomic gases or nonpolar molecules. Second, unlike the self-collisions of methyl fluoride, where the V-V process plays an important role in transferring population to the probed level, for methyl fluoride-foreign gas collisions, only the direct energy transfer process dominates the contribution to the spectra. This is because the V-V process is either completely absent (as when the foreign gas is an atomic species) or it involves excitation of foreign gas molecules whose spectra are not probed. This allows us to distinguish

the direct energy transfer process from the V-V process. The advantage of this is to observe the effect of the direct transfer without the complication of the V-V transfer. This advantage can be employed in the study of rotationally-resolved direct vibrational energy transfer from the $v_3=1$ to $v_6=1$ vibrational state in $^{12}\text{CH}_3\text{F}$, which was made possible by the recent assignment of high resolution spectra in the $v_3 + v_6 - v_6$ hot band for the molecule (46). In pure methyl fluoride these effects are dominated by the V-V processes.

The final motivation of the study was concerned with the phenomenological collision kernel that is a sum of two K-S kernels and that has been used to describe the velocity change during the collisionally-induced transition (35-38). The K-S collision kernel was originally introduced to describe Brownian motion (45) and then applied to other collisional problems because of its simplicity (47, 48). One of the most important reasons we used this kernel, in addition to its simplicity, was that the theoretical line shape derived from the kernel described the experimental observations very well, but we wanted further evidence to justify the use of the phenomenological collision kernel in our study. For this purpose, we used the method of Borenstein and Lamb (47) to calculate one-dimensional collision kernels from the classical elastic scattering theory using Lennard-Jones or Buckingham-Slater intermolecular potential functions (49). It turned out that the calculated kernel and a sum of the two K-S kernels had in general the same shape.

The classical calculation of elastic collision kernels also helped explain the line shapes of the observed spectra. Although the collision process in our experiment is not elastic, and probably not classical, the change in internal energy and angular momentum for collisionally-induced rotational transitions is small compared to the energy and angular momentum of the collision, and classical scattering calculations often give a view of the collision process that is at least qualitatively

correct. In spite of the simplicity of the model and the crudeness of the potential function, it turns out that by adding consideration of the collision diameter, as obtained for example from lineshape measurements, the calculated collision kernels provide a useful and instructive view of the experimental lineshapes.

II. Experimental Details

The double resonance spectrometer used for this work was identical to that used for the study described in Chapter 2 except that a 2 meter sample cell was used and the chopping frequency for the pump was 150 Hz. We needed a longer optical path because the densities of sample molecules used in this study were lower and the absorptions were much weaker. A slower pump chopping frequency was used because we were studying the energy transfer process and we wanted the period of the pump on or the pump off to be substantially longer than the time required for the molecules to reach the steady state. By contrast, for the three-level double resonance spectra described in Chapter 2, the four-level double resonance effects should be eliminated as much as possible.

All of the gases were commercial samples used without further purification. Sample mixtures were prepared by adding gases to the sample cell at the appropriate pressures, which were measured by means of a capacitance manometer. Typical pump powers at the entrance of the sample cell were ~ 1 W while probe powers were $\sim 20 \mu\text{W}$. All spectra were recorded at room temperature, ~ 297 K.

The lasers and microwave frequency offsets for the transitions studied in this work were taken from previous reports from this laboratory (46,50,51) and are

shown in Table 3.1. The laser frequencies for the various CO₂ isotopic species were calculated from the molecular constants reported in Refs. (52,53).

III. Theoretical Detail

For calculation of the one-dimensional collisional kernel by the procedure of Borenstein and Lamb (47), we consider the interaction of an active molecule and a perturber which, at time $-t$, are at $\mathbf{r}_a = \mathbf{r}_a^0$ and $\mathbf{r}_p = \mathbf{r}_p^0$, respectively, defined in a space-fixed coordinate system; the initial unperturbed velocities of these molecules are \mathbf{v}_a^0 and \mathbf{v}_p^0 , respectively, in the same space-fixed frame. It is well known that the motion of the active molecule is in the plane defined by the initial vector connecting the two particles, $\mathbf{r}^0 = \mathbf{r}_a^0 - \mathbf{r}_p^0$, and the initial relative velocity vector, $\mathbf{v}^0 = \mathbf{v}_a^0 - \mathbf{v}_p^0$ (49). Borenstein and Lamb have shown that if \mathbf{v}_a' is the asymptotic velocity of the active molecule long after the interaction, then in the space-fixed frame (47),

$$\mathbf{v}_a' = \mathbf{v}_a^0 + \Delta \mathbf{v}_a$$

where

$$\Delta \mathbf{v}_a = \frac{m_p}{m_a + m_p} v^0 [\sin \Theta \mathbf{q} - (1 - \cos \Theta) \mathbf{p}] \quad (\text{A1})$$

in which m_a and m_p are the masses of the active and perturber molecules, respectively; v^0 is the magnitude of \mathbf{v}^0 , the initial relative velocity; Θ is the angle between the extension of \mathbf{v}^0 and \mathbf{v}' , the asymptotic relative velocity long after the collision; and \mathbf{p} and \mathbf{q} are unit vectors in the scattering plane defined such that \mathbf{p} is in the original direction of \mathbf{v}^0 and \mathbf{q} is perpendicular to \mathbf{p} . The unit vector \mathbf{q} is in the direction of \mathbf{b} , whose length and direction are defined to be the length and

Table 3.1. Pump and Probe Transitions Used for Double Resonance

Sample	Transition	Band	Symmetry	Frequency ^a	Offset ^{b,c}	Laser
Pump Transitions						
¹³ CH ₃ F	Q _R (4,3)	ν_3	A	31 042 693. 8	-24. 26	¹² C ¹⁶ O ₂ 9P(32)
¹² CH ₃ F	Q _Q (12,1)	ν_3	E	31 383 841. 7	-58. 71	¹² C ¹⁶ O ₂ 9P(20)
¹² CH ₃ F	Q _Q (12,2)	ν_3	E	31 383 940. 1	39. 70	¹² C ¹⁶ O ₂ 9P(20)
¹² CH ₃ F	Q _R (11,9)	ν_3	A	31 998 588. 1	-26. 10	¹² C ¹⁸ O ₂ 9P(22)
Probe Transitions						
¹³ CH ₃ F	Q _R (5,3)	ν_3	A	31 088 539. 2	-12 952. 96	¹² C ¹⁶ O ₂ 9P(30)
¹³ CH ₃ F	Q _P (6,3)	$2\nu_3 - \nu_3$	A	30 040 816. 7	-12 712. 01	¹³ C ¹⁶ O ₂ 9P(18)
¹³ CH ₃ F	Q _P (7,0)	$2\nu_3 - \nu_3$	A	29 987 762. 1	-10 888. 01	¹³ C ¹⁶ O ₂ 9P(20)
¹³ CH ₃ F	Q _P (7,1)	$2\nu_3 - \nu_3$	E	29 987 793. 1	-10 856. 95	¹³ C ¹⁶ O ₂ 9P(20)
¹³ CH ₃ F	Q _P (7,2)	$2\nu_3 - \nu_3$	E	29 987 886. 9	-10 763. 20	¹³ C ¹⁶ O ₂ 9P(20)
¹³ CH ₃ F	Q _P (7,3)	$2\nu_3 - \nu_3$	A	29 988 045. 1	-10 605. 03	¹³ C ¹⁶ O ₂ 9P(20)
¹³ CH ₃ F	Q _P (7,4)	$2\nu_3 - \nu_3$	E	29 988 270. 6	-10 379. 44	¹³ C ¹⁶ O ₂ 9P(20)
¹³ CH ₃ F	Q _P (7,5)	$2\nu_3 - \nu_3$	E	29 988 568. 1	-10 081. 95	¹³ C ¹⁶ O ₂ 9P(20)
¹³ CH ₃ F	Q _P (7,6)	$2\nu_3 - \nu_3$	A	29 988 943. 6	-9 706. 49	¹³ C ¹⁶ O ₂ 9P(20)
¹² CH ₃ F	Q _P (14,0)	$2\nu_3 - \nu_3$	A	30 197 402. 9	-15 623. 25	¹³ C ¹⁶ O ₂ 9P(12)
¹² CH ₃ F	Q _P (14,1)	$2\nu_3 - \nu_3$	E	30 197 444. 7	-15 581. 38	¹³ C ¹⁶ O ₂ 9P(12)
¹² CH ₃ F	Q _P (14,2)	$2\nu_3 - \nu_3$	E	30 197 571. 0	-15 455. 13	¹³ C ¹⁶ O ₂ 9P(12)
¹² CH ₃ F	Q _P (14,3)	$2\nu_3 - \nu_3$	A	30 197 783. 9	-15 242. 28	¹³ C ¹⁶ O ₂ 9P(12)
¹² CH ₃ F	Q _P (14,4)	$2\nu_3 - \nu_3$	E	30 198 087. 0	-14 939. 16	¹³ C ¹⁶ O ₂ 9P(12)
¹² CH ₃ F	Q _P (14,5)	$2\nu_3 - \nu_3$	E	30 198 485. 7	-14 540. 44	¹³ C ¹⁶ O ₂ 9P(12)
¹² CH ₃ F	Q _R (7,1,-1)	$\nu_3 + \nu_6 - \nu_6$	E	31 531 894. 1	-12 134. 83	¹² C ¹⁶ O ₂ 9P(14)
¹² CH ₃ F	Q _R (9,3,1)	$\nu_3 + \nu_6 - \nu_6$	E	31 632 525. 7	-14 317. 71	¹² C ¹⁶ O ₂ 9P(10)
¹² CH ₃ F	Q _R (10,2,-1)	$\nu_3 + \nu_6 - \nu_6$	A	31 661 334. 5	14 491. 07	¹² C ¹⁶ O ₂ 9P(10)
¹² CH ₃ F	Q _R (12,0)	$2\nu_3 - \nu_3$	A	31 556 943. 0	12 914. 16	¹² C ¹⁶ O ₂ 9P(14)
¹² CH ₃ F	Q _R (12,1)	$2\nu_3 - \nu_3$	E	31 556 957. 2	12 928. 33	¹² C ¹⁶ O ₂ 9P(14)
¹² CH ₃ F	Q _R (12,2)	$2\nu_3 - \nu_3$	E	31 557 000. 4	12 971. 51	¹² C ¹⁶ O ₂ 9P(14)
¹² CH ₃ F	Q _R (12,3)	$2\nu_3 - \nu_3$	A	31 557 074. 6	13 045. 71	¹² C ¹⁶ O ₂ 9P(14)
¹² CH ₃ F	Q _R (12,4)	$2\nu_3 - \nu_3$	E	31 557 183. 2	13 154. 33	¹² C ¹⁶ O ₂ 9P(14)
¹² CH ₃ F	Q _R (12,5)	$2\nu_3 - \nu_3$	E	31 557 331. 2	13 302. 29	¹² C ¹⁶ O ₂ 9P(14)
¹² CH ₃ F	Q _R (12,6)	$2\nu_3 - \nu_3$	A	31 557 525. 1	13 496. 18	¹² C ¹⁶ O ₂ 9P(14)
¹² CH ₃ F	Q _R (12,7)	$2\nu_3 - \nu_3$	E	31 557 773. 3	13 744. 43	¹² C ¹⁶ O ₂ 9P(14)
¹² CH ₃ F	Q _R (12,8)	$2\nu_3 - \nu_3$	E	31 558 086. 4	14 057. 55	¹² C ¹⁶ O ₂ 9P(14)
¹² CH ₃ F	Q _R (12,9)	$2\nu_3 - \nu_3$	A	31 558 477. 2	14 448. 36	¹² C ¹⁶ O ₂ 9P(14)

^aCenter frequency of the transition in MHz.^bCenter frequency of the transition minus the CO₂ laser frequency in MHz.^cLaser frequencies calculated from the constants in References (52) and (53).

direction, respectively, of $\mathbf{r}_a - \mathbf{r}_p$ at the point of closest approach for the condition of no interacting potential.

The one-dimensional collision kernel that is of interest in this work is the quantity $W(v_Z, v_Z') dv_Z'$ which is defined to be the probability per unit time that an active molecule with initial space-fixed Z-component of velocity v_Z has its final Z-component of velocity between v_Z' and $v_Z' + dv_Z'$. To compute $W(v_Z, v_Z')$ we follow Borenstein and Lamb (47) and calculate $v_Z' = v_{aZ}'$ for a large number of randomly-chosen scattering events for a single active molecule with initial Z-component of velocity equal to $v_Z = v_{aZ}^0$. We set up inside the computer a number of bins of width dv_Z and increment the count in the appropriate bin for each calculated value of v_{aZ}' . In order to make a random selection of scattering events, we set up a new particle-fixed coordinate system centered at the perturber, but rotated from the space-fixed frame so that the new z axis is in the direction of \mathbf{v}^0 (Fig. 3.1). The new y axis is in the direction of \mathbf{b} and therefore in the plane of \mathbf{r}^0 and \mathbf{v}^0 ; the y axis is assumed to make an angle χ with the line of nodes, the intersection of the space-fixed XY and the new particle-fixed xy planes, as defined by Wilson, Decius, and Cross (WDC) (54). The new x axis completes a right-handed coordinate system and is in the direction of the collisional angular momentum, $\mathbf{L} = \mu \mathbf{r}^0 \times \mathbf{v}^0$. The initial space-fixed Z component of the velocity of the active molecules is fixed for all scattering events, while for each event the initial space-fixed X and Y components of this velocity as well as all three components of the initial space-fixed velocity of the perturber are randomly chosen from the appropriate Boltzmann distributions defined by the assumed particle masses and the temperature.

To take into account all of the possible relative positions of the active molecules and perturber at time $-t$, we assume that the tip of \mathbf{r}^0 in the center of mass frame

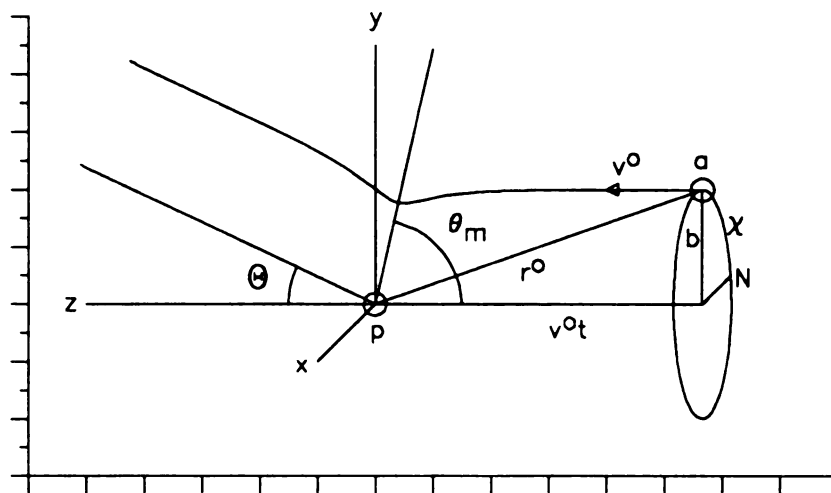


Figure 3.1 Diagram of the scattering plane for a single scattering event between an active molecule (a) and a perturber (p). The curved path of the active molecule is symmetric about the line that makes an angle θ_m with the -z axis. In the figure, $\Theta = \pi - 2\theta_m$ is the scattering angle; r^0 is the initial separation of a and p; v^0 is the initial relative velocity; b , which is parallel to the y axis, is the magnitude of the impact parameter; and χ is the angle between b and a line (N) that is parallel to the line of nodes.

lies in an element of volume of magnitude $dV = v^0 dt db b d\chi$ that is located by cylindrical coordinates $(b, \chi, z=v^0 t)$ in the center-of-mass frame (Fig. 3.1); t is the time that would be required for the active molecule to reach the position of closest approach to the scattering center for the case of no interacting potential. The final value of v'_{aZ} is independent of t , so that if the probability of an encounter for $\mathbf{v}=\mathbf{v}^0$ with r_0 in the range defined by $t, t+dt, b, b+db, \chi$, and $\chi + d\chi$ is

$$P v^0 b dt db d\chi$$

then the probability per unit time for such an encounter is

$$P v^0 b db d\chi.$$

To calculate v'_{aZ} , we write

$$v_{aZ}' = v_{aZ}^0 + \Delta v_{aZ}$$

where

$$\Delta v_{aZ} = \frac{m_p}{m_a + m_p} v^0 [\sin\Theta \mathbf{q} \cdot \mathbf{k} - (1 - \cos\Theta) \mathbf{p} \cdot \mathbf{k}]$$

in which \mathbf{k} is a unit vector in the space-fixed Z direction. According to WDC (54), the direction cosines are

$$\mathbf{p} \cdot \mathbf{k} = \cos\theta$$

and

$$\mathbf{q} \cdot \mathbf{k} = \sin\theta \sin\chi,$$

where θ is the angle between the Z and z axes. In our case,

$$\cos\theta = v_Z^0 / v^0$$

and

$$\sin\theta = \left(v^0{}^2 - v_Z^0{}^2\right)^{\frac{1}{2}} / v^0.$$

Therefore,

$$\Delta v_{aZ} = \frac{m_p}{m_a + m_p} \left[\left(v^0{}^2 - v_Z^0{}^2\right)^{\frac{1}{2}} \sin\chi \sin\Theta - v_Z^0 (1 - \cos\Theta) \right].$$

Finally, to complete the integration, the impact parameter b is randomly selected from the range 0 to b (max) and the angle χ is randomly selected from the range 0 to 2π . Then, after calculation of v'_{aZ} , the appropriate v_Z' bin is identified and incremented by bv^0 . If the number of events is made very large, the result should be proportional to the classical collision kernel for the assumed masses, temperature, and interaction potential. Normalization can be achieved by multiplying the contents of each bin by the number of molecules per unit volume and dividing each result by the sum of the bv^0 values for all of the events.

For these initial calculations, two potential functions were chosen: the Lennard-Jones 6- γ function (49),

$$V(r) = \frac{6\epsilon}{\gamma-6} \left[\left(\frac{r_e}{r}\right)^\gamma - \frac{\gamma}{6} \left(\frac{r_e}{r}\right)^6 \right],$$

and the Buckingham-Slater potential (49),

$$V(r) = \frac{6\epsilon}{\gamma-6} \left[\exp\left[\gamma\left(1 - \frac{r}{r_e}\right)\right] - \frac{\gamma}{6} \left(\frac{r_e}{r}\right)^6 \right].$$

In these equations, ϵ is the well depth at the equilibrium value of $r = r_e$.

Unfortunately, we have no specific information about the value of ϵ and r_e to use for this purpose. Consequently, a number of calculations were performed with $\epsilon /$

k_B (k_B is the Boltzmann constant) in the range 100-500 K and r_e in the range of 3.5-4.5 Å. These ranges were selected on the basis of examination of Table I-A in Ref. (55).

Most of the calculations were performed with the Lennard-Jones 6-12 potential, but a few Buckingham-Slater calculations were performed to test the dependence of the shape of the collision kernel on the repulsive part of the potential curve. Since the results for the two potentials were not qualitatively different, the Lennard-Jones 6-12 potential was used exclusively after these tests were completed.

For comparison with the lineshapes of the transferred spikes that were measured and analyzed in our previous work, some of the calculated collision kernels were fit by least squares to a sum of Keilson-Storer collision kernels (45),

$$W(v_Z, v'_Z) = \sum \frac{A_i}{\sqrt{\pi}\beta_i} \exp\left[-(v'_Z - \alpha_i v_Z)^2 / \beta_i^2\right]$$

in which $\alpha_i^2 = 1 - \beta_i^2 / u^2$ where $u^2 = 2 k_B T / m$, with T the temperature and m the molecular mass; the A_i are expansion coefficients and the β_i may be interpreted as $\sqrt{2}$ times the r.m.s. change in the Z component of the velocity as a result of collision for the molecules that contribute to the i th component of the expansion.

IV. Experimental Results

A. Foreign gas effects on the double-resonance lineshape

The effects of five different foreign gases ($^{12}\text{CH}_3\text{F}$, H_2 , He , Ar , and Xe) on the

lineshapes of infrared-infrared four-level double resonance in $^{13}\text{CH}_3\text{F}$ have been investigated. In Figure 2, the spectra of 3 mTorr $^{13}\text{CH}_3\text{F}$ in 50 mTorr of different foreign gases were each compared to the spectrum of 7 mTorr pure $^{13}\text{CH}_3\text{F}$ sample for the $^{\text{Q}}\text{P}(6,3)$ probe transition in the $2\nu_3 - \nu_3$ hot band while the $^{\text{Q}}\text{R}(4,3)$ transition in the ν_3 fundamental band was pumped. The dotted traces are the spike and Gaussian components in the observed spectrum separated by the least squares fitting program used in Ref. 35. It is apparent that for collisions with $^{12}\text{CH}_3\text{F}$ (Fig. 3.2b), H_2 (Fig. 3.2c), and He (Fig. 3.2d), a transferred spike with substantial intensity is seen, whereas for Ar (Fig. 3.2e) and Xe (Fig. 3.2f) the lineshape is mostly a broad Gaussian shape. The same experiments were repeated with different ratios of the partial pressures of the sample and foreign gas and the qualitative pattern of the line shapes did not change.

In contrast to methyl fluoride self collisions, where the spike components were attributed to direct rotational energy transfer and the Gaussian component to the near resonant V-V transfer, for methyl fluoride - foreign gas collisions, both spike and Gaussian components are results of the direct rotational energy transfer processes. The reason has already been mentioned for this: that for perturbers that do not have vibrational energy levels (e.g. He , Ar and Xe), the V-V process simply does not exist, while for perturbers that have vibrational levels, for which the V-V process can occur (e.g. $^{13}\text{CH}_3\text{F}$ - $^{12}\text{CH}_3\text{F}$ collision), the result of the V-V process is to increase the population of a vibrationally excited state of the perturber, which is not probed.

The spike component of the lineshapes includes a contribution from pumped molecules whose velocity underwent little change during the rotationally inelastic collision. This is an indication of a weak collision, where conversion from rotational energy to translational energy is small and the molecular path is not

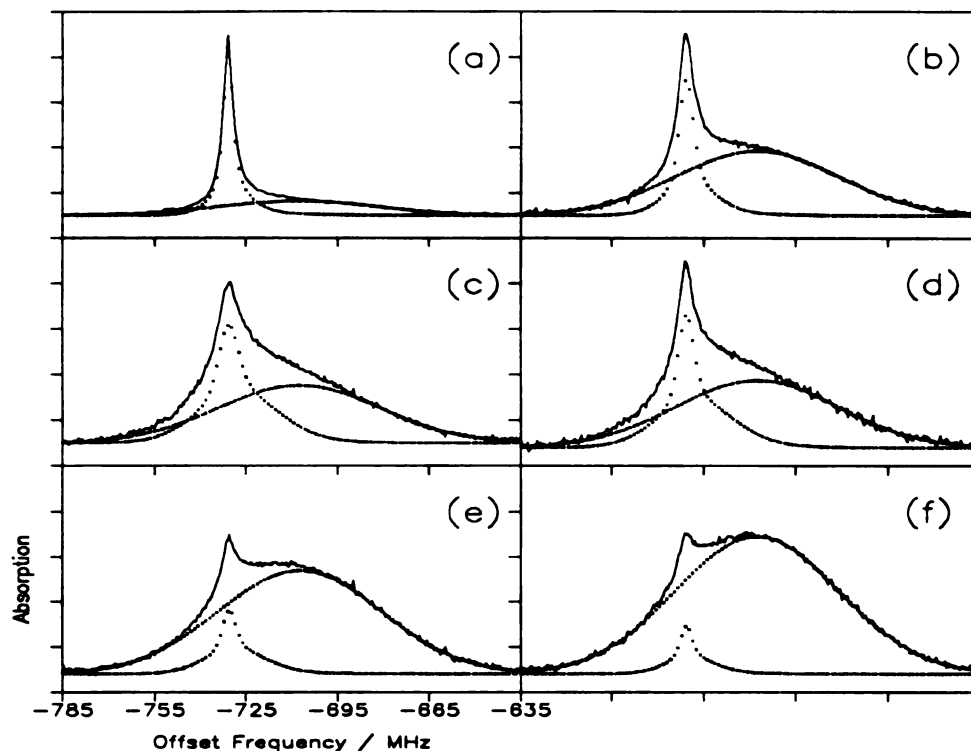


Figure 3.2 Spectra of the QP(6,3) transition in the $2\nu_3$ - ν_3 band in $^{13}\text{CH}_3\text{F}$ taken for a variety of collision partners; the spike and Gaussian components for each lineshape are also shown. Trace (a) is a single resonance spectrum in a pure sample at 7 mTorr; Traces (b) - (f) are double resonance spectra recorded while the QR(4,3) transition in the ν_3 band was pumped. The samples for the double resonance spectra were 3 mTorr of $^{13}\text{CH}_3\text{F}$ in 50 mTorr of foreign gas, as follows: (b) $^{12}\text{CH}_3\text{F}$; (c) H_2 ; (d) He; (e) Ar; (f) Xe. The infrared frequencies for each spectrum are the horizontal axis values shown for (e) plus 30 041 529 MHz.

deflected significantly. The weak collision may be due to the effect of a long range intermolecular force at a large collisional impact parameter, or a light perturber. The broad Gaussian components in Fig. 3.2 have widths that are comparable to the Doppler width (31 MHz) of the probe transition. This component results from pumped molecules whose velocity is completely scrambled during collision. These molecules lose all "memory" of the initial velocity during collision, which is characteristic of a strong collision. For a strong collision, the conversion from rotational energy to translational energy can be large and the molecular path is deflected substantially. A strong collision may result from a small collisional impact parameter, or from a heavy perturber.

The lineshapes in Fig. 3.2 show that collisionally-induced rotational energy transfer without much change of the translational momentum can readily occur between species with substantial dipole moments or between species in which the mass of the perturber is relatively small compared to the mass of the active molecule. Thus, we attribute the existence of the transferred spike in the $^{13}\text{CH}_3\text{F}/^{12}\text{CH}_3\text{F}$ colliding pair (Fig. 3.2b) to the long-range dipole-dipole interaction for which collisions of large impact parameter can induce rotational transitions. The existence of transferred spikes for the $^{13}\text{CH}_3\text{F}/\text{H}_2$ (Fig. 3.2c) and $^{13}\text{CH}_3\text{F}/\text{He}$ (Fig. 3.2d) colliding pairs is attributed to the low mass of the perturber, which is insufficient to cause a substantial change in the velocity of the $^{13}\text{CH}_3\text{F}$ active molecule, even for collisions of relatively low impact parameter. For $^{13}\text{CH}_3\text{F}/\text{Ar}$ (Fig. 3.2e) and $^{13}\text{CH}_3\text{F}/\text{Xe}$ (Fig. 3.2f) colliding pairs, most of the collisionally-induced rotational transitions randomize the velocity. The hard collisions are presumably the result of small impact parameter and/or relatively heavy perturbers.

It is interesting to note that the spike for the $^{13}\text{CH}_3\text{F}/\text{H}_2$ colliding pair (Fig.

3.2c) is broader than the spike for the $^{13}\text{CH}_3\text{F}/\text{He}$ (Fig. 3.2d) colliding pair in spite of the greater mass for He than for H_2 . This may indicate that the form of the intermolecular potential function may be more sensitive in determining the correlation of the velocity change and the state change during the collisionally induced transition.

The qualitative features of the collision kernels that result from different masses of the perturbers, collisional impact parameters and parameters in the potential functions are discussed in Section V. The results from calculations demonstrate most of the tendencies observed above.

B. Selection rule for direct rotational energy transfer

The most important selection rule for collision-induced direct rotational energy transfer in molecules with C_{3v} symmetry is $\Delta k = 3n$ (1-2), where n is a positive or negative integer or zero. Thus, methyl fluoride molecules in an initial state (J, k) find themselves only in the final states (J', k') after collision, where $k' - k = 3n$. Since the selection rule connects rotational states with the same nuclear spin state, we can interpret the selection rule to be the result of the difficulty in changing the nuclear spin state by collisions. In the previous work from this laboratory, where pure methyl fluoride samples were studied (36, 38), double resonance effects were observed for all values of k . This was because collisionally-induced rotational energy transfer occurs by two mechanisms for methyl fluoride self-collision -- direct transfer, and V-V transfer. The direct transfer process obeys the selection rule while the V-V process does not. In the CH_3F -foreign gas sample studied here, because only the direct transfer process is responsible for the double resonance

effects, the selection rule for the collisionally-induced rotational transfer should be clearly seen.

Figure 3.3 shows the energy levels of a four-level system used for observation of the selection rule. The $(J,K) = (5,3)$ level in the $v_3=1$ vibrational state in $^{13}\text{CH}_3\text{F}$ was pumped by absorption of radiation by the $Q_R(4,3)$ transition in the v_3 band, while the $(7,K)$ ($K = |k| = 0-6$) levels in the same vibrational state were probed by absorption of the $Q_P(7,K)$ transitions in the $2v_3 - v_3$ band. Figure 3.4 shows a comparison of the observed spectra for the $Q_P(7,K)$ transitions in the $2v_3 - v_3$ hot band in different experimental conditions. Fig. 3.4 (a) is a regular single resonance spectrum which gives a view of the relative intensities of the probe transition at thermal equilibrium. Fig. 3.4 (b) is a double resonance spectrum for 17 m torr of pure $^{13}\text{CH}_3\text{F}$ sample, in which the transferred spike is obvious only for the $Q_P(7,3)$ transition, but double-resonance effects are seen for all of the transitions. Fig. 3.4 (c) and Fig. 3.4 (d) are double resonance spectra recorded for 1% of $^{13}\text{CH}_3\text{F}$, by volume, in $^{12}\text{CH}_3\text{F}$ and in Ar, respectively, at a total pressure of 100 mTorr. As can be seen in Fig. 3.4 (c) and Fig. 3.4 (d), only the $Q_P(7,0)$, $Q_P(7,3)$, and $Q_P(7,6)$ transitions have appreciable intensity. This is a very good graphic illustration of the $\Delta k = 3n$ selection rule. This selection rule holds for CH_3F -Ar collision as well as for CH_3F - CH_3F collision even though the former is expected to be a much harder collision than latter. In Fig. 3.4 (b) substantial intensities are also seen for the probe transitions with $K=1,2$ and $4,5$. Upon comparison with Figs. 3.4 (c) and 3.4 (d), it is clear that these transitions are the results of the V-V process.

In Figure 3.4, the selection rule was illustrated in ortho methyl fluoride molecules. In order to demonstrate the same selection rule in para methyl fluoride molecules, we simultaneously pumped the $Q_Q(12,2)$ and $Q_Q(12,1)$ transitions (different velocity groups) in the v_3 band of $^{12}\text{CH}_3\text{F}$ and probed $Q_P(14,K)$

Probe P(7,K) (K=0, 1, 2, 3, 4, 5, 6) in $2\nu_3 - \nu_3$ hot band

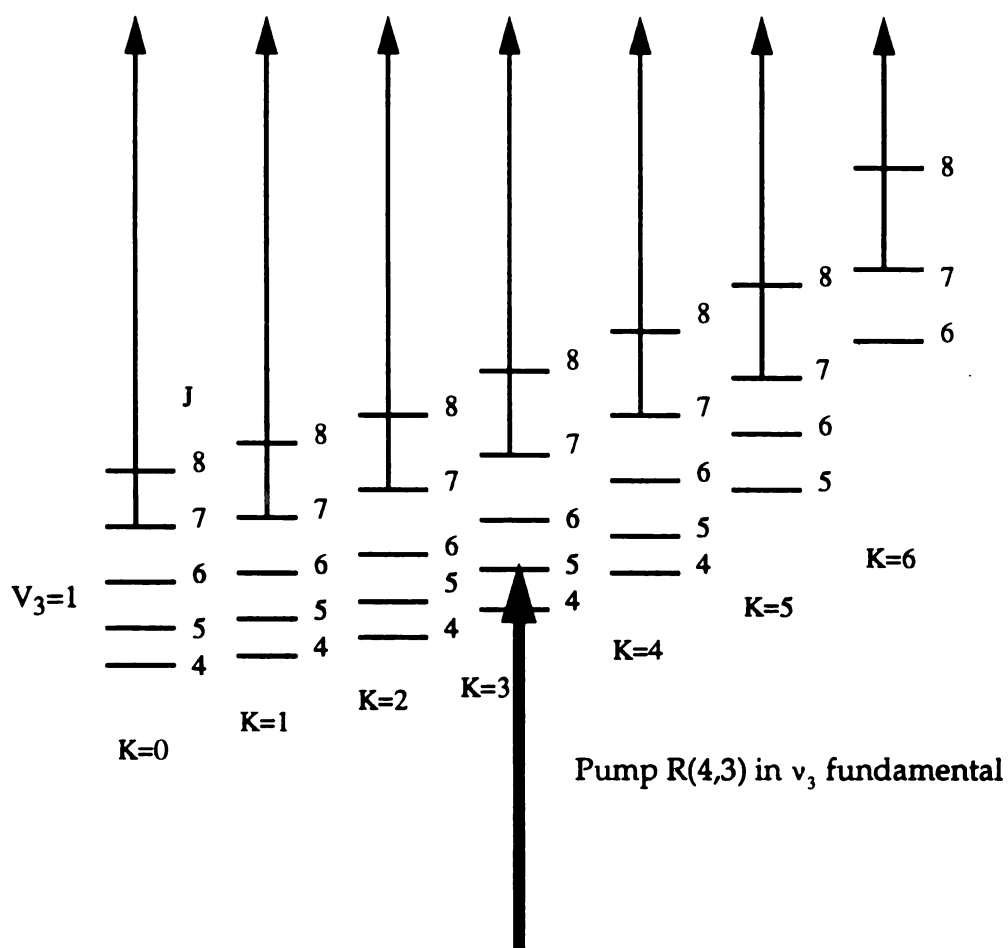


Figure 3.3 Energy level diagram for $^{13}\text{CH}_3\text{F}$ for the double resonance transitions shown in Fig. 3.4. Only the levels for $4 \leq J \leq 8$ and $0 \leq K \leq 6$ in $v_3 = 1$ are shown.

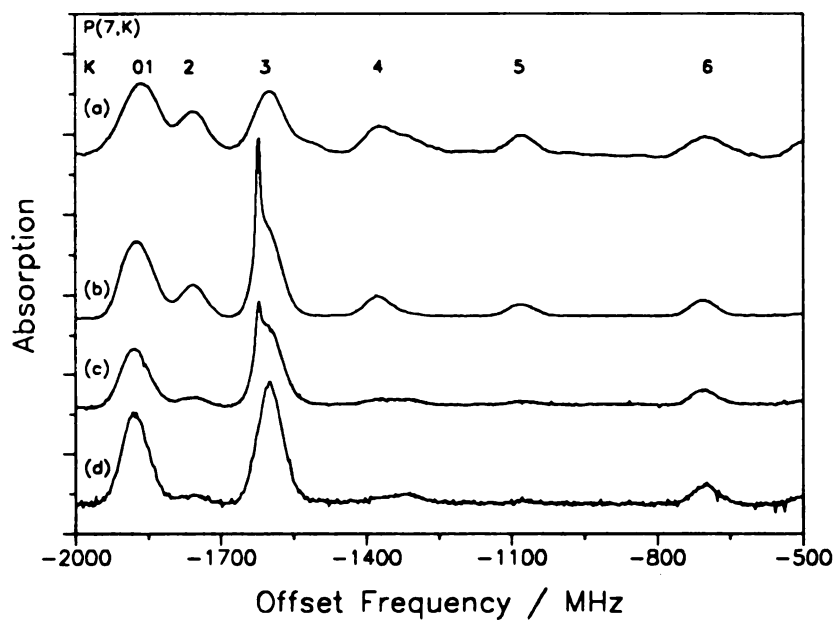


Figure 3.4. Single resonance (a) and double resonance (b-d) spectra of the $QP(7,K)$ transitions for $K \leq 6$ in the $2\nu_3-\nu_3$ band of $^{13}\text{CH}_3\text{F}$. The $QR(4,3)$ transition in the ν_3 band of $^{13}\text{CH}_3\text{F}$ was pumped for the double resonance. The samples were: (a) $^{13}\text{CH}_3\text{F}$ at 30 mTorr; (b) $^{13}\text{CH}_3\text{F}$ at 17 mTorr; (c) 1 mTorr $^{13}\text{CH}_3\text{F}$ in 100 mTorr $^{12}\text{CH}_3\text{F}$; and (d) 1 mTorr $^{13}\text{CH}_3\text{F}$ in 100 mTorr Ar. The infrared frequencies for each spectrum are the horizontal axis value plus 29 989 650 MHz.

transitions with $K = 0-5$ in the $2\nu_3 - \nu_3$ band in the same molecule. Figure 3.5 shows a comparison of the double resonance spectrum recorded for 1% $^{12}\text{CH}_3\text{F}$ in argon at a total pressure of 140 mTorr to the single resonance spectrum for 30 mTorr of pure $^{12}\text{CH}_3\text{F}$. It is clear in Fig. 3.5 (b) that the intensities are substantially increased for the transitions with $K = 1, 2, 4$, and 5 and suppressed for transitions with $K = 0$ and 3.

C. Vibrational energy transfer from $\nu_3 = 1$ to $\nu_6 = 1$

Rotationally selective vibrational energy transfer is a subject of several recent publications. Orr and his coworkers observed selection rules for rotationally specific mode-to-mode vibrational energy transfer from the $\nu_6 = 1$ to the $\nu_4 = 1$ vibrational state in D_2CO self collisions in their infrared-ultraviolet double resonance experiments (41-44). In D_2CO the $\nu_4 = 1$ vibrational level is about 51 cm^{-1} lower than the $\nu_6 = 1$ level. In $^{12}\text{CH}_3\text{F}$ the closest vibrational level to $\nu_3 = 1$ is the $\nu_6 = 1$ level, which is approximately 134 cm^{-1} above the $\nu_3 = 1$ level. Although evidence for the energy flow between the $\nu_3 = 1$ and $\nu_6 = 1$ vibrational states in methyl fluoride was reported many years ago (56-57), the existence of direct energy transfer between the two vibrational states was not clear. The assignment of the high resolution spectrum of the $\nu_3 + \nu_6 - \nu_6$ hot band in $^{12}\text{CH}_3\text{F}$ (46) provides a convenient way to probe the population in a specific rotational level in the $\nu_6 = 1$ vibrational state. By probing the spectra in the $\nu_3 + \nu_6 - \nu_6$ hot band while pumping a transition in the ν_3 fundamental for a $^{12}\text{CH}_3\text{F}$ sample in excess of foreign gas, the collisionally-induced rotationally specific direct vibrational energy transfer from $\nu_3 = 1$ to $\nu_6 = 1$ vibrational levels can be studied.

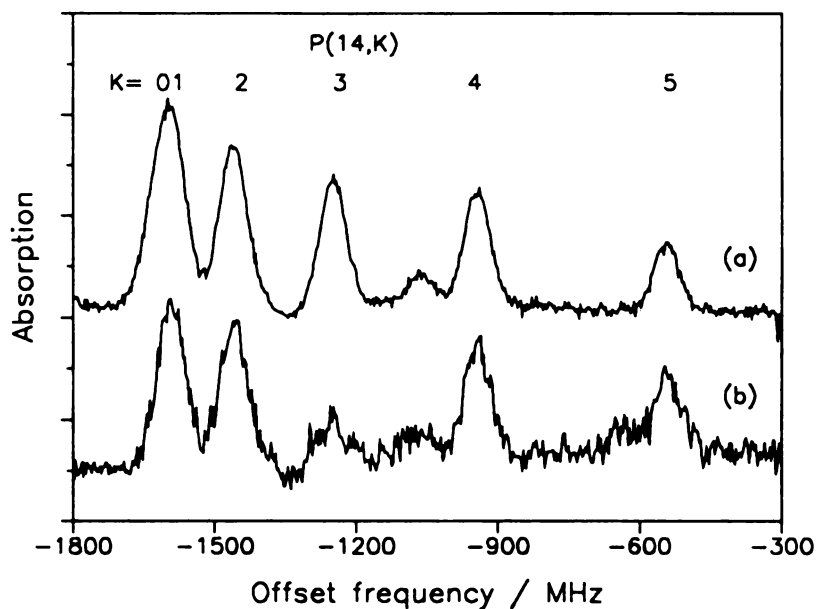


Figure 3.5. Single resonance (a) and double resonance (b) spectra of the $QP(14,K)$ transitions for $K \leq 5$ in the $2\nu_3-\nu_3$ band of $^{12}\text{CH}_3\text{F}$. The $QQ(12,1)$ and $QQ(12,2)$ transitions in the ν_3 band of $^{12}\text{CH}_3\text{F}$ were simultaneously pumped for the double resonance. The samples were: (a) 30 mTorr $^{12}\text{CH}_3\text{F}$; and (b) 1% $^{12}\text{CH}_3\text{F}$ in Ar at 140 mTorr total pressure. The infrared frequencies for each spectrum are the horizontal axis values plus 30 199 026 MHz.

Figure 3.6 is a comparison of single resonance (Fig. 3.6 a) and double resonance spectra (Fig. 3.6 b-d) of the $Q_R(J=9, K=3, l=1)$ transition in the $\nu_3 + \nu_6 - \nu_6$ band in para $^{12}\text{CH}_3\text{F}$ and the $Q_R(10,2,-1)$ transition in the same band in ortho $^{12}\text{CH}_3\text{F}$. The single resonance spectrum was taken with the sample at 500 mTorr pressure while the double resonance spectra were taken at 63 mTorr total pressure with 1% $^{12}\text{CH}_3\text{F}$ in Ar for Figs. 3.6b and 3.6c and in $^{13}\text{CH}_3\text{F}$ for Fig. 3.6d. For Fig. 3.6 b, the $Q_Q(12,1)$ and $Q_Q(12,2)$ transitions in the ν_3 band of $^{12}\text{CH}_3\text{F}$ (para levels) were pumped and there is a clear intensity enhancement of the E level (para) transition. By contrast, for Fig. 3.6 c, the $Q_R(11,9)$ transition in the ν_3 band (ortho levels) was pumped and there is a corresponding intensity enhancement of the A level (ortho) transition. In each of these spectra there is a weak double resonance effect at the transition that would result from collisionally-induced ortho-para or para-ortho transitions. We have not yet performed the very careful intensity measurements that would be required to tell whether these are the result of V-V transfer from the relatively small number of $^{12}\text{CH}_3\text{F} - ^{12}\text{CH}_3\text{F}$ collisions in the sample or whether there is a small probability of direct ortho-para transition as a result of $^{12}\text{CH}_3\text{F}$ -Ar collisions. It is clear in Fig. 3.6b and 3.6c that the ortho-ortho (E-E) and para-para (A-A) selection rule, which here must be generalized to $\Delta(k-l) = 3n$, is strongly preferred in the observed double resonance effects. This indicates that the CH_3F -Ar collisions are strong enough to induce direct vibrational energy transfer in CH_3F and the energy transfer process is governed by the symmetry selection rule $\Delta(k-l) = 3n$.

Figure 3.6d shows the double resonance spectrum of 1% $^{12}\text{CH}_3\text{F}$ in $^{13}\text{CH}_3\text{F}$ at 63 mTorr total pressure, recorded for the $Q_Q(12,2)$ - $Q_Q(12,1)$ pump. In this spectrum, almost no double resonance effects are seen. The corresponding spectrum for the $Q_R(11,9)$ pump is almost the same. This indicates that $^{12}\text{CH}_3\text{F}$ -

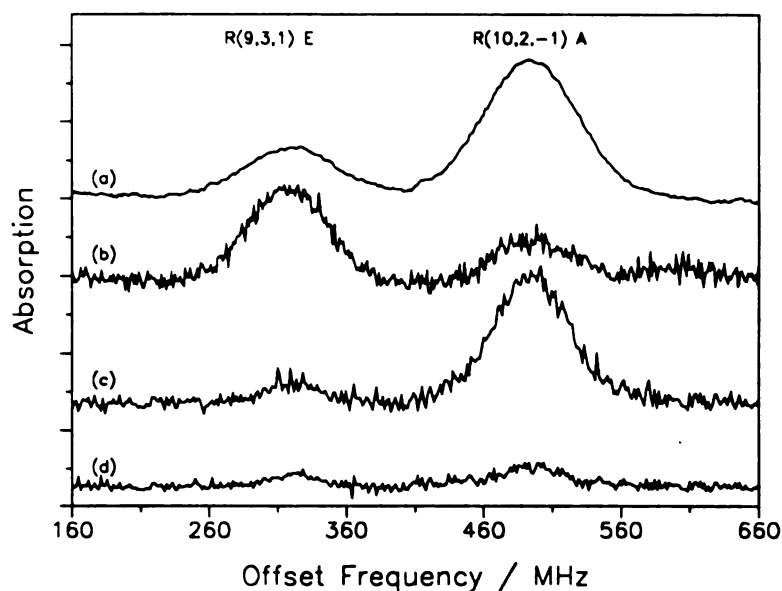


Figure 3.6. Single resonance (a) and double resonance (b-d) spectra of the $QR(9,3,1)$ and $QR(10,2,-1)$ transitions in the $\nu_3+\nu_6-\nu_6$ band of $^{12}\text{CH}_3\text{F}$. The $QQ(12,1)$ and $QQ(12,2)$ transitions in the ν_3 band of $^{12}\text{CH}_3\text{F}$ were simultaneously pumped for the double resonance in (b) and (d), whereas the $QR(11,9)$ transition in the ν_3 band of $^{12}\text{CH}_3\text{F}$ was pumped for (c). The samples were: $^{12}\text{CH}_3\text{F}$ at 500 mTorr for (a); 1% $^{12}\text{CH}_3\text{F}$ in 63 mTorr total pressure of Ar for (b) and (c); and 1% $^{12}\text{CH}_3\text{F}$ in 63 mTorr total pressure of $^{13}\text{CH}_3\text{F}$ for (d). The infrared frequency for the $QR(9,3,1)$ transition is 31 632 843 MHz minus the horizontal axis value, whereas the infrared frequency for the $QR(10,2,-1)$ transition is 31 660 843 MHz plus the horizontal axis value.

$^{13}\text{CH}_3\text{F}$ collisions can hardly induce direct vibrational energy transfer from $\nu_3 = 1$ to $\nu_6 = 1$.

The above observations are understandable. Because of the large energy gap between the $\nu_3=1$ and $\nu_6=1$ vibrational states (134 cm^{-1}) in $^{12}\text{CH}_3\text{F}$, a large energy conversion is required during the energy transfer. This can only occur for a fairly strong collision. A $\text{CH}_3\text{F-Ar}$ collision is a much harder collision than a $\text{CH}_3\text{F-CH}_3\text{F}$ collision, therefore the former can induce the direct vibrational energy transfer in methyl fluoride while the latter cannot.

Although $\text{CH}_3\text{F-CH}_3\text{F}$ collisions do not induce direct vibrational energy transfer, they appear to induce V-V energy transfer quite readily. This can be seen in Fig. 3.7. Figure 3.7a is the single resonance spectrum shown in Fig. 3.6a, while Fig. 3.7b is a double resonance spectrum recorded for 60 mTorr of pure $^{12}\text{CH}_3\text{F}$ while the $Q_Q(12,1)$ and $Q_Q(12,2)$ transitions in the ν_3 band were pumped. Strong double resonance effects are seen in the probe transitions (Fig. 3.7b). Since the ratio of the intensities of the two transitions in the $\nu_3 + \nu_6 - \nu_6$ band is essentially the same for the single resonance (Fig. 3.7a) and the double resonance spectra (Fig. 3.7b), showing no evidence for selection rules, the vibrational energy transfer in pure CH_3F must be the result of the V-V process.

Figure 3.8 shows a comparison of the single and double resonance spectra for the $R(7,1,-1)$ probe transition in the $\nu_3 + \nu_6 - \nu_6$ hot band and the $Q_P(12,k)$ ($k=0,1,2,3\dots 9$) probe transitions in the $2\nu_3 - \nu_3$ band when the $Q_Q(12,1)$ and $Q_Q(12,2)$ in the ν_3 fundamental band was pumped. Two spikes are seen in the spectrum which correspond to the three level double resonance effects for the $Q_P(12,1)$ and $Q_P(12,2)$ transitions, respectively. The double resonance effects for the $Q_R(7,1,-1)$, $Q_P(12,6)$ and $Q_P(12,9)$ transitions are all the result of the V-V process. Thus, by comparing the relative intensities of the $Q_R(7,1,-1)$ transition in

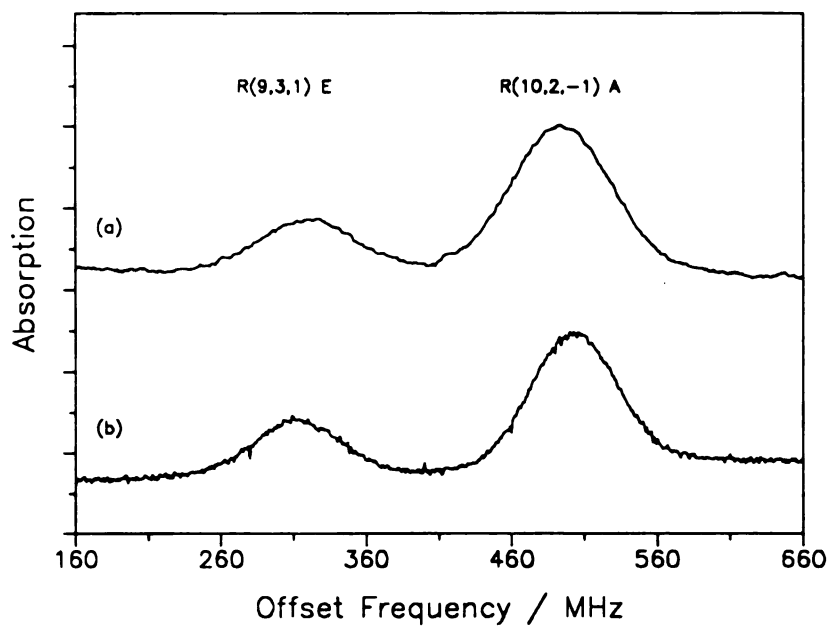


Figure 3.7. Single resonance (a) and double resonance spectra (b) of the transitions shown in Fig. 7. The spectrum in (a) is the same as that in Fig. (7a). The spectrum in (b) was recorded for 60 mTorr of $^{12}\text{CH}_3\text{F}$ while the QQ(12,1) and QQ(12,2) transitions in the ν_3 band of $^{12}\text{CH}_3\text{F}$ were simultaneously pumped.

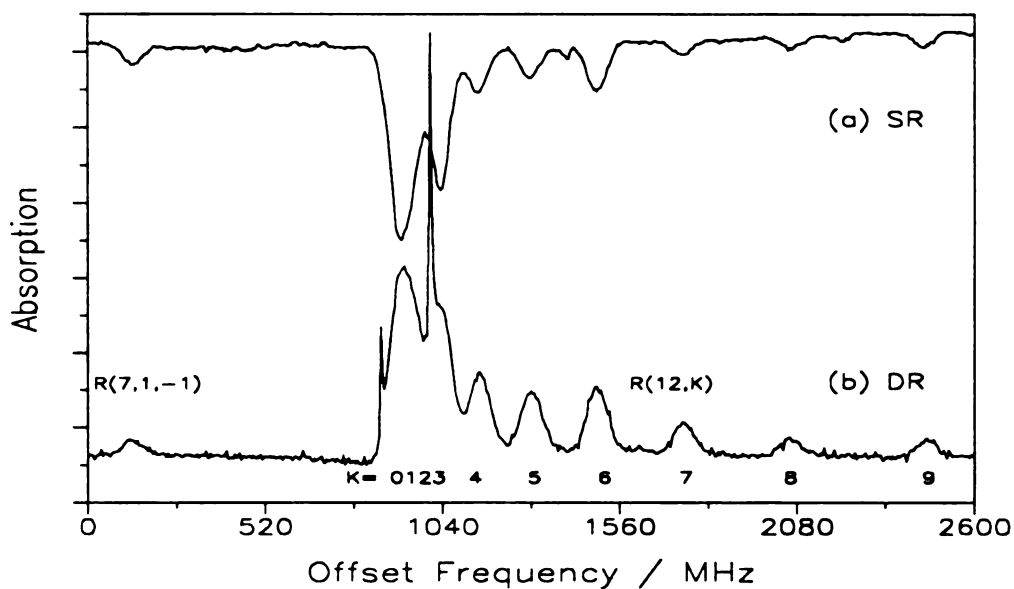
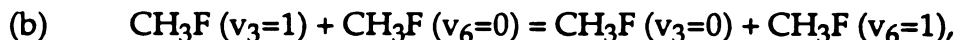
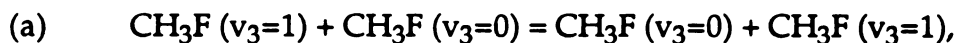


Figure 3.8. Single resonance (a) and double resonance (b) spectra of the $Q_R(7,1,-1)$ transition in the $\nu_3+\nu_6-\nu_6$ band and the $Q_R(12,K)$ transitions for $K \leq 9$ in the $2\nu_3-\nu_3$ band of $^{12}\text{CH}_3\text{F}$. The $Q_Q(12,1)$ and $Q_Q(12,2)$ transitions in the ν_3 band of $^{12}\text{CH}_3\text{F}$ were simultaneously pumped for (b). The sample pressures were 250 mTorr (a) and 60 mTorr (b). The infrared frequencies for the $Q_R(12,K)$ transitions are the horizontal axis values plus 31 556 029 MHz, whereas the infrared frequency for the $Q_R(7,1,-1)$ transition is 31 532 029 MHz minus the horizontal axis value.

the $\nu_3 + \nu_6 - \nu_6$ band to the relative intensities of the $Q_R(12,6)$ and the $Q_R(12,9)$ transitions in the $2\nu_3 - \nu_3$ band in single resonance and double resonance spectra, the relative efficiency of V-V transfer for the two processes:



can be obtained. Our results showed that the V-V transfer for process (b) is 50-60% as efficient as the V-V transfer for process (a). The difference is almost certainly the result of the larger vibrational energy for $\nu_6 = 1$ than for $\nu_3 = 1$.

D. Center frequency shift in double resonance spectra

While recording four-level double resonance effects for dilute mixtures of $^{13}\text{CH}_3\text{F}$ in the rare gases Ar and Xe, we found substantial evidence for a shift in the center frequency in the double resonance spectrum. Figure 3.9 shows a comparison of a single resonance spectrum for the $Q_R(5,3)$ transition in the ν_3 band of $^{13}\text{CH}_3\text{F}$ to the corresponding double resonance spectrum when the $Q_R(4,3)$ transition in the ν_3 band was pumped. The sample used was a mixture of 5 m Torr of $^{13}\text{CH}_3\text{F}$ in 5 Torr of Ar. A clear shift in the center frequency of the double resonance compared to the single resonance is seen. This shift was roughly proportional to the partial pressure of the foreign gas within the pressure range we examined (<10 Torr). The shift only occurs in the double resonance spectrum. The frequency shift in the single resonance spectrum is very small. An interesting point is that the shift in frequency for the several cases studied is always toward the direction that would occur if the velocity component of the pumped molecule in the direction of the pump laser changed sign during collision, as if a recoil effect is being seen. In the following section, we show from calculations of classical

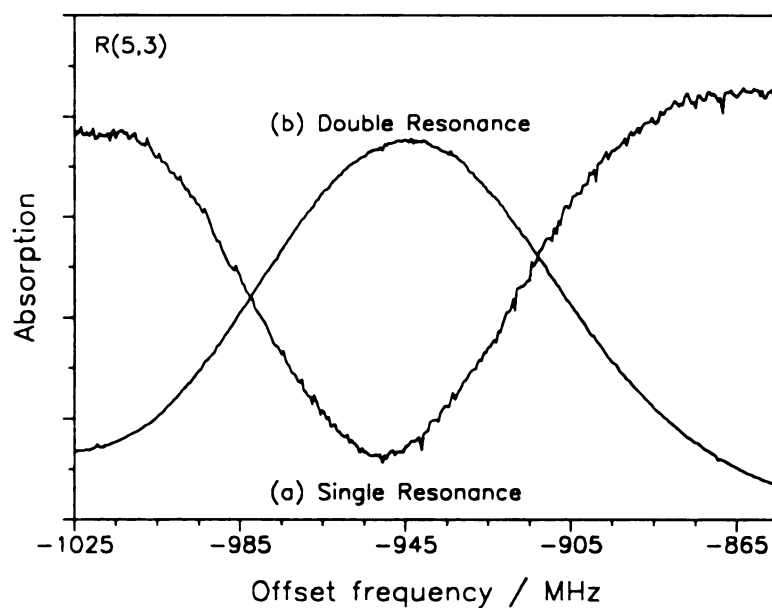


Figure 3.9. Single resonance (a) and double resonance (b) spectra of the QP(5,3) transition in the ν_3 band of $^{13}\text{CH}_3\text{F}$. The QR(4,3) transition in $^{13}\text{CH}_3\text{F}$ was pumped for the double resonance. The samples were 5 mTorr of $^{13}\text{CH}_3\text{F}$ in 5 Torr of Ar for both spectra. The infrared frequencies for each spectrum are the horizontal axis value plus 31 089 492 MHz.

collision kernels that a recoil effect is expected for under certain collisional conditions, although the pressure dependence of shift can not be explained.

V. Theoretical collision kernels

We used the procedure described in the Theory section to calculate a number of classical collision kernels. The purposes of these calculations were (i) to determine the shape of the classical collision kernels when an appropriate Lennard-Jones 6- γ function was assumed to be the intermolecular potential, so that the rationale for using the phenomenological collision kernel (the sum of the two K-S kernel) in the previous studies from this laboratory could be justified; and (ii) to ascertain whether the qualitative features of the observed line shapes for different perturbers in this study could be predicted from the classical calculation. Considering the known inadequacy of classical calculations and the uncertainty about the potential function, we did not attempt any quantitative comparison of observed and calculated results. In addition, the calculations were performed for elastic collisions, whereas the observations were for inelastic collisions. However, since the internal energy change (rotational energy) is so small compared with the kinetic energy of the molecules, it seemed reasonable to assume an elastic process for a rough initial calculation.

The procedure for our calculation can be summarized as follow:

1. Pick appropriate values of ϵ and r_e for Lennard-Jones potential.
2. Select the z-component of the velocity of the active molecule in a space-fixed coordinate system.

3. Randomly choose the impact parameter and the initial values of velocity components from appropriate Maxwell distributions.
4. Calculate the classical scattering angle in the center-of-mass coordinate system.
5. Randomly choose χ , the orientation angle of the scattering plane relative to the space-fixed frame.
6. Calculate the z-component of final velocity of the active molecule in the space-fixed frame.
7. Multiply by the normalizing factor and add to the population of an appropriate velocity box.
8. Repeat the Steps 3 to 7 many times.

One of the problems associated with the calculation was how to choose the maximum impact parameter (Step 2). In our calculation all encounters, even those with very large impact parameters, for which there is essentially no change in velocity, are considered to be "collisions". Even worse, the number of encounters per unit time within a range of impact parameter db increases with b . Thus if very large b values are allowed in the calculation, the one-dimensional collision kernel shows a strong spike within a very small range about the initial v_z value. Since the collisions we are concerned with should be hard enough to induce rotational transitions, collisions with very large impact parameter should be excluded. Our solution to this problem was to set the maximum impact parameter to a collision diameter near that calculated from the estimated linewidth parameter for an appropriate rotational transition. Unfortunately, there are not many linewidth measurements for CH_3F in foreign gases. A few values of linewidth parameters are given in Refs. (58-63) and these show that the halfwidth at halfheight for self broadening is about 15 MHz/Torr (collision diameter $\sim 15 \text{ \AA}$) for low J and

decreases with increasing J . For $\text{CH}_3\text{F}-\text{Ar}$, the width is about 3 MHz/Torr (collision diameter $\sim 5.5 \text{ \AA}$). Since this is all the information available, the best that we could do was to calculate the collision kernel for a variety of values of the maximum impact parameter and note the differences.

A. Collision kernel for dipolar-dipolar collision

One-dimensional collision kernels were calculated for $\text{CH}_3\text{F}-\text{CH}_3\text{F}$ collisions. The purpose of these calculations was to see how close the calculated kernel was to the sum of two K-S collision kernels. Figure 3.10 shows a comparison of a theoretically-calculated kernel to the sum of two K-S kernels. For the theoretically-calculated kernel, the Lennard-Jones potential function of the form of Eq. (12) with $\epsilon/k_b = 300\text{K}$ and $r_e = 3.5 \text{ \AA}$ was used. The impact parameter b was constrained within $0 < b < 10 \text{ \AA}$ and 20 000 events were counted in the calculation. The selection of the values for ϵ and r_e was on the basis of examination of the potential constants reported in Table I-A of Ref. (55). The β values for the two K-S collision kernels are 19. 1 m/s and 140. 5 m/s and the ratio of the A values $A(\text{broad})/A(\text{narrow}) = 0.185$, which are close to those obtained experimentally (36,38). As shown in Fig. 3.10, the two collision kernels have in general a similar shape. Although adjustment of the form of the potential function may bring the calculated kernel even closer to the sum of the two K-S kernels, we did not intend to do that due to the reasons mentioned above. However, the qualitative agreement between the two kernels to some extent justified the phenomenological collision kernel we have used to describe the velocity change upon collision in the previous experiments from this laboratory.

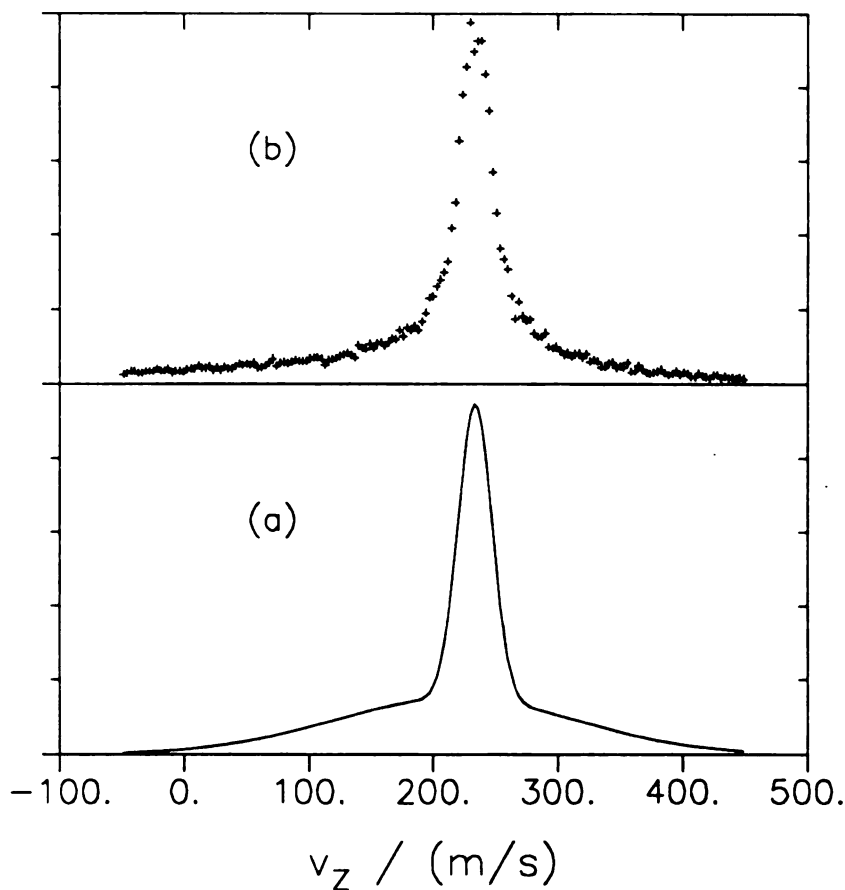


Figure 3.10. (a) One-dimensional collision kernel as a function of final velocity calculated as the sum of two Keilson-Storer functions. The β values for the two functions are 19.1 m/s and 140.5 m/s and the ratio of the A values is $A(\text{broad})/A(\text{narrow}) = 0.185$. (b) One-dimensional classical collision kernel calculated by the procedure described in the text. The parameters for the calculation are: $m = 35$ u for the active molecule and the perturber; $\epsilon/k_B = 300$ K; $r_e = 3.5$ Å; $0 \leq b \leq 10$ Å; number of collisions = 20 000. The initial velocity for both kernels was 234 m/s. The vertical axes have been scaled for convenient plotting and comparison.

B. Collision kernels for dipolar-nonpolar collision

In dipolar-nonpolar collisions, the impact parameter is supposed to be smaller than in dipolar-dipolar collisions. The well depth of the intermolecular potential (ϵ in the Lennard-Jones potential function) is also smaller for the former than for the latter. Figure 3.11 shows the effect of the mass of the perturber on the collision kernel. The parameters used in the calculations are: $\epsilon/k_b = 100\text{K}$; $r_e = 3.5$; $0 < b < 4 \text{ \AA}$; number of collisions = 40 000; m (active) = 35 u; m (perturber) = 4 u (Fig. 3.11 a); or m (perturber) = 131.3 u (Fig. 3.11b). The collision kernel in Fig. 3.11a is for the methyl fluoride - helium reduced mass and shows a substantial spike, whereas the kernel in Fig. 3.11b is for the methyl fluoride - xenon reduced mass and is much broader. This tendency agrees with the observed experimental data shown in Fig. 3.2.

The width of the spike in the calculated collision kernel increases with increased value of ϵ/k_b in the potential function and especially with decreased value of the ratio $b(\text{max}) / r_e$; the latter comparison is shown in Fig. 3.12. The parameters used in calculations are: $\epsilon/k_b = 100\text{K}$; $0 < b < 4 \text{ \AA}$; number of collisions = 40 000; m (active) = 35 u; $r_e = 4 \text{ \AA}$ (Fig. 3.12 a); $r_e = 3.5 \text{ \AA}$ (Fig. 3.12b). The four-level spectra for methyl fluoride - hydrogen show a broader spike than for methyl fluoride - helium (Figs. 3.2c and 3.2d). We therefore conclude that the intermolecular potential function for $\text{CH}_3\text{F} - \text{H}_2$ either has a well that is deeper or has a ratio of collision diameter to equilibrium distance that is smaller than the potential function for $\text{CH}_3\text{F} - \text{He}$. According to Table I-A in Ref. (55), the equilibrium distance in the potential for $\text{H}_2 - \text{H}_2$ collisions is $\sim 0.5 \text{ \AA}$, greater than the corresponding value for He-He collisions.

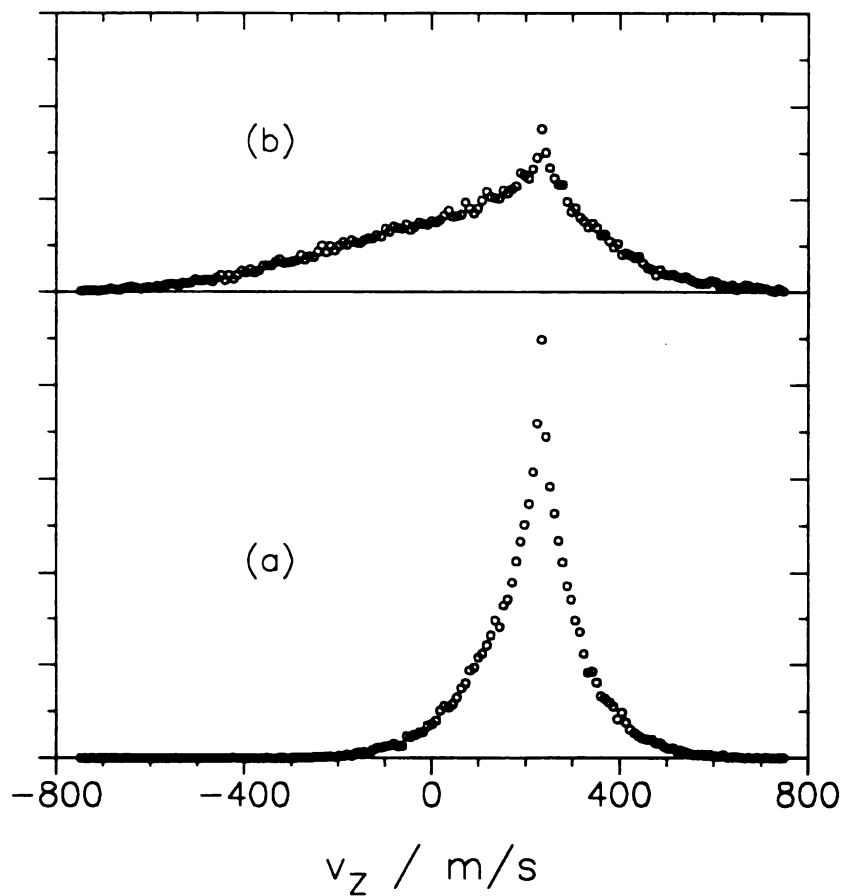


Figure 3.11. One-dimensional classical collision kernels as a function of final velocity calculated by the procedure described in the text. The parameters are: $\epsilon/k_B = 100$ K; $r_e = 4$ Å; $0 \leq b \leq 4$ Å; number of collisions = 40 000; $m(\text{active molecule}) = 35$ u; $m(\text{perturber}) = 4$ u (a) or 131.3 u (b). The initial velocity for both kernels was 234 m/s. The vertical axes have been scaled for plotting, but are relatively correct for the two plots.

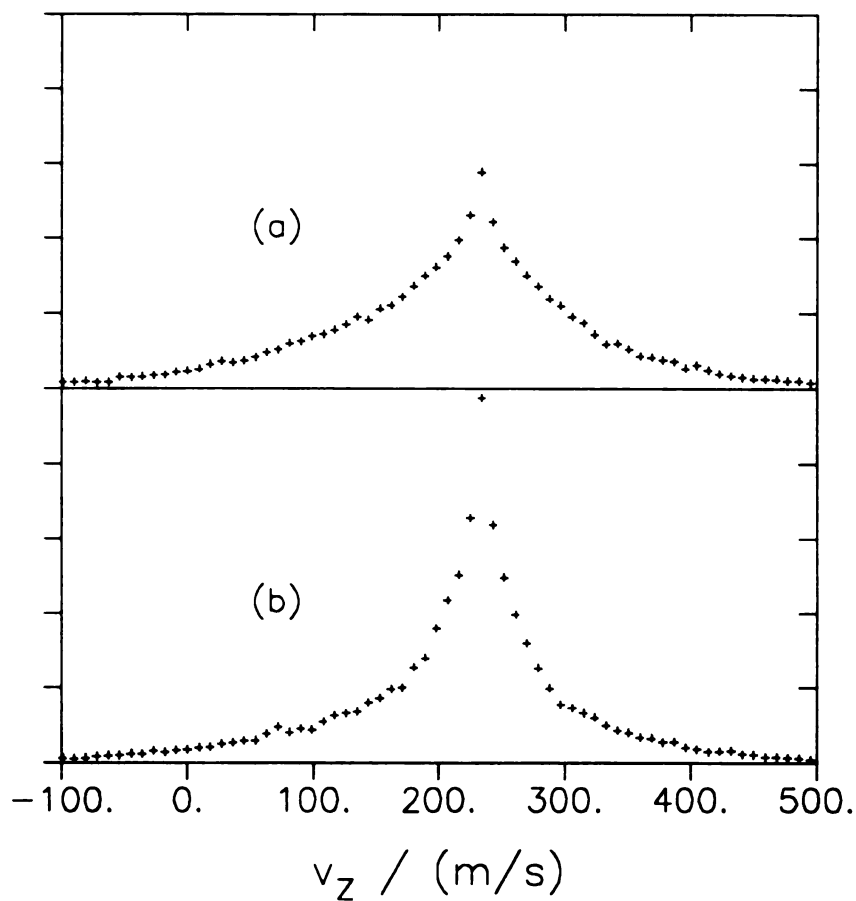


Figure 3.12. One -dimensional classical collision kernels as a function of final velocity calculated by the procedure described in the text. The parameters are: $\epsilon/k_B = 100$ K; $0 \leq b \leq 4$ Å; $m(\text{active molecule}) = 35$ u; $m(\text{perturber}) = 4$ u; number of collisions = 40 000; and $r_e = 4$ Å (a) or 3.5 Å (b). The initial velocity for both kernels was 234 m/s. The vertical axes have been scaled for plotting, but are relatively correct for the two plots.

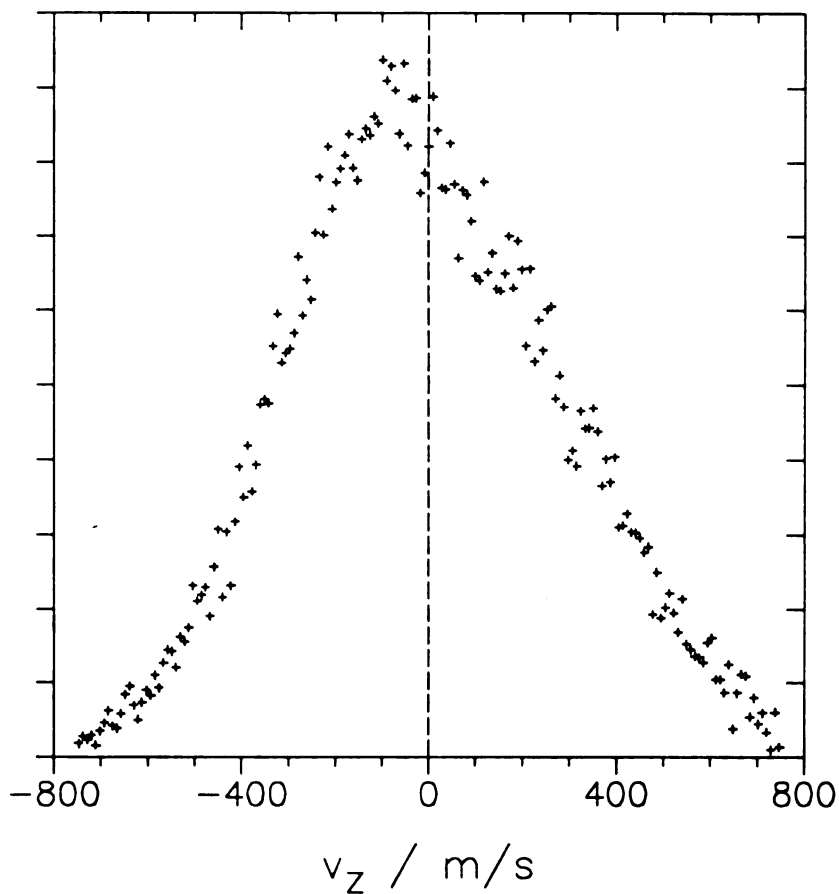


Figure 3.13. One-dimensional classical collision kernel as a function of final velocity calculated by the procedure described in the text. The parameters are: $\epsilon/k_B = 100$ K; $r_e = 4$ Å; $0 \leq b \leq 3$ Å; $m(\text{active molecule}) = 35$ u; $m(\text{perturber}) = 131.3$ u; initial velocity = 234 m/s; number of collisions = 30 000. The vertical axis has been scaled.

The collision kernels calculated for the methyl-fluoride - argon and methyl fluoride - xenon reduced mass show a significant "recoil effect" if the maximum impact parameter is limited to a small value ($< 3 \text{ \AA}^{\circ}$). This effect is especially dramatic for methyl fluoride -xenon, as shown in Fig. 3.13. We have not, however, been able to interpret the fact that the experimental data show a recoil effect that increases with increasing pressure. It appears that more sophisticated calculations are required to demonstrate this feature of these spectra.

References

1. T. Oka, J. Chem. Phys. 45, 754-755 (1966); T. Oka, J. Chem. Phys. 47, 13-26 (1967); T. Oka, J. Chem. Phys. 47, 4852- 4853 (1967); T. Oka, J. Chem. Phys. 48, 4919-4928 (1968); T. Oka, J. Chem. Phys. 49, 3135-3145 (1968).
2. T. Oka, Adv. At. Mol. Phys. 9, 127-206 (1973).
3. E. Arimondo, P. Glorieux, and T. Oka, Phys. Rev. A 17, 1375-1393 (1978); P. Glorieux, E. Arimondo, and T. Oka, J. Phys. Chem. 87, 2133-2141 (1983).
4. E. Arimondo, J. G. Baker, P. Glorieux, and T. Oka, J. Mol. Spectrosc. 82, 54-72 (1980).
5. J. C. Peterson and D. A. Ramsay, Chem. Phys. Lett. 118, 34-37 (1985).
6. S. Kano, T. Amano, and T. Shimizu, J. Chem. Phys. 64, 4711-4718 (1976).
7. N. Morita, S. Kano, Y. Ueda, and T. Shimizu, J. Chem. Phys. 66, 2226-2228 (1977).
8. N. Morita, S. Kano, and T. Shimizu, J. Chem. Phys. 69, 277-280 (1978).
9. W. A. Kreiner, A. Eyer, and H. Jones, J. Mol. Spectrosc. 52, 420-438 (1974).
10. R. M. Lees, C. Young, J. Van der Linde, and B. A. Oliver, J. Mol. Spectrosc. 75, 161-167 (1979).
11. K. Shimoda, in "Laser Spectroscopy of Atoms and Molecules" (H. Walther, ed.), pp.

- 198-252, Springer, Berlin, 1976.
12. H. Jones, in "Modern Aspects of Microwave Spectroscopy" (G. Chantry, ed.), pp. 123-216, Academic Press, New York, 1979.
 13. R. I. McCormick, F. C. De Lucia, and D. D. Skatrud, *IEEE J. Quantum Electron.* QE-23, 2060-2067 (1987).
 14. H. O. Everitt and F. C. De Lucia, *J. Chem. Phys.* 90, 3520-3527 (1989).
 15. H. O. Everitt and F. C. De Lucia, *J. Chem. Phys.* 92, 6480-6491 (1990).
 16. J. I. Steinfeld, I. Burak, D. G. Sutton, and A. V. Nowak, *J. Chem. Phys.* 52, 5421-5434 (1970).
 17. R. G. Brewer, R. L. Shoemaker, and S. Stenholm, *Phys. Rev. Lett.* 33, 63-66 (1974).
 18. R. L. Shoemaker, S. Stenholm, and R. G. Brewer, *Phys. Rev. A* 10, 2037-2050 (1974).
 19. J. W. C. Johns, A. R. W. McKellar, T. Oka, and M. Romheld, *J. Chem. Phys.* 62, 1488-1496 (1975).
 20. P. R. Berman, J. M. Levy, and R. G. Brewer, *Phys. Rev. A* 11, 1668-1688 (1975).
 21. W. K. Bischel and C. K. Rhodes, *Phys. Rev. A* 14, 176-188 (1976).
 22. C. C. Jensen, T. G. Anderson, C. Reiser, and J. I. Steinfeld, *J. Chem. Phys.* 71, 3648-3657 (1979).
 23. R. C. Sharp, E. Yablonovitch, and N. Bloembergen, *J. Chem. Phys.* 74, 5357-5365 (1981).
 24. M. Dubs, D. Harradine, E. Schweitzer, and J. I. Steinfeld, *J. Chem. Phys.* 77, 3824-3839 (1982).
 25. W. H. Weber and R. W. Terhune, *J. Chem. Phys.* 78, 6437-6446 (1983).
 26. H. K. Haugen, W. H. Pence, and S. R. Leone, *J. Chem. Phys.* 80, 1839-1852 (1984).
 27. L. Laux, B. Foy, D. Harradine, and J. I. Steinfeld, *J. Chem. Phys.* 80, 3499-3500 (1984).
 28. H. Kuze, H. Jones, M. Tsukakoshi, A. Minoh, and M. Takami, *J. Chem. Phys.* 80, 4222-4229 (1984).

29. D. Harradine, B. Foy, L. Laux, M. Dubs, and J. I. Steinfeld, *J. Chem. Phys.* 81, 4267-4280 (1984).
30. B. Foy, L. Laux, S. Kable and J. I. Steinfeld, *Chem. Phys. Lett.* 118, 464-467 (1985).
31. Y. Honguh, F. Matsushima, R. Katayama, and T. Shimizu, *J. Chem. Phys.* 83, 5052-5059 (1985).
32. K. Veeken, N. Dam, and J. Reuss, *Chem. Phys.* 100, 171-191 (1985).
33. F. Menard-Bourcin and L. Doyennette, *J. Chem. Phys.* 88, 5506-5511 (1988).
34. B. Foy, J. Hetzler, G. Millot, and J. I. Steinfeld, *J. Chem. Phys.* 88, 6838-6852 (1988).
35. Y. Matsuo, S. K. Lee, and R. H. Schwendeman, *J. Chem. Phys.* 91, 3948-3965 (1989).
36. Y. Matsuo and R. H. Schwendeman, *J. Chem. Phys.* 91, 3966-3975 (1989).
37. U. Shin and R. H. Schwendeman, *J. Chem. Phys.* 94, 7560-7561 (1991).
38. U. Shin, Q. Song, and R. H. Schwendeman, *J. Chem. Phys.* 95, 3964-3974 (1991).
39. K. M. Evenson and H. P. Broida, *J. Chem. Phys.* 44, 1637-1641 (1966).
40. J. G. Haub and B. J. Orr, *Chem. Phys. Lett.* 107, 162-167 (1984).
41. C. P. Bewick, A. B. Duval, and B. J. Orr, *J. Chem. Phys.* 82, 3470-3471 (1985).
42. J. G. Haub and B. J. Orr, *J. Chem. Phys.* 86, 3380-3409 (1987).
43. C. P. Bewick and B. J. Orr, *J. Chem. Phys.* 93, 8634-8642 (1990).
44. C. P. Bewick, J. F. Martin, and B. J. Orr, *J. Chem. Phys.* 93, 8643-8657 (1990).
45. J. Keilson and J. E. Storer, *Q. Appl. Math.* 10, 243-253 (1952).
46. H. G. Cho, Y. Matsuo, and R. H. Schwendeman, *J. Mol. Spectrosc.* 137, 215-229 (1989).
47. M. Borenstein and W. E. Lamb, *Phys. Rev. A* 5, 1311-1322 (1972).
48. J. Schmidt, P. R. Berman, and R. G. Brewer, *Phys. Rev. Lett.*, 31, 1103-1106 (1973)
49. H. Pauly in "Atom-Molecule Collision Theory" (R. B. Bernstein, ed.), pp 111-199, Plenum Press, New York, 1979.
50. S. K. Lee, R. H. Schwendeman, and G. Magerl, *J. Mol. Spectrosc.* 117, 416-433 (1986).

51. S. K. Lee, R. H. Schwendeman, R. L. Crownover, D. D. Skatrud, and F. C. De Lucia, *J. Mol. Spectrosc.* 123, 145-160 (1987).
52. F. R. Petersen, E. C. Beaty, and C. R. Pollock, *J. Mol. Spectrosc.* 102, 112-1122 (1983).
53. C. Freed, L. C. Bradley, and R. G. O'Donnell, *IEEE J. Quantum Electron.* QE-16, 1195-1206 (1980).
54. E. B. Wilson, Jr., J. C. Decius, and P. C. Cross, "Molecular Vibrations", Appendix I, Mcguire-Hill, New York, 1955.
55. J. O. Hirschfelder, C. F. Curtiss, and R. B. Bird, "Molecular Theory of Gases and Liquids", Wiley, London, 1964.
56. E. Weitz and G. W. Flynn, *J. Chem. Phys.* 58, 2679-2683 (1973).
57. E. Weitz and G. W. Flynn, *J. Chem. Phys.* 58, 2781-2793 (1973).
58. O. R Gilliam, R. D. Edwards, and W. Gordy, *Phys. Rev.* 75, 1014-1016 (1949).
59. G. Birnbaum, E. R. Cohen, and J. R. Rusk, *J. Chem. Phys.* 49, 5150-5156 (1968).
60. R. G. Brewer and R. L. Schoemaker, *Phys. Rev. Lett.* 27, 631-634 (1971).
61. H. Jetter, E. F. Pearson, C. L. Norris, J. C. McGurk, and W. H. Flygare, *J. Chem. Phys.* 59, 1796-1804 (1973).
62. P. Glorieux, J. Legrand, and B. Macke, *Chem. Phys. Lett.* 40, 287-291 (1976).
63. S. T. Sandholm and R. H. Schwendeman, *J. Chem. Phys.* 78, 3476-3482 (1983).

Chapter 4

The Effect of Initial Velocity on Rotational Energy Transfer in $^{13}\text{CH}_3\text{F}$

I. Introduction

As has been demonstrated in Chapter 3 and in the previous papers from this laboratory, pumping a near-coincident molecular transition with a very monochromatic infrared laser was able to prepare molecules in an excited state with a specific velocity component in the direction of the pump laser (1-3). This velocity component is determined by the Doppler effect and can be varied by changing the pump laser frequency (or pump laser offset). Smith *et al* have used this concept to carry out a series of measurements of velocity dependences of rates for rotational energy transfer in Na_2 and $^7\text{Li}_2$ colliding with rare gas atoms (4-6). In these experiments, the pump transitions were in the visible region and the well-developed continuously-tunable dye laser can change the pump laser frequency easily. In this study we use a similar technique in the infrared region to investigate the velocity dependence of collisionally-induced rotational transitions in $^{13}\text{CH}_3\text{F}$.

Study of the velocity dependence of a collisional process using velocity selection by Doppler shift is probably more difficult in the infrared region than in the visible region. Besides the fact that a strong and continuously tunable infrared

laser is hard to find, the absolute frequency stability of the pump laser required for the same velocity resolution is much more rigorous in the infrared region than in the visible region. This is because the Doppler shift in frequency for a molecule with a given velocity is proportional to the frequency of the transition. Thus, a change in the frequency of the radiation has a smaller effect on the velocity when the frequency is larger. Nevertheless, A. T. Mattick *et al.* investigated the velocity dependence of collisional broadening in an infrared transition in NH_3 (7). In order to study the velocity dependence of rotational energy transfer in CH_3F by infrared-infrared double resonance, we had to have a pump source that was both tunable and very monochromatic. In the previous double resonance experiments from this laboratory (1-3), a conventional CO_2 laser stabilized to a fluorescence Lamb dip of CO_2 (8) was used as the pump source. A CO_2 laser operated with this stabilization scheme emits very monochromatic radiation at the center frequency of each laser transition. Since velocity selection by Doppler shift does not require a large tunability in order to change the velocity component substantially, typically a Doppler half width of the pump transition, the tunability of a CO_2 laser line within its laser gain profile should be large enough as long as the frequency of the laser is stabilized properly. For this purpose, Weber and Terhune used a Lamb dip in a laser Stark spectrum for frequency stabilization of a CO laser (9). The advantage of this stabilization scheme, in addition to the extremely high frequency stability (at least as good as fluorescence Lamb dip stabilization), was to be able to stabilize the laser line at any frequency within the laser gain curve. For the work described here, we used the same technique to stabilize a CO_2 laser to a Stark Lamb dip of CH_3F . The technique allowed us to lock the laser to any frequency within ± 15 MHz of the center frequency of the laser transition, which provided a tunability of about 30 MHz for each CO_2 laser line.

For our experiment, the Lamb dip of a Stark spectrum in $^{13}\text{CH}_3\text{F}$ (10) was used to stabilize the 9P(32) CO_2 laser which pumps the $^{\text{Q}}\text{R}(4,3)$ transition in the ν_3 fundamental band in $^{13}\text{CH}_3\text{F}$. With this pumping, the velocity dependence of the double resonance effects was investigated for a number of probe transitions in the $2\nu_3 - \nu_3$ band. The questions we wanted to answer were whether the characteristics of the collisionally-induced rotational energy transfer (e.g. r.m.s. velocity change, relative rates) were velocity dependent, and if so, what were the dependences. One of the motivations of this experiment can be attributed to the Keilson and Storer (K-S) collision kernel (11) that we have used to obtain the root-mean-square (r.m.s.) velocity change upon collision from four-level infrared-infrared double resonance line shapes. The K-S kernel has been used in various collisional problems (1-3, 12-16). The parameter representing the r.m.s. velocity change in the kernel is now assumed to be a constant, which is equivalent to the assumption that the r.m.s. velocity change is independent of the initial velocity of the colliding molecules. Since the K-S collision kernel has been used so many times we would like to know if this assumption is true. In addition, from a practical point of view, knowledge of the velocity dependence of the parameter is essential in order to simulate the collision process (i.e., determine the final velocity distribution) with the kernel for molecules that have an initial velocity distribution instead of a single velocity. In fact, as will be seen, our experimental results show a linear dependence of the parameter on the r.m.s. relative velocity of the colliding molecules.

In order to see how the classical elastic scattering theory describes the velocity dependence of the r.m.s. velocity change during collision for a Lennard-Jones molecular potential function, we used the Monte Carlo calculation discussed in Chapter 3 to simulate collisional processes with two different initial velocities of

active molecules. Although the simulation also showed a velocity dependence of the r.m.s. velocity change during collision, the calculated variation was opposite to that observed in experiment. The disagreement between the observed and calculated results will be discussed.

II. Theoretical Part

A. Relative velocity of the colliding molecule

In our experiment, the active molecules (the molecules pumped) have a fixed velocity component in the direction of the pump laser. All of the other velocity components of both the active molecules and the perturbers are assumed to be in an equilibrium distribution. If we choose a coordinate system so that the pump beam travels in the space-fixed z direction, the velocity component in the z direction for the active molecules can be calculated from the Doppler equation (17)

$$v_z = \frac{c}{v_0} \left(v_l - v_p^0 \right), \quad (4.1)$$

where c is the speed of light, v_l is the frequency of the pump laser and v_p^0 is the center frequency of the pump transition. If only molecules with v_{az} equal to v_z given by Eq. (3.1) are pumped, then the probability of finding an excited active molecule with velocity

$$\mathbf{v}_a = v_{ax}\mathbf{i} + v_{ay}\mathbf{j} + v_{az}\mathbf{k},$$

and a perturber with velocity

$$\mathbf{v}_p = v_{px}\mathbf{i} + v_{py}\mathbf{j} + v_{pz}\mathbf{k},$$

can be expressed as $W dv_{ax} dv_{ay} dv_{az} dv_{px} dv_{py} dv_{pz}$, where

$$W = \frac{\delta(v_{az} - v_z)}{\pi^{5/2} u_a^2 u_p^3} \exp \left[-\frac{(v_{ax}^2 + v_{ay}^2)}{u_a^2} - \frac{(v_{px}^2 + v_{py}^2 + v_{pz}^2)}{u_p^2} \right]. \quad (4.2)$$

where u_a and u_p are the most probable speeds in thermal equilibrium for the active molecules and perturbers respectively. In this study, only self collisions of $^{13}\text{CH}_3\text{F}$ molecules were studied, so $u_a = u_p = \sqrt{2RT/m}$, where m is the mass of a $^{13}\text{CH}_3\text{F}$ molecule, R is the gas constant and T is the temperature. The root mean square (r.m.s.) speed of the colliding molecules can be calculated by

$$\begin{aligned} \sqrt{\langle v_r^2 \rangle} &= \sqrt{\langle (\mathbf{v}_a - \mathbf{v}_p) \cdot (\mathbf{v}_a - \mathbf{v}_p) \rangle} \\ &= \left[\int \left(v_a^2 + v_p^2 - 2\mathbf{v}_a \cdot \mathbf{v}_p \right) W dv_{ax} dv_{ay} dv_{az} dv_{px} dv_{py} dv_{pz} \right]^{1/2} \\ &= \sqrt{v_z^2 + 5RT/m}. \end{aligned} \quad (4.3)$$

Since the relative r.m.s. speed of colliding molecules is a function of v_z , which is determined by the pump laser offset, it is possible to prepare colliding molecules with different r.m.s. relative speeds by changing the pump laser frequency.

B. Velocity change upon collision

In previous studies from this laboratory, a theory has been built up to determine the r.m.s velocity change upon collision for active molecules by analyzing the lineshapes of transferred spikes observed in infrared-infrared four-level double resonance (1-3). The line shapes were analyzed by means of a function

based on the Keilson-Storer collision kernel. The final form of the line shape function is a sum of terms of the form $F\left(\left[v - v_0\right]/k\right)$ (1), where

$$F(v_z) = \frac{1}{\sqrt{\pi}\beta} \int dv'_z f(v'_z) \exp\left\{-\left[(v_z - \alpha v'_z)/\beta\right]^2\right\}, \quad (4.4)$$

in which $f(v_z)$ is the power broadened form,

$$f(v_z) = \frac{\exp\left[-(v_z/u)^2\right]}{\left(v_1 - v_p^0 - k_p v_z\right)^2 + \gamma_2^2 + \gamma_2 x_p^2 / \gamma_1}. \quad (4.5)$$

In these equations, v and v_1 are the probe and pump laser frequencies, respectively; v_0 and v_p^0 are the resonance frequency of the probe and pump transitions, respectively; x_p , γ_1 and γ_2 are the Rabi frequency for the pump, population relaxation rate, and coherence relaxation rate, respectively; $k = v_0/c$ and $k_p = v_p^0/c$, where c is the speed of light. The constants α and β in the Keilson-Storer collision kernel in Eq. (4.4) are related by expression $\alpha^2 = 1 - (\beta/u)^2$ where $0 \leq \alpha \leq 1$. The nature of Eq. (4.4) is such that if $f(v'_z)$ is a delta function at $v'_z = v_z''$, then $F(v_z)$ is a Gaussian function centered at $\alpha v_z''$ with half width at half height equal to $\beta (\ln 2)^{1/2}$. Therefore, after collision, the mean value of the component of the velocity in the z direction is $\alpha v'_z$ and the root-mean-square change in this component is $\beta / (\sqrt{2})$. In order to obtain the values of x_p , γ_1 , and γ_2 so that Eqs. (4.4) and (4.5) can be used, we recorded three-level double resonance spectra under the same experimental condition as we recorded the four-level double resonance spectra. The three-level double resonance spectra were fit to a theoretical expression derived from a semi-classical treatment, as described in Chapter 2 or in Ref. (18), and the values of x_p , γ_1 , and γ_2 which gave the best

fit were used for fitting four-level double resonance line shapes.

The line shapes of four-level double resonance spectra were fit to an expression based on Eq. (4.4) by a least squares method. It was found that a sum of three terms of the form of Eq. (4.4) represented our experimental line shapes very well. In one of these terms β_1 is the limiting value, $\beta_1 = u$, in which case, $\alpha_1 = 0$. This term is interpreted as arising from a near resonant swapping of vibrational energy between the active molecule and the perturber. In this case, the active molecule and the perturber exchange roles and since the new active molecule came from a thermal distribution, it should have a thermal distribution. The other two terms were interpreted as representing the results of collisionally-induced direct rotational transitions. The β_1 values and the amplitudes of two of the terms, the amplitude of the Gaussian component (the term with $\beta_1 = u$), and the center frequency of the probe transition were all adjusted independently by least squares in order to obtain the best fit. The input parameters for the least squares fit include the pump laser offset, the temperature and the values of γ_1 , γ_2 and x_p that were determined from the three-level double resonance line shape.

III. Experimental Details

The experimental set up used for the present study was similar to the double resonance spectrometer described in previous chapters, except that the pump laser frequency was stabilized to a saturation dip (Lamb dip) in a vibration-rotation transition in a $^{13}\text{CH}_3\text{F}$ sample in a Stark cell outside the laser cavity. Figure 4.1 shows the set up used for this stabilization scheme. In order to obtain different pump laser offsets, the center frequency of the Stark Lamb dip of $^{13}\text{CH}_3\text{F}$

was varied by changing the electric field in the Stark cell. A beam splitter was used to split the pump laser and direct a portion of the beam to the Stark cell to obtain the Stark spectrum. A mirror with 90% reflection and 10% transmission was placed at the output of the Stark cell to reflect most of the beam back through the cell to form a typical structure for a Lamb dip generation. Connected to one plate of the Stark cell was a high voltage power supply which could be operated up to 2 KV at either positive or negative voltage. The other plate was connected to a high voltage amplifier which provided a continuously variable source up to 10 KV at either polarity. To lock the laser, a strong Lamb dip signal had to be obtained first. For this purpose, a 10 kHz sine wave signal (from FG1) was superimposed on a 0.2 Hz triangular wave (from FG2) by a signal mixing box (S.M.B.) whose output was amplified 1000 times by the high voltage amplifier. The sine wave signal provided a necessary modulation to the Stark field while the triangular wave scanned the high voltage so that the Lamb dip signal could be seen on an oscilloscope. The Lamb dip signal was obtained from the transmittance through the partial reflecting mirror at the output of the Stark cell. The output of the detector was amplified by a preamplifier and then demodulated at 10 KHz by a phase sensitive detector.

When a strong Lamb dip signal was obtained, the triangular wave was turned off before the laser was locked. As mentioned above, a laser locked to a Stark Lamb dip emitted radiation at the frequency of the Stark Lamb dip. Since the frequency of the Stark spectra can be easily varied by changing the high voltage applied to the Stark cell, a laser line stabilized at this reference can be at different frequencies within the laser gain curve. In this way very stable laser with a tunability of roughly \pm the halfwidth of the laser gain curve can be obtained. By contrast, in conventional fluorescence Lamb dip stabilization, the reference signal

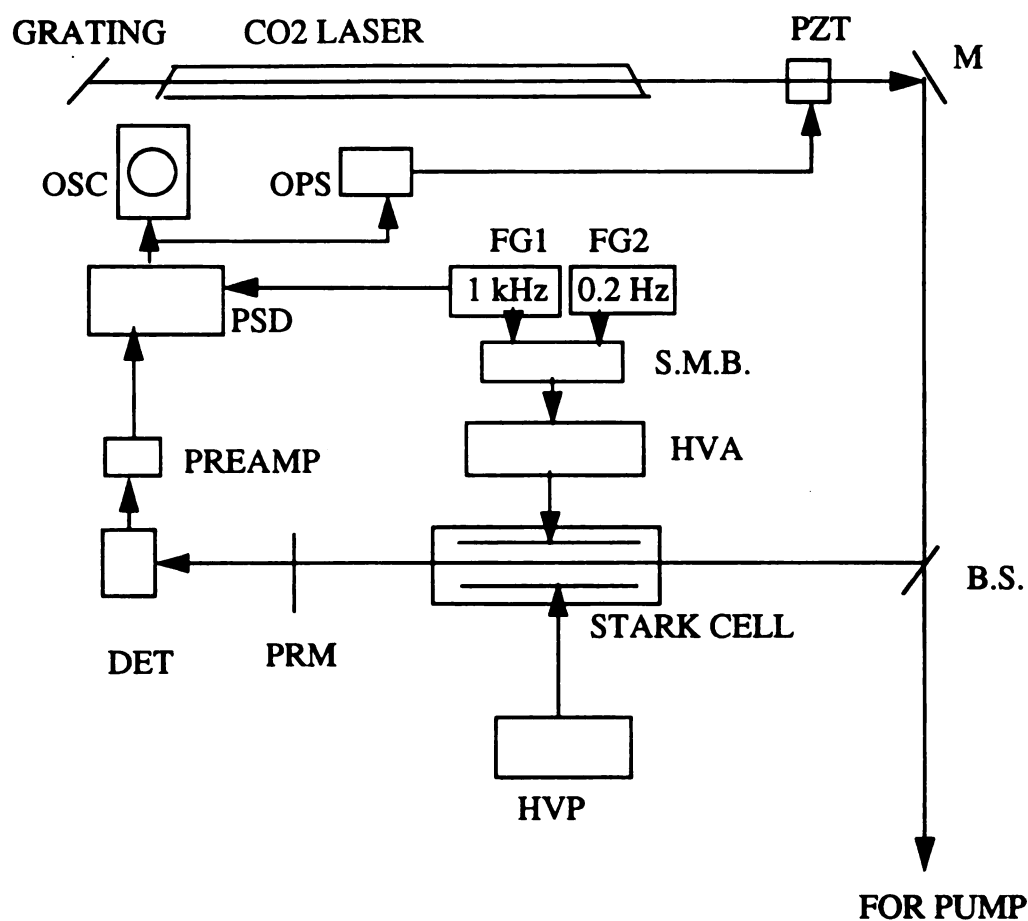


Figure 4.1. Set up for stabilization of CO₂ laser to a Stark Lamb dip. M = mirror; PZT = piezoelectric translator and laser output coupling mirror; B.S. = beam splitter; FG1, FG2 = function generators; S.M.B. = signal mixing box; HVA = high voltage amplifier; HVP = high voltage power supply; PRM = 90% partially reflecting mirror; DET = detector; PREAMP = preamplifier; OPS = operational power supply; OSC = oscilloscope.

is always at the center of the laser transition. The advantage of this frequency stabilization scheme is that the laser has a very precise frequency. As will be shown below, the frequency of the laser stabilized at a Lamb dip in a Stark spectrum can also be precisely determined from the three-level double resonance line shape, provided that precise center frequencies of the pump and probe transitions are known.

Laser gain is frequency dependent, so the pump laser power will be different when the laser emits at different positions within the gain curve. It was important to keep the pumping power constant at different pump laser offsets in this experiment, so that the line shape changes would not be the result of different pumping power. For this purpose, we carefully monitored the pump power during the whole process of the experiment. Each time the pump offset was changed, the pumping power was measured before the sample cell and kept at the same level by rotating the additional polarizer before POL2 (Fig. 1.1) to change the amplitude of the horizontal component of the pumping radiation. The pumping power was also monitored from time to time and the fluctuation at the same offset was less than 3%.

In the present study, only the $Q_R(4,3)$ transition in the ν_3 fundamental band of $^{13}\text{CH}_3\text{F}$ was pumped. The pump laser was the 9P(32) line of $^{12}\text{CO}_2$ laser which was known to be coincident with several strong Stark effect transitions in $^{13}\text{CH}_3\text{F}$ (11). By locking the laser to the Stark Lamb dip of the $Q_R(4,1)$, $m=5 \leftarrow 4$ transition in the ν_3 band of $^{13}\text{CH}_3\text{F}$, a tunability of about 30 MHz was obtained. The double resonance effects at 8.6, 23.1 and 37.8 MHz pump offsets were recorded for each of the $Q_P(6,3)$, $Q_P(7,3)$ and $Q_P(8,3)$ probe transitions in the $2\nu_3 - \nu_3$ hot band of $^{13}\text{CH}_3\text{F}$ at room temperature, ~ 297 K. The sample cell was a glass tube, 1 m long and 25 mm in diameter, with NaCl windows mounted at a slight angle to reduce

etalon effects. The frequencies for the pump and probe transitions are summarized in Table 4.1. The sample pressure, measured by a capacitance manometer, was typically 10 mTorr.

IV. Result and discussion

A. Three-level double resonance at different pump laser offsets

Three-level double resonance effects in $^{13}\text{CH}_3\text{F}$ were recorded first to check the frequency stability and the available tunability of the pump laser locked to the Stark Lamb dip. For this purpose, the $Q_R(4,3)$ transition in the ν_3 fundamental band was pumped while the $Q_P(5,3)$ transition in the $2\nu_3 - \nu_3$ hot band was probed. Figure 4.2 shows a comparison of the double resonance effects observed with three different pump laser offsets. The very well defined line shapes of these Doppler-free spectra indicate that the pump laser has extremely stable frequencies for all of the pump laser offsets. Each three-level double resonance spectrum was fit to a Lorentz function to determine the center frequency of the spike. From the frequencies of the spike and the known center frequency of the probe transition, precise (± 0.1 MHz) pump laser offsets could be determined (Chapter 5). Precise values of the pump laser offsets were necessary for analysis of the velocity dependence of the four-level double resonance line shape since the offsets determine the velocity components of the molecules pumped. Three-level double resonance spectra at different pump laser offsets were also used to determine the effective power broadening of the pump transition, $(\gamma_2/\gamma_1) x_p$. For this purpose, three or more spectra were recorded at each pump offset for the

TABLE 4.1

Pump and Probe Transitions Used for Double Resonance in $^{13}\text{CH}_3\text{F}$

Transition	Band	Frequency ^a	Offset ^b	Laser ^c
Pump Transitions				
$Q_{R(4,3)}$	ν_3	31 042 693. 8	8.6	$^{12}\text{C}^{16}\text{O}$ 9P(32)
$Q_{R(4,3)}$	ν_3	31 042 693. 8	23.1	$^{12}\text{C}^{16}\text{O}$ 9P(32)
$Q_{R(4,3)}$	ν_3	31 042 693. 8	37.8	$^{12}\text{C}^{16}\text{O}$ 9P(32)
Probe Transitions				
$Q_{P(5,3)}$	$2\nu_3 - \nu_3$	30 092 980. 5	14572.6	$^{13}\text{C}^{16}\text{O}$ 9P(16)
$Q_{P(6,3)}$	$2\nu_3 - \nu_3$	30 040 821. 2	12707.5	$^{13}\text{C}^{16}\text{O}$ 9P(18)
$Q_{P(7,3)}$	$2\nu_3 - \nu_3$	29 988 049. 4	10600.7	$^{13}\text{C}^{16}\text{O}$ 9P(20)
$Q_{P(8,3)}$	$2\nu_3 - \nu_3$	29 934 667. 0	8253.7	$^{13}\text{C}^{16}\text{O}$ 9P(22)

^aCenter frequency of the transition in MHz determined in the work described in Chapter 5.

^bThe CO_2 laser frequency minus center frequency of the transition in MHz.

^cPump lasers were stabilized to the Stark Lamb dip of the $R(4,1)$, $m=5 \leftarrow 4$, transition in the ν_3 band of $^{13}\text{CH}_3\text{F}$; the electric field applied for Stark Lamb dips for different pump laser offsets were: 7.851 kV/cm for 8.6 MHz; 8.363 kV/cm for 23.1 MHz; and 8.875 kV/cm for 37.8 MHz. Probe lasers were stabilized to the fluorescence Lamb dip of a $^{13}\text{C}^{16}\text{O}_2$ sample.

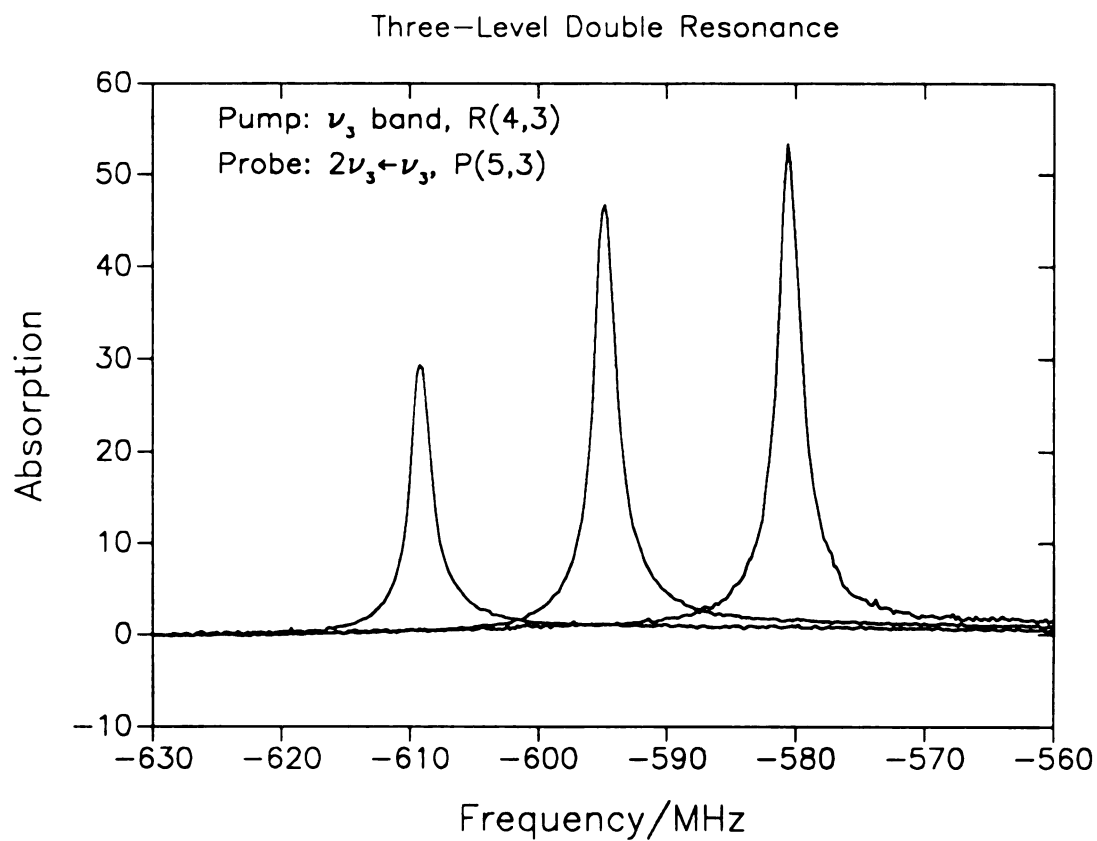


Figure 4.2. Comparison of three-level double resonance effects observed with three different pump laser offsets. The $QR(4,3)$ transition in the ν_3 hot band was pumped and the $QP(5,3)$ transition in $2\nu_3 - \nu_3$ band was probed. The lasers used are given in Table 4.1. The horizontal axis is the probe laser frequency minus 30093553.09 MHz.

same pumping power that was used to record four-level double resonance spectra, typically 1 W. The spectra were fit to the three-level double resonance line shape derived from a density matrix formalism, which was discussed in detail in Chapter 2. The values of x_p , γ_1 , and γ_2 obtained from the fit were each averaged for different spectra to get the final values that were used to analyze the four-level double resonance line shapes.

B. Initial velocity dependence of the r.m.s. velocity change upon collision

As has been shown in the previous work from this laboratory, infrared-infrared four-level double resonance line shapes can provide information about the correlation of r.m.s. velocity change and angular momentum change for active molecules as a result of collision. The line shapes obtained with different pump laser offsets allow us to study the velocity dependence of this correlation. For this purpose, we recorded the double resonance effects for each of the $Q_P(6,3)$, $Q_P(7,3)$ and $Q_P(8,3)$ probe transitions in the $2\nu_3 - \nu_3$ hot band with three different pump laser offsets, which were the same as those used in three-level double resonance, for the $Q_R(4,3)$ pump transition in the ν_3 fundamental band. Figure 4.3 shows a comparison of the spectra obtained for the $Q_R(7,3)$ probe transition. The spectra were analyzed numerically by means of the least squares fitting program described briefly in the Theoretical Section and in more detail in Ref. (3). It was found that the widths of the transferred spikes were substantially larger for a larger pump laser offset for all of the investigated probe transitions. Figure 4.4 shows a comparison of the transferred spikes in the $Q_P(6,3)$ probe transition in the

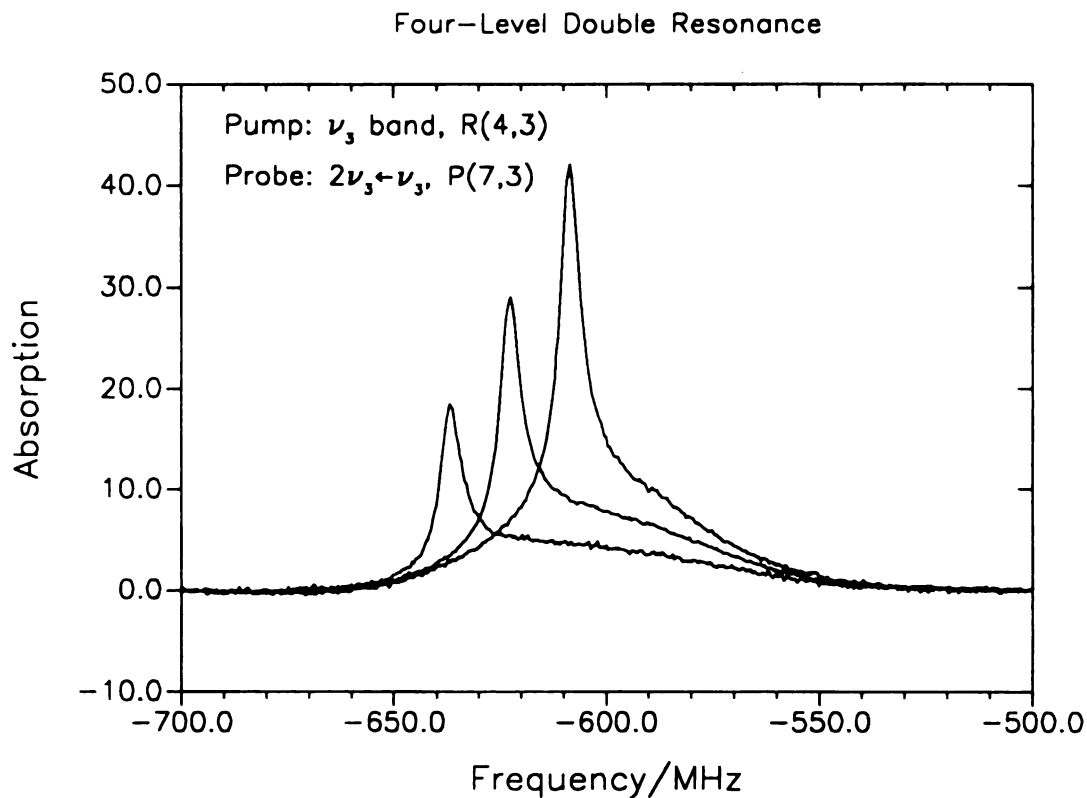


Figure 4.3. Comparison of four-level double resonance effects observed with different pump laser offsets (8.6, 23.1 and 37.8 MHz from left to right). The $Q_R(4,3)$ transition in the ν_3 band was pumped and the $Q_P(7,3)$ transition in $2\nu_3 - \nu_3$ hot band was probed. The lasers used are given in Table 4.1. The horizontal axis is the probe laser frequency minus 29988650.09 MHz.

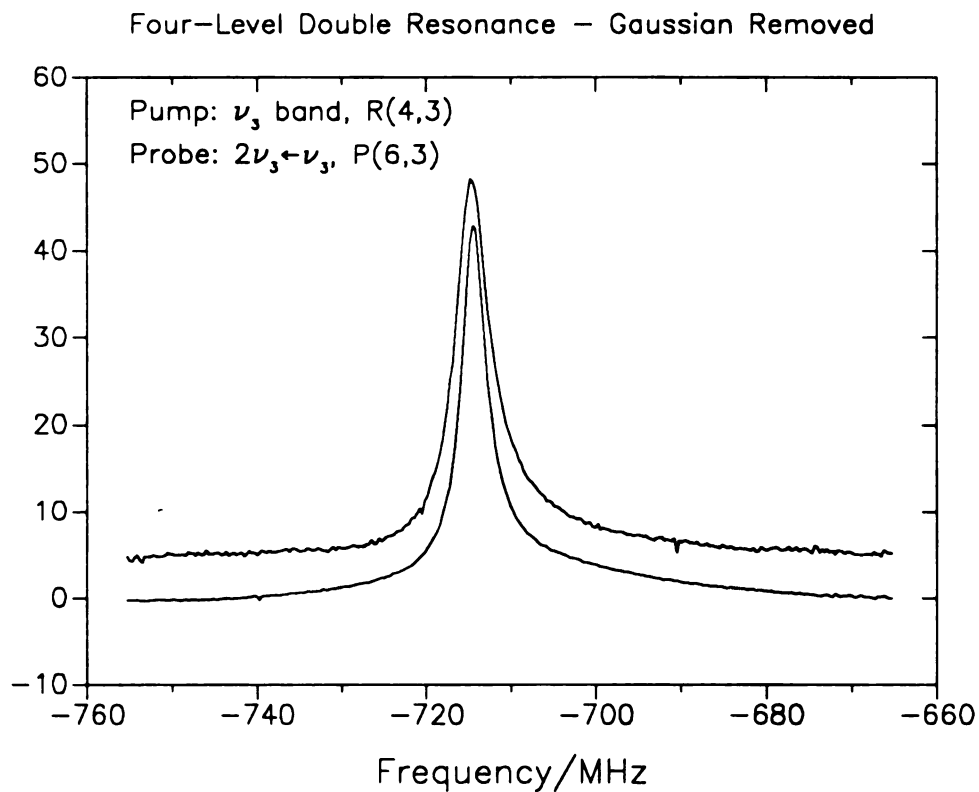


Figure 4.4. Comparison of the line shape of the transferred spike observed with pump laser offset at 37.8 MHz (upper) to that at 8.6 MHz (lower). The Gaussian part was removed. The $QR(4,3)$ transition in the ν_3 band was pumped and the $QP(7,3)$ transition in the $2\nu_3 - \nu_3$ hot band was probed. The lasers used are given in Table 4.1. The upper spectrum has been shifted in frequency and scaled for comparison. The horizontal axis is the probe laser frequency minus 30041528.73 MHz.

$2\nu_3 - \nu_3$ band while the $Q_R(4,3)$ transition in the ν_3 band was pumped at two different pump laser offsets 8.6 and 37.8 MHz (the spectra have been shifted in frequency for comparison). The upper spectrum was at the larger offset. The intensities of the spectra were normalized for comparison. It is clear that the upper spectrum is wider than the lower one.

Table 4.2 summarizes the results obtained from the fittings for the three probed transitions at three different pump laser offsets. The two β parameters in the table were the parameters of the two K-S collision kernels that were obtained from the two spike components in the four-level double resonance line shape. Although both of the spike components are interpreted to be the results of direct rotational energy transfer, they are believed to have different origins. The narrower spike component results from molecules that have undergone one or a small number of collisions with a large impact parameter where the intramolecular interaction was weak and the velocity change was small. The broader spike component results from molecules that have undergone either one collision with a small impact parameter, where the intramolecular interaction was strong and the molecular path was deflected with a large angle, or a very large number of collisions with large impact parameters, where the large velocity change was the result of many small changes in velocity during each collision. It is interesting to note in Table 4.2 that the value of $\Delta v_{\text{rms}} = \beta / (\sqrt{2})$, the r.m.s. velocity change upon collision, depends on the pump laser offset for both components of the transferred spike for all of the probe transitions examined. The tendency is that the larger the pump laser offset, the larger the r.m.s. velocity change.

In the collisional process concerned in this study, the velocity of one molecule of a colliding pair in space fixed coordinates does not determine the nature of

TABLE 4.2

Transferred spikes for different pumping offsets in $^{13}\text{CH}_3\text{F}^{\text{a}}$

Probe ^b	Pump offset	$k\beta_1$ ^c	$(\Delta v_{\text{rms}})_1$ ^d	$k\beta_2$ ^e	$(\Delta v_{\text{rms}})_2$ ^f
Q _P (6,3)	8.6	1.22	8.61	7.15	50.5
	23.1	1.35	9.53	8.86	62.5
	37.8	1.52	10.73	10.93	77.1
Q _P (7,3)	8.6	1.82	12.87	10.44	73.8
	23.1	1.99	14.07	12.20	86.2
	37.8	2.21	15.62	15.98	113.0
Q _P (8,3)	8.6	2.45	17.35	14.00	99.1
	23.1	2.65	18.77	16.74	118.5
	37.8	2.99	21.17	18.95	134.2

^aPump transition is Q_R(4,3) in the ν_3 fundamental band.^bProbe transitions are in the $2\nu_3 - \nu_3$ hot band.^cKeilson-Storer β parameter in frequency units (MHz) for the narrow spike. k is the magnitude of the wave vector for the probe transition.^dRoot mean square change in speed for active molecules that contribute to the narrow spike.^eKeilson-Storer β parameter in frequency units (MHz) for the broad spike. k is the magnitude of the wave vector for the probe transition.^fRoot mean square change in speed for active molecules that contribute to the broad spike.

collision. What really matters is the relative velocity of the colliding partners. To understand the essence of the observed phenomena, we calculated the relative r.m.s. velocity of molecules pumped with different pump laser offsets. The dependences of r.m.s. velocity change upon collision on the initial relative r.m.s. velocity of molecules before collision are summarized in Table 4.3. It is obvious that the r.m.s. velocity change is roughly proportional to the initial relative r.m.s. velocity of the active molecules for the same collisionally-induced transition. The proportionality coefficients get larger when the change of the J quantum number gets larger during the collisionally-induced rotational energy transfer.

C. Velocity dependence of rates of energy transfer

While the line width of a spike component in the four-level double resonance line shape contains information on r.m.s. velocity change of the active molecule during rotational energy transfer, the relative intensity of the component reflects the relative rate of the energy transfer process. Comparison of relative intensities of spikes obtained at different pump laser offsets allows us to examine the velocity dependence of the rates for the energy transfer. In previous work from this laboratory (3), theoretical relations necessary for comparative intensity measurements for four-level double resonance line shapes have been worked out. These theoretical considerations have been built into the least-squares fitting program, which allowed us to obtain scaled intensities for different components in the observed line shapes. The results are summarized in Table 4.4.

With the same initial relative r.m.s velocity, the ratio of the area of the narrow component to the broad component of the transferred spikes decreases as ΔJ

TABLE 4.3

Velocity change during state change upon collision in $^{13}\text{CH}_3\text{F}$

State change ^a	v_z^b	v_r^c	$(\Delta v_{\text{rms}})_1^d$	r_1^e	$(\Delta v_{\text{rms}})_2^d$	r_2^e
(5, 3) \rightarrow (6, 3)	83.1	599.5	8.61	0.014	50.46	0.08
	223.1	634.3	9.53	0.015	62.52	0.10
	365.1	697.0	10.73	0.015	77.13	0.11
(5, 3) \rightarrow (7, 3)	83.1	599.5	12.87	0.021	73.83	0.12
	223.1	634.3	14.07	0.022	86.24	0.14
	365.1	697.0	15.62	0.022	112.96	0.16
(5, 3) \rightarrow (8, 3)	83.1	599.5	17.35	0.029	99.14	0.17
	223.1	634.3	18.77	0.030	1118.55	0.19
	365.1	697.0	21.17	0.030	134.20	0.19

^aRotational state change from (J,K) to (J',K') upon collision in the $v_3=2$ vibrational state.^bThe z-component of the initial velocity of active molecule before collision.^cInitial root mean square relative speed of the colliding molecules $(v_z^2 + 5u^2/2)^{1/2}$,
 $u=(2RT/M)^{1/2}=375.5$ m/s.^dThe same as in Table 4.2^e $r_i=(\Delta v_{\text{rms}})_i / v_r$ (i=1,2)

TABLE 4.4

Relative intensities for collisionally-induced transitions in $^{13}\text{CH}_3\text{F}$

State change ^a	v_r ^b	A_1/A_2 ^c	A_1/A_G ^d	A_2/A_G ^e	R_1 ^f	R_2 ^g
(5, 3) \rightarrow (6, 3)	599.5	1.98	0.59	0.30	1.00	1.00
	697.0	1.94	0.60	0.33	1.06	1.15
(5, 3) \rightarrow (7, 3)	599.5	1.21	0.26	0.21	1.00	1.00
	697.0	1.18	0.38	0.34	1.23	1.32
(5, 3) \rightarrow (8, 3)	599.5	0.88	0.23	0.25	1.00	1.00
	697.0	0.81	0.33	0.53	1.32	1.86

^aRotational state change from (J,K) to (J',K') upon collision in the $v_3=1$ vibrational state.^bInitial root mean square relative velocity (m/s) of colliding molecules $(v_z^2 + 5u^2/2)^{1/2}$, $u=(2RT/M)^{1/2}=375.5$ m/s.^cThe ratio of intensity for the narrow spike to that for the broad spike.^dThe relative intensity of the narrow spike to the Gaussian in the observed spectrum.^eThe relative intensity of the broad spike to the Gaussian in the observed spectrum^fThe ratio of the intensity of the narrow spike to that at $v_r=599.5$ m/s.^gThe ratio of the intensity of the broad spike to that at $v_r=599.5$ m/s.

increases. If the broad component is interpreted as resulting from collisions with small impact parameter, this is an indication that a greater proportion of hard collisions is required for rotational energy transfer with larger ΔJ . For the same ΔJ , the ratio decreases slightly as the initial relative r.m.s. velocity increases. This indicates that a collision with a larger relative velocity is harder than that with a smaller velocity.

For the same initial relative r.m.s velocity, the ratios of the areas of both the narrow and the broad components of the transferred spikes to the Gaussian component decrease as ΔJ increases while for the same ΔJ , the ratios increase as the relative r.m.s. velocity increases. This indicates that the time required for rotational energy transfer increases as ΔJ increases and that for a larger initial relative velocity a shorter time is required for a rotational energy transfer.

Finally, for the same ΔJ , the intensity of either the narrow or the broad component of the spike is larger at larger relative r.m.s. velocity than that at smaller relative r.m.s. velocity. The difference is greater as ΔJ increases. The former is understandable since the larger the relative velocity of the colliding molecules, the larger the collisional rate. The latter indicates again that a collision with a larger relative velocity is harder so that it favors a collisionally-induced transition with a large ΔJ .

D. Calculation from classical scattering theory

In Chapter 2, we described an application of classical elastic scattering theory and a Monte Carlo calculation to simulate the collisional processes concerned in our experiment. In that chapter, most of the features observed in the experiments

agreed qualitatively with calculations. We had expected that the calculation would be able to predict the qualitative feature of dependence of r.m.s. velocity change on initial relative velocity discussed in this chapter. However, the results of the calculation indicate that the r.m.s. velocity change should decrease as the relative r.m.s. initial velocity of the colliding molecules increases, which is just opposite to the results from experiment. This contradiction may not be surprising considering the crudeness of the model we used in our simulation. For the simulation, the collision process was assumed to be classical and elastic, and the result is understandable upon realization that the larger the relative velocity, the less time the molecules interact during collision, which leads to a smaller deflection and therefore a smaller change in the z component of the velocity. By contrast, the collisional process we studied in our experiment was neither classical nor elastic. In order for a collision to induce a state-to-state transition, the collision must be hard enough. For larger relative velocity for a colliding pair, the smaller interaction time can be compensated by a larger interaction potential, i.e., a smaller impact parameter, which may cause a larger deflection angle during collision. In order to interpret our experimental result correctly, it appears that a full quantum mechanical treatment of the rotationally inelastic collision process may be required. Although a quantum mechanical calculation for an inelastic scattering process is typically very complicated and time consuming, our experimental results provide considerable data for comparison, which may lead to additional understanding of the fundamental nature of intramolecular collisional interaction.

References

1. Y. Matsuo, S. K. Lee, and R. H. Schwendeman, *J. Chem. Phys.* 91, 3948-3965 (1989).
2. Y. Matsuo and R. H. Schwendeman, *J. Chem. Phys.* 91, 3966-3975 (1989).
3. U. Shin, Q. Song, and R. H. Schwendeman, *J. Chem. Phys.* 95, 3964-3974 (1991).
4. N. Smith, T. A. Brunner, R. D. Driver, and D. E. Pritchard, *J. Chem. Phys.* 69, 1498-1503 (1978).
5. N. Smith, T. A. Brunner, and D. E. Pritchard, *J. Chem. Phys.* 74, 467-482 (1982).
6. N. Smith, T. P. Scott, D. E. Pritchard, *J. Chem. Phys.* 81, 1229-1247 (1978).
7. A. T. Mattick, A. Sanchez, N. A. Kurnit, and A. Javan, *Appl. Phys. Lett.* Vol. 23 (12), 675-678 (1973).
8. C. Freed and A. Javan, *Appl. Phys. Lett.* 17, 53-56 (1970).
9. W. H. Weber and R. W. Terhune, *Opt. Lett.* 6, 455-457 (1981).
10. S. M. Freund, G. Duxbury, M. Romheld, J. T. Tiedje, and T. Oka, *J. Mol. Spectrosc.* 52, 38-57 (1974).
11. J. Keilson and J. E. Storer, *Q. Appl. Math.* 10, 243-253 (1952).
12. M. Borenstein and W. E. Lamb, *Phys. Rev. A* 5, 1311-1322 (1972).
13. J. Schmidt, P. R. Berman, and R. G. Brewer, *Phys. Rev. Lett.*, 31, 1103-1106 (1973).
14. C. Brechignac, R. Vetter, and P. R. Berman, *Phys. Rev. A* 17, 1609 (1978).
15. C. G. Aminoff, J. Javanainen, and M. Kaivola, *Phys. Rev. A* 28, 722 (1983).
16. J. E. M. Haverkort, J. P. Woerdman, and P. R. Berman, *Phys. Rev. A* 36, 5251-5264 (1987).
17. W. Demtroder, *Laser Spectroscopy*, edited by F. P. Schafer (Springer Series in Chemical Physics 5, 1982), pp. 86.
18. Q. Song and R. H. Schwendeman, *J. Mol. Spectrosc.* 149, 356-374 (1991).

Chapter 5

Study of the $3\nu_3 - 2\nu_3$ Band in $^{12}\text{CH}_3\text{F}$ and Doppler-Free Frequencies in $^{12}\text{CH}_3\text{F}$ and $^{13}\text{CH}_3\text{F}$

I. Introduction

Methyl fluoride has been considered as an ideal compound for a number of spectroscopic applications with lasers. In addition to its stability and strong absorption near the 10 μm region the molecule has many near coincidences of vibration-rotation transitions with CO_2 laser lines (1,2). Because of this, various experiments have been carried out in methyl fluoride with CO_2 lasers as excitation sources. Examples include studies of rotational and vibrational energy transfer (3-5), relaxation processes in the optically-pumped far-infrared laser (6-8), observation of dynamic Stark splitting (9), measurement of light-induced drift (10,11), and studies of the correlation of change in velocity with collisionally-induced rotational energy transfer (12-14). These applications stimulated a considerable number of spectroscopic investigations for this molecule.

Vibration-rotation transitions of $^{12}\text{CH}_3\text{F}$ in the 10 μm region have been studied extensively several times. High resolution spectra (Doppler limited) for the ν_3 fundamental, the $2\nu_3 - \nu_3$ hot band and the $\nu_3 + \nu_6 - \nu_6$ hot band have been measured with the infrared sideband laser system in this laboratory (2,15), and with FTIR spectrometers by D. Papousek et al (16). The molecular constants for the relevant vibrational levels have been determined to an accuracy that allows a

frequency of a rovibrational transition to be calculated within several MHz. However, in spite of these spectroscopic studies, there has been no report of frequencies of transitions in the $3\nu_3 - 2\nu_3$ hot band. In addition, only a few transitions in CH_3F have been measured with Doppler-free resolution (9,17-19). The major purposes of this study were to investigate rovibrational transitions in the $3\nu_3 - 2\nu_3$ band of $^{12}\text{CH}_3\text{F}$ and to carry out precise frequency measurements for some important transitions in the ν_3 fundamental and the $2\nu_3 - \nu_3$ hot band of CH_3F .

The rovibrational transitions in the $3\nu_3 - 2\nu_3$ hot band of methyl fluoride are expected to be difficult to observe with conventional single modulation spectroscopy. Since the $\nu_3=2$ vibrational state is about 2000 cm^{-1} above the ground vibrational state, the population in thermal equilibrium at room temperature is extremely small ($N_{2\nu_3}/N_0 \sim 6 \times 10^{-5}$) which leads to very weak absorptions for transitions in this hot band. Besides, there are several unassigned weak hot bands in the region that have larger intensities than the $2\nu_3 - \nu_3$ band which makes it even harder to assign the spectrum even if transitions can be observed. High resolution infrared spectroscopy of methyl fluoride showed many near coincidences of the vibration rotation transitions in the $2\nu_3 - \nu_3$ hot band with CO_2 lasers (2). These near coincidences can be employed to pump molecules from the $\nu_3=1$ to the $\nu_3=2$ vibrational state with strong CO_2 laser radiation. By searching for transitions in the $3\nu_3 - 2\nu_3$ band while a transition in the $2\nu_3 - \nu_3$ band is pumped - i.e., by using infrared-infrared double resonance - the chances of observing transitions in this band increase dramatically. First, the intensities of transitions in the $3\nu_3 - 2\nu_3$ band will increase as a result of the pumping effect on the population. Second, which may be more important, our knowledge of double resonance lineshapes in this molecule (12,13) can help us to make a correct assignment for the transitions in the $3\nu_3 - 2\nu_3$ band. In the present study, the transitions in the $3\nu_3 - 2\nu_3$ band were searched with a probe laser while either the

$Q_R(7,3)$ or the $Q_R(13,6)$ transition in the $2\nu_3 - \nu_3$ band was pumped. Six transitions in the $3\nu_3 - 2\nu_3$ band of $^{12}\text{CH}_3\text{F}$ were observed and assigned. The frequencies obtained have been fit to equations for the rotational levels in the $\nu_3=3$ vibrational state by the least squares method and molecular constants for this vibrational state have been obtained.

The Doppler-free feature of the spikes in infrared-infrared double resonance spectra can be used to determine the precise center frequencies of both pump and probe transitions. Knowledge of precise center frequencies of the pump transitions is found to be desirable in this laboratory for the study of the r.m.s. velocity change during collisionally-induced rotational energy transfer (Chapter 4). Recently, we found that Doppler free frequencies for the pump and probe transitions could be obtained from three-level or four-level double resonance spectra recorded separately with copropagating and counter-propagating configurations for the pump and probe beams. In this work, we used the technique to obtain Doppler-free frequencies for several important transitions in both $^{12}\text{CH}_3\text{F}$ and $^{13}\text{CH}_3\text{F}$. Some of these frequencies have been used to deduce the precise pump laser offsets in Chapter 4.

We also carried out infrared-infrared four-level double resonance within the $2\nu_3 - \nu_3$ hot band. As will be discussed below, the four-level double resonance effect in the $3\nu_3 - 2\nu_3$ band observed by pumping a $2\nu_3 - \nu_3$ transition shows only the direct rotational energy transfer, while that in the $2\nu_3 - \nu_3$ band with the same pumping shows the direct rotational energy transfer and near vibration-vibration transfer in opposite phases. The information about the relative rates of these two energy transfer processes obtained from the experimental line shapes will be discussed.

II. Theoretical background

A. Energy levels in a non-degenerate vibrational mode in $^{12}\text{CH}_3\text{F}$

The ν_3 vibration in $^{12}\text{CH}_3\text{F}$ is a non-degenerate vibration rotation mode whose energy levels can be calculated by means of the equations (20),

$$\begin{aligned}
 E(v, J, K) = & E_v + B_v J(J+1) + (A_v - B_v) K^2 - D_J^{(v)} J^2 (J+1)^2 \\
 & - D_{JK}^{(v)} J(J+1) K^2 - D_K^{(v)} K^4 + H_J^{(v)} J^3 (J+1)^3 + H_{JK}^{(v)} J^2 (J+1)^2 K^2 \\
 & + H_{KJ}^{(v)} J(J+1) K^4 + H_K^{(v)} K^6 + L_J^{(v)} J^4 (J+1)^4 + L_{JJK}^{(v)} J^3 (J+1)^3 K^2 \\
 & + L_{JJK}^{(v)} J^2 (J+1)^2 K^4 + L_{JKKK}^{(v)} J(J+1) K^6 + L_K^{(v)} K^8.
 \end{aligned} \tag{5.1}$$

Here v and J are the vibrational and rotational quantum numbers; K is the quantum number for the projection of angular momentum on the molecular axis; E_v is the vibrational energy; A_v and B_v are rotational constants; and the remaining parameters are centrifugal distortion constants. The selection rules for the vibration rotation transitions are $\Delta v = 1$; $\Delta K = 0$; and $\Delta J = 0, \pm 1$ which corresponds to three different branches: P ($\Delta J = -1$), Q ($\Delta J = 0$) and R ($\Delta J = 1$) branches. The frequency of a transition can be expressed by

$$\nu = \frac{E'(v', J', K') - E''(v'', J'', K'')}{h}. \tag{5.2}$$

Typically, frequencies of a large number of transitions in a vibrational band are measured and fit to Eqs. (5.1) and (5.2) in order to determine the molecular constants for the upper and the lower vibrational levels of the band. Once the

molecular constants are known, the frequency for any rovibrational transition in the band can be predicted by Eqs. (5.1) and (5.2).

Eq. (5.1) is valid for a non-degenerate vibration rotation mode in a symmetric top molecule for the case for which Coriolis and Fermi coupling effects are small enough to be included in the rotational and centrifugal distortion constants. The ν_3 vibrational mode in CH_3F is such a case (21). The absence of significant differences between observed and calculated frequencies has shown that this is the case for the $2\nu_3 - \nu_3$ band and, apparently, from the present work, for the $3\nu_3 - 2\nu_3$ band.

B. Precise measurement of pump laser offset frequency

The Doppler-free features of the spikes in infrared-infrared double resonance spectra recorded at both copropagating and counter propagating geometries for the pump and probe beams can be used to determine the precise center frequencies of the pump and probe transitions. Because of the Doppler effect, a moving molecule absorbs radiation whose laboratory frequency is

$$\nu = \nu_0 \left(1 + \frac{v_z}{c} \right), \quad (5.3)$$

where ν_0 is the center frequency of a transition, v_z is the velocity component of the molecule in the direction of radiation and c is the speed of light (22). The values of v_z for the sample molecules can be positive or negative depending on whether the molecule moves along the wave propagation, or against the wave propagation. For the pump transition, the frequency of absorption is the frequency of the pump laser ν_1 and the fixed velocity component of the molecules that are pumped is determined by Eq. (5.3). This velocity component has the same absolute value, but

different signs, for copropagating and counterpropagating probe laser beams, so that the pumped molecules absorb radiation at different frequencies of the probe laser in the two geometries. The frequencies can be expressed by

$$\nu_{\pm} = \nu'_0 \left(1 \pm \frac{v_z}{c} \right), \quad (5.4)$$

where ν_+ and ν_- are the probe laser frequencies of absorption by the pumped molecules (frequencies of the spikes) in the copropagating and counterpropagating configurations, respectively, and ν'_0 is the center frequency of the probe transition. If ν_+ and ν_- can be obtained from experiment, then the center frequency of the probe transition is

$$\nu'_0 = \frac{\nu_+ + \nu_-}{2}; \quad (5.5)$$

and the velocity component of the pumped molecules in the direction of the pump laser is

$$v_z = \frac{(\nu_+ - \nu_-)c}{2\nu'_0}. \quad (5.6)$$

The pump laser offset can be calculated by means of

$$\nu_0 - \nu_1 = -\frac{v_z \nu_0}{c}, \quad (5.7)$$

where the ν_1 is the frequency of the pump laser; and ν_0 is the center frequency of the pump transition. As can be seen from Eq. (5.7), if the frequency of the pump laser has been calibrated very precisely, as in the case of fluorescence Lamb dip stabilization (23), the precise center frequency of the pump transition can be

obtained (the value of ν_0 obtained from Doppler limited spectroscopy can be used on the right side of Eq. (5.7) since $\nu_z/c \ll 1$). When the pump laser frequency is not known precisely, as in the case of Stark Lamb dip stabilization (Chapter 4), precise center frequencies of the pump and probe transitions are required in order to determine the precise pump laser offset, or the velocity component of the pumped molecules in the direction of the pump radiation.

The center frequencies of the spikes are obtained by least-squares fitting the line shape of each spike to a Lorentz function. Since the line widths of the spikes (~ 1 MHz) are much narrower than the line widths of the Doppler limited spectra (~ 32 MHz), the transition frequencies determined in this way are much more accurate than the ones obtained from Doppler-limited spectroscopy, especially for transitions that are seriously overlapped in the Doppler limit.

III. Experimental detail

The double resonance spectrometer used for observation of transitions in the $3\nu_3 - 2\nu_3$ hot band is exactly the same as that used for the studies described in Chapter 2. Our strategy was to search double resonance effects in the $3\nu_3 - 2\nu_3$ hot band of $^{12}\text{CH}_3\text{F}$ while a near coincident rovibrational transition in the $2\nu_3 - \nu_3$ band was pumped by a CO_2 laser. Two near coincident transitions in the $2\nu_3 - \nu_3$ band were used as pumps for this purpose: the $Q_R(13,6)$ pump with the $9P(38)$ $^{12}\text{C}^{18}\text{O}_2$ laser and the $Q_R(7,3)$ pump with the $9P(33)$ $^{12}\text{C}^{16}\text{O}^{18}\text{O}$ laser. The frequencies for the two pump transitions and the laser offsets are listed in Table 5.1. Since our probe laser, the infrared sideband system, has only a small tunable range for each CO_2 laser line, the full coverage of the tunability in the region has to rely on a large number of laser lines of different isotopic CO_2 lasers. High resolution frequency measurements with this system are therefore most efficient

TABLE 5.1

Pump and Probe Transitions in the $2\nu_3 - \nu_3$ band of $^{12}\text{CH}_3\text{F}$

Transition	Frequency ^a	Offset ^b	Laser ^c	
Pump Transitions				
^Q R(7,3)	31341428.9	5.7	¹² C ¹⁶ O ¹⁸ O	9P(33)
^Q R(13,6)	31598591.2	35.1	¹² C ¹⁸ O ₂	9P(38)
Probe Transitions				
^Q Q(9,3)	30932581.7	9666.3	¹² C ¹⁶ O ₂	9P(36)
^Q Q(9,4)	30932871.3	9901.9	¹² C ¹⁶ O ₂	9P(36)
^Q Q(9,5)	30933130.2	10214.7	¹² C ¹⁶ O ₂	9P(36)
^Q Q(9,5)	30933130.2	10612.7	¹² C ¹⁶ O ₂	9P(36)

^aCenter frequency of the transition in MHz.

^bCenter frequency of the transition minus the CO_2 laser frequency in MHz.

^cLaser frequencies calculated from the constants in References (24) and (25).

when the spectrum has been studied previously at low resolution, or when the major molecular constants for the states involved in the transitions have been approximately determined, so that we know which CO₂ laser line to use for the sideband system. For the $3\nu_3 - 2\nu_3$ hot band of $^{12}\text{CH}_3\text{F}$, no previous study was found. In order to estimate frequencies for the transitions in the $3\nu_3 - 2\nu_3$ hot band of $^{12}\text{CH}_3\text{F}$, we calculated the molecular constants E_v , B_v , $A_v - B_v$, $D_J^{(v)}$, $D_{JK}^{(v)}$, and ΔD_K for the $\nu_3=3$ vibrational state of $^{12}\text{CH}_3\text{F}$ from extrapolation of the parameters in the $\nu_3=1$ and $\nu_3=2$ vibrational states (2). Then, frequencies of transitions in the $3\nu_3 - 2\nu_3$ hot band were calculated with the estimated parameters for the $\nu_3=3$ state and the known parameters for the $\nu_3=2$ state reported in ref. (2). It turns out that the frequencies estimated in this way provided a very good starting point for the observation and the assignment of the transitions in the $3\nu_3 - 2\nu_3$ hot band in $^{12}\text{CH}_3\text{F}$.

In order to determine the precise center frequencies of the pump and probe transitions a number of counterpropagating and copropagating three-level and four-level double resonance experiment were carried out. To get the double resonance effects for both configurations, one can record spectra for the counterpropagating and copropagating geometries separately, or use a mirror to reflect the pumping laser back into the sample cell. The advantage of the latter is that the double resonance effects for both configurations appear in the same spectrum. However, use of a mirror turned out to be difficult for a weak transition or for a large pump laser offset. The set up for the copropagating experiment is shown in figure 5.1.

The sample cell used in this work was a 1 m long Pyrex tube, 25 mm in diameter. All spectra were recorded at room temperature (~ 297 K) with the sample pressure in the range 5 - 40 mTorr.

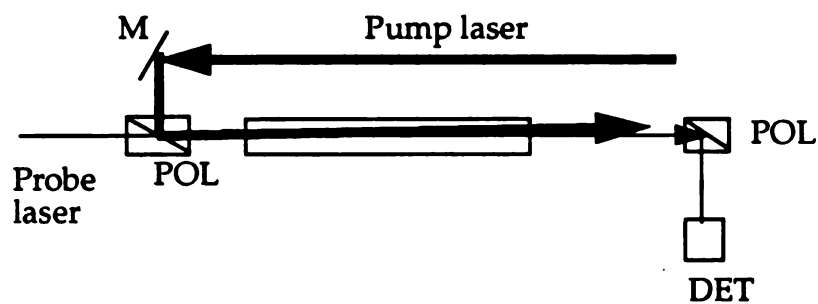


Figure 5.1. The geometry for the copropagating double resonance experiment. M = mirror; POL = polarizer; DET = detector. The planes of polarization of the pump and probe lasers were perpendicular to one another.

IV. Results and Discussion

A. Observation and assignment of the $3\nu_3 - 2\nu_3$ band in $^{12}\text{CH}_3\text{F}$

The experiment was first performed by pumping the $Q_R(13,6)$ transition in the $2\nu_3 - \nu_3$ band and scanning as wide a range as possible near the estimated frequencies of the $Q_R(10,6)$ and $Q_R(8,6)$ transitions in the $3\nu_3 - 2\nu_3$ band with the probe laser. Three double resonance effects with one showing a spike feature were observed ~ 2 GHz from the estimated frequency for each of the $Q_R(10,6)$ and the $Q_R(8,6)$ transitions. From our previous studies of double resonance line shapes in methyl fluoride, a probe transition with a spike feature in the line shape must have the same K quantum number as the pump transition (5,12,13). Thus, it was very reasonable to assign these six transitions as $Q_R(8,0)$, $Q_R(8,3)$, $Q_R(8,6)$ and $Q_R(10,0)$, $Q_R(10,3)$ and $Q_R(10,6)$ transitions in the $3\nu_3 - 2\nu_3$ band. However, we were not quite sure about the assignment of the J quantum numbers at the time since the assignment was just based on the fact that the observed spectra were closest to the estimated frequencies of the assigned transitions. It was not impossible that the rotational constants obtained from the extrapolation were so bad that the predicted frequencies were shifted by one or two J quantum numbers. In order to confirm the assignment, we investigated the same probe transitions with the $Q_R(7,3)$ pump in the $2\nu_3 - \nu_3$ band. This provided a very good test for the assignment. First, when the K quantum number for the pumped transition is 3, the spikes should appear in the $Q_R(8,3)$ and the $Q_R(10,3)$ probe transitions. Second, the $Q_R(7,3)$ pump in the $2\nu_3 - \nu_3$ band and the $Q_R(8,3)$ probe in the $3\nu_3 - 2\nu_3$ band is a three level double resonance combination. If the assigned J quantum number was correct then the double resonance line shape for the $Q_R(8,3)$ transition should have the features of a three-level double resonance line shape. It turned out that

the line shape of the $Q_R(8,3)$ probe did have much narrower line width and larger intensity than the $Q_R(10,3)$ transition indicating that our initial assignment was correct.

Figures 5.2 and Fig. 5.3 show the four-level double resonance spectra for the $Q_R(13,6)$ pump in the $2\nu_3 - \nu_3$ band and the $Q_R(8,6)$ and the $Q_R(10,6)$ probes in the $3\nu_3 - 2\nu_3$ band, respectively. Because the pumped level ($J=13, K=6$) has the same K quantum number as the probed levels in the $\nu_3=2$ vibrational state for both spectra, spike features are clearly seen in the double resonance line shapes. Also, since the J value of the $(10,6)$ rotational level is closer to the J value of the pumped level than the $(8,6)$ level in the $\nu_3=2$ state, the transferred spike is stronger in the $Q_R(10,6)$ than in the $Q_R(8,6)$ probe transition. Figures 5.4 and Fig. 5.5 show the double resonance spectra of the $Q_R(8,K)$ and $Q_R(10,K)$ ($K=0, 3, 6$) transitions in the $3\nu_3 - 2\nu_3$ hot band when the $Q_R(7,3)$ transition in the $2\nu_3 - \nu_3$ hot band was pumped. The $R(8,3)$ transition in Fig. 5.4 is a three-level double resonance spectrum which shows a much stronger and narrower spike than in the $Q_R(10,3)$ in Fig. 5.5. It is interesting to notice that the $Q_R(10,0)$ transition seems to be stronger than the $Q_R(10,6)$ while the $Q_R(8,0)$ transition seems to be weaker than the $Q_R(8,6)$. For the non-degenerate vibrational bands of $^{12}\text{CH}_3\text{F}$ the intensity of a rovibrational transition decreases with increasing K quantum number in the P and R branch and increases with increasing K in the Q branch for the same J . The appearance of the spectrum in Fig. 5.5 looks as if it belongs to a series of Q branch transitions. In fact, this did cast doubt on our assignment at first. As we found out later, the $Q_R(8,6)$ transition in the $3\nu_3 - 2\nu_3$ hot band is overlapped with the $Q_Q(9, 9)$ transition in the $2\nu_3 - \nu_3$ band of $^{12}\text{CH}_3\text{F}$. The double resonance effect of the latter is much stronger than that of the former. The mechanisms of the double resonance effects in the hot band of methyl fluoride will be discussed in more detail in later sections.

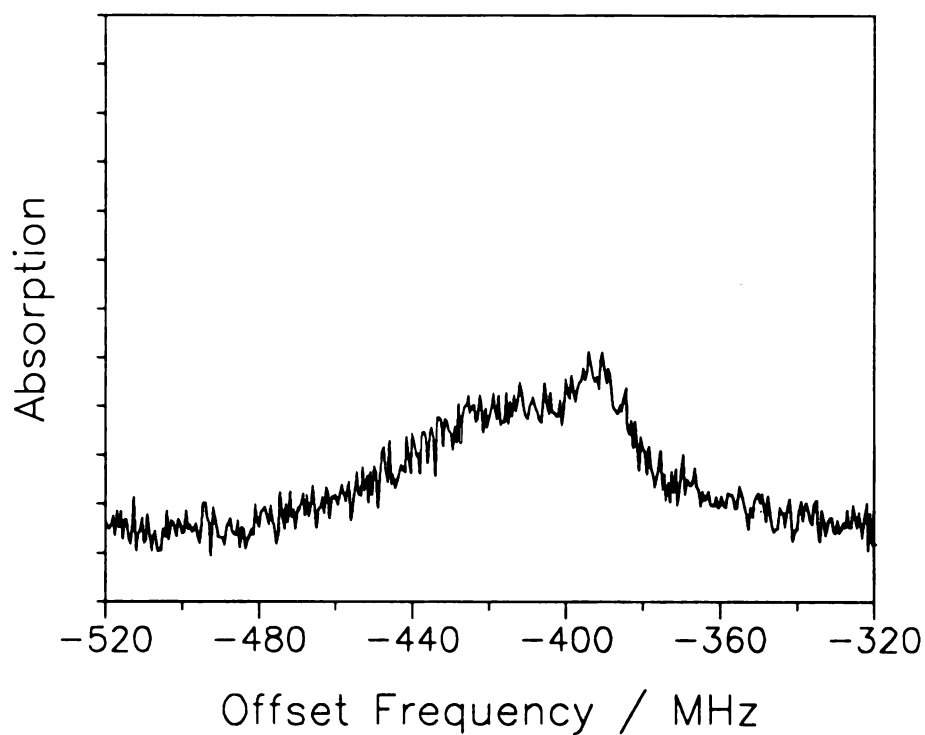


Figure 5.2. Four level double resonance spectrum for the $QR(8,6)$ transition in the $3\nu_3$ - $2\nu_3$ band in $^{12}\text{CH}_3\text{F}$. The $QR(13,6)$ transition in the $2\nu_3$ - ν_3 band was pumped. The horizontal axis is the offset frequency of the probe laser with the GHz part removed. The pump and probe lasers used are given in Tables 5.1 and 5.2, respectively.

TABLE 5.2
Comparison of Observed and Calculated Frequencies in $^{12}\text{CH}_3\text{F}$

Transition	ν / MHz	O-C ^b	Unc. ^c	Offset ^d	Laser
Transitions in the $3\nu_3 - 2\nu_3$ hot band ^a					
$Q_R(8,0)$	30909808.2	0.65	2.0	-13107.2	$^{12}\text{C}^{16}\text{O}_2$ 9P(36)
$Q_R(8,3)$	30909961.8	-0.04	0.5	-12953.2	$^{12}\text{C}^{16}\text{O}_2$ 9P(36)
$Q_R(8,6)$	30910490.7	0.05	2.0	-12427.7	$^{12}\text{C}^{16}\text{O}_2$ 9P(36)
$Q_R(10,0)$	30995912.5	-0.65	2.0	12721.8	$^{12}\text{C}^{16}\text{O}_2$ 9P(34)
$Q_R(10,3)$	30996039.7	0.04	0.5	12849.4	$^{12}\text{C}^{16}\text{O}_2$ 9P(34)
$Q_R(10,6)$	30996480.3	-0.05	2.0	13289.1	$^{12}\text{C}^{16}\text{O}_2$ 9P(34)
Pure Rotational Transitions in the $\nu_3=3$ Vibrational State ^e					
$Q_R(4,0)$	245525.700	0.018	0.1		
$Q_R(4,1)$	245519.698	0.011	0.1		
$Q_R(4,2)$	245501.621	-0.041	0.1		
$Q_R(4,3)$	245471.505	0.012	0.1		

^aObserved in this study.

^bObserved minus calculated frequencies in MHz. The parameters used for the calculation are in Table 5.3. The Laser frequencies were calculated from the constants in References (24) and (25).

^cEstimated uncertainty in the observed frequency in MHz.

^dCenter frequency of the transition minus the CO_2 laser frequency in MHz.

^e Measured in De Lucia's laboratory (26).

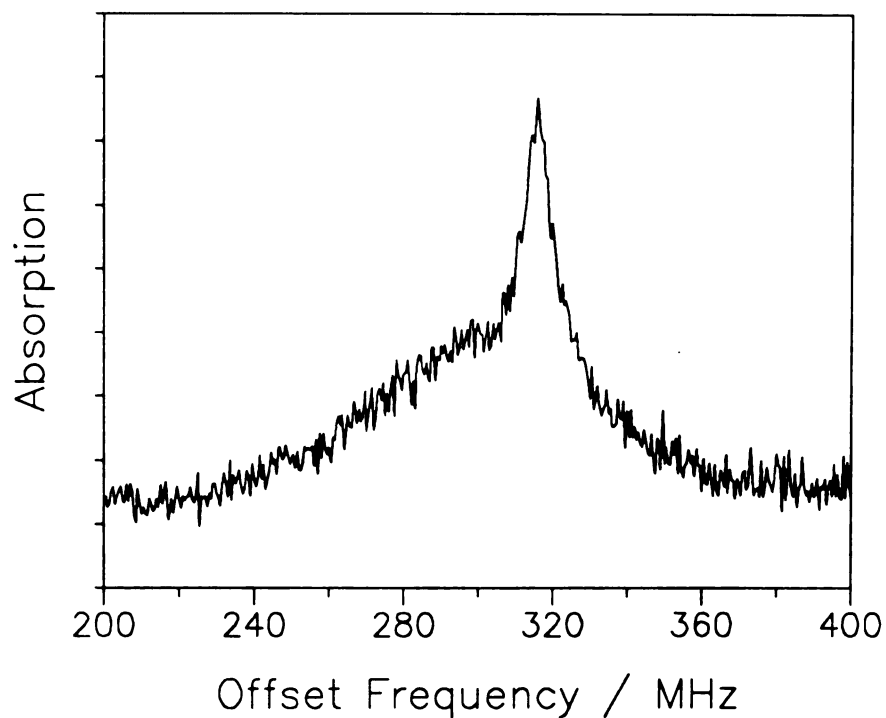


Figure 5.3. Four level double resonance spectrum for the $QR(10,6)$ transition in the $3v_3$ - $2v_3$ band in $^{12}CH_3F$. The $QR(13,6)$ transition in the $2v_3$ - v_3 band was pumped. The horizontal axis is the offset frequency of the probe laser with the GHz part removed. The pump and probe lasers used are given in Tables 5.1 and 5.2, respectively.

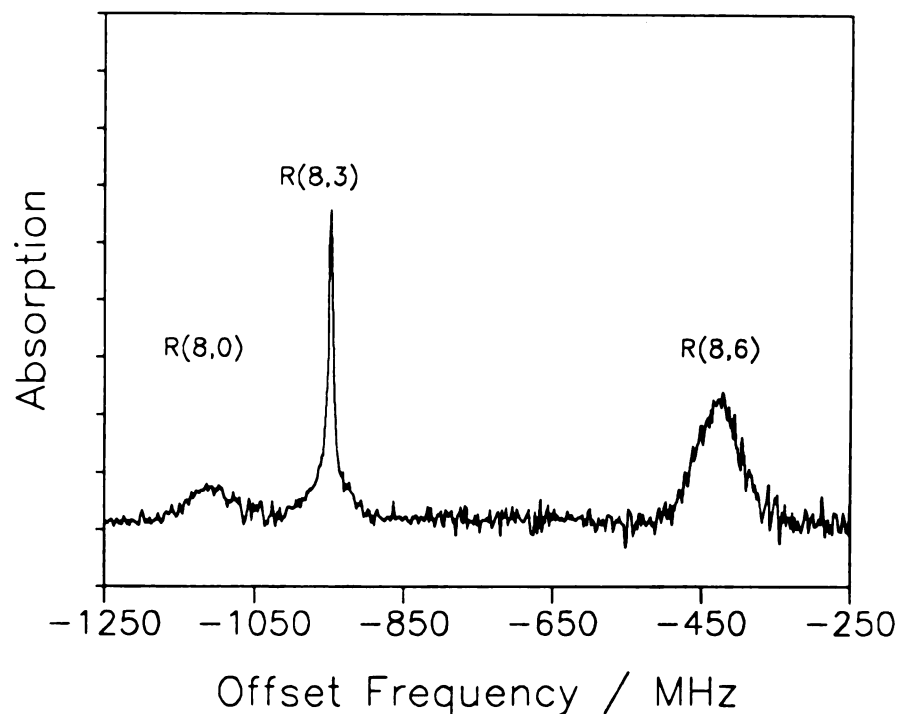


Figure 5.4. Double resonance spectrum for the $\text{QR}(8,0)$, $\text{QR}(8,3)$ and $\text{QR}(8,6)$ transitions in the $3\nu_3-2\nu_3$ band in $^{12}\text{CH}_3\text{F}$. The $\text{QR}(7,3)$ transition in the $2\nu_3-\nu_3$ band was pumped.

The horizontal axis is the offset frequency of the probe laser with the GHz part removed.

The pump and probe lasers used are given in Tables 5.1 and 5.2, respectively. The $\text{QR}(8,6)$ transition is overlapped with the $\text{QR}(9,9)$ transition in the $2\nu_3-\nu_3$ band.

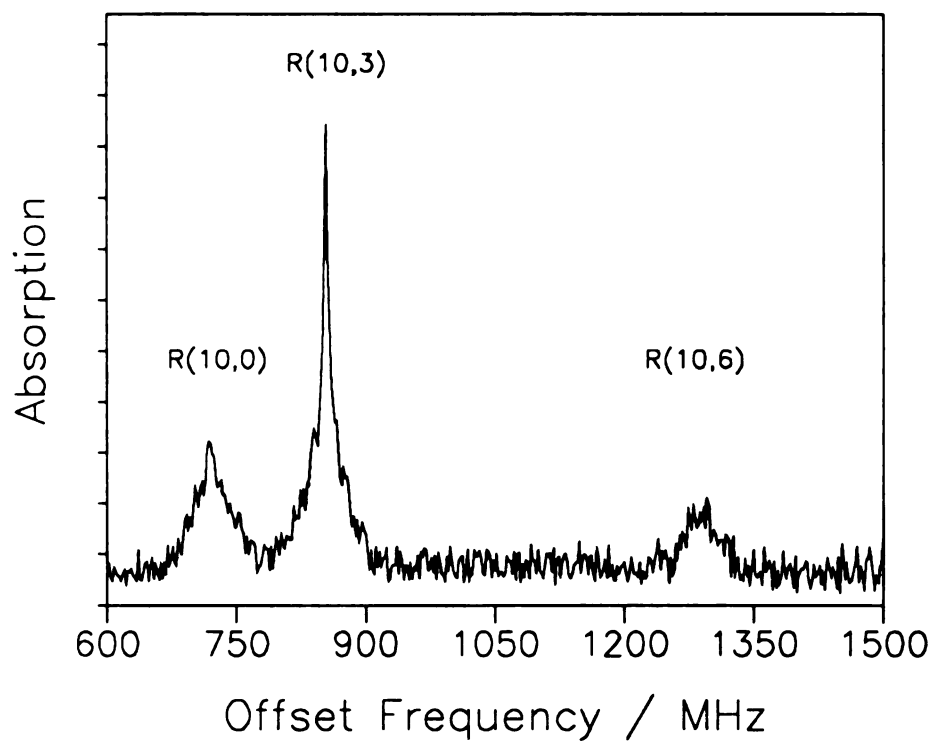


Figure 5.5. Four level double resonance spectrum for the $QR(10,0)$, $QR(10,3)$ and $QR(10,6)$ transitions in the $3\nu_3-2\nu_3$ band in $^{12}\text{CH}_3\text{F}$. The $QR(7,3)$ transition in the $2\nu_3-\nu_3$ band was pumped. The horizontal axis is the offset frequency of the probe laser with GHz part removed. The pump and probe lasers used are given in Tables 5.1 and 5.2, respectively.

B. Rotational constants in the $v_3=3$ vibrational state of $^{12}\text{CH}_3\text{F}$

From the frequencies of the assigned transitions in the $3v_3 - 2v_3$ hot band the major molecular constants for the $v_3=3$ vibrational level in $^{12}\text{CH}_3\text{F}$ can be determined. Since the number of frequencies measured is relatively small, a couple of very accurate transition frequencies can substantially improve the molecular constants from the least squares fit. As has been seen, four of the six double resonance spectra observed have a Doppler free feature in the line shape (spike). Thus, more accurate transition frequencies (compared with Doppler limited spectroscopy) can be obtained, provided that accurate pump laser offsets are known. Unfortunately neither of the pump laser offsets had been accurately determined. Therefore, for this purpose, we recorded three-level double resonance effects for the $Q_R(7,3)$ pump in the $2v_3 - v_3$ band and the $Q_R(8,3)$ probe in the $3v_3 - 2v_3$ band for both copropagating and counterpropagating geometries of the pump and probe beams. In this experiment, a reflecting mirror was used to reflect the pump beam back into the sample cell so that double resonance effects for both geometries could be recorded in the same scan. Figure 5.6 shows the corresponding spectrum. The copropagating component is much weaker than the counterpropagating component because the pumping laser power for the copropagating geometry was much smaller than for the counter-propagating geometry as a result of absorption by the sample and losses during reflection. The two spikes were each fit to a Lorentz lineshape by the method of least squares and the frequencies obtained from the fitting were used to calculate the pump laser offset and the precise center frequencies of the $Q_R(8,3)$ and the $Q_R(10,3)$ transitions in the $3v_3 - 2v_3$ hot band by the procedure described in the Theoretical part.

The center frequencies of the $Q_R(8,6)$ and the $Q_R(10,6)$ transitions were obtained by least squares fitting the four-level double resonance spectra, shown in Fig. 5.2 and Fig. 5.3, with a computer program that was developed to calculate the

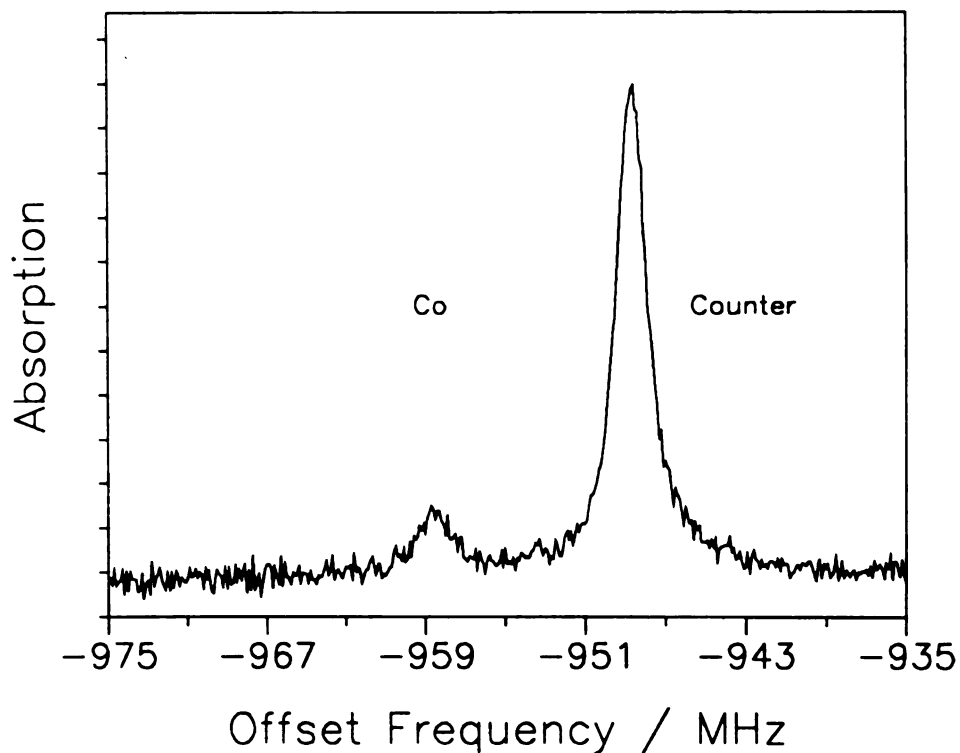


Figure 5.6. Three-level double resonance spectrum for the $QR(7,3)$ pump transition in the $2\nu_3-\nu_3$ band and the $QR(8,3)$ probe in the $3\nu_3-2\nu_3$ band in $^{12}\text{CH}_3\text{F}$. The spectrum was recorded with a setup with which double resonance effects for both counter-propagating and copropagating pump beams could be seen in the same scan. The horizontal axis is the offset frequency of the probe laser with the GHz part removed. The pump and probe lasers used are given in Tables 5.1 and 5.2, respectively.

center frequency of the probe transition and the half width of the transferred spikes for the four-level double resonance line shape. Although the observed double resonance spectra are Doppler free, the accuracy of the center frequencies determined depends on the accuracy of the center frequency of the pump transition—the $Q_R(13,6)$ transition in the $2\nu_3 - \nu_3$ band, which was determined by Doppler limited spectroscopy. The frequencies for the $Q_R(8,0)$ and the $Q_R(10,0)$ transitions were obtained by least squares fitting each double resonance line shape with a Gaussian function. The frequencies for all six of the observed transitions in the $3\nu_3 - 2\nu_3$ band are listed in Table 5.2. These frequencies, together with the frequencies of several pure rotational transitions in the $\nu_3=3$ vibrational state measured in De Lucia's laboratory (26), were least squares fit to Eqs. (5.1) and (5.2) to obtain the molecular constants for the $\nu_3=3$ vibrational state in $^{12}\text{CH}_3\text{F}$ reported in Table 5.3.

In the least-squares fitting the parameters of the $\nu_3=2$ state of $^{12}\text{CH}_3\text{F}$ were constrained to the values reported in Ref. (2). Because the number of frequencies observed were limited, only the molecular constants E_v , B_v , $A_v - B_v$, $D_J^{(v)}$, $D_{JK}^{(v)}$, and ΔD_K in the $\nu_3=3$ vibrational state were adjusted in the least squares fit. Several ways of treating the other high order molecular constants in the fitting were tested. The first test was to constrain the high order constants to the values obtained from linear extrapolation of the constants in the $\nu_3=1$ and the $\nu_3=2$ vibrational states. The second test was to constrain the constants to the values of the corresponding constants in the $\nu_3=2$ vibrational state. Finally, the constants were constrained to zero. It turned out that linear extrapolation of the high order molecular constants gave the best fit. The molecular constants for the $\nu_3=3$ vibrational state in $^{12}\text{CH}_3\text{F}$ determined from this study are listed in Table 5.3.

TABLE 5.3

Vibration-Rotation Parameters for the $3\nu_3 - 2\nu_3$ Band in $^{12}\text{CH}_3\text{F}$

Parameter	$\nu_3=2$ ^a	$\nu_3=3$ ^b
E_v /GHz	62398.208	92888.904
B_v /MHz	24870.982	24555.114
$\Delta(A_v-B_v)$ /MHz	81.301	110.278
D_J /kHz	53.449	50.438
D_{JK} /kHz	576.153	604.045
D_K /kHz	169.646	-247.974
H_J /Hz	6.671	-13.107
H_{JK} /Hz	57.665	99.484
H_{KJ} /Hz	-207.750	-323.159
H_K /Hz	172.75	239.056
L_J /mHz	8.384	16.7051
L_{JJJK} /mHz	-46.501	-90.132
L_{JJKK} /mHz	106.803	172.376
L_{JKKK} /mHz	-238.59	-239.889
L_K /mHz	142.613	130.219

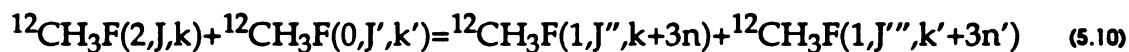
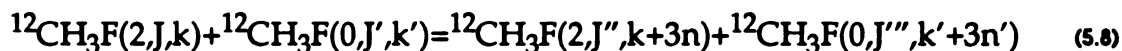
^aTaken from ref. (2).

^bThe first six parameters are obtained from the least squares fit and all the others are from linear extrapolation (see text).

C. Collisionally induced energy transfer in the $v_3=2$ state

It is very interesting to notice that in Fig. 5.4 and Fig. 5.5 the double resonance effects are only observed in the rotational levels with $K=0, 3, 6$ in the $v_3=2$ vibrational state when the rotational level with $K=3$ in the same state is pumped. This indicates that the collisionally-induced energy transfer within the $v_3=2$ vibrational state is dominated by the direct rotational energy transfer process for methyl fluoride self-collisions. The effect of the near resonant vibration-vibration swapping is negligible. Collisionally induced energy transfer within the $v_3=1$ vibrational state of methyl fluoride has been discussed in Chapter 3 and in ref. (12,13). We have found that in the $v_3=1$ vibrational state, near resonant vibrational swapping plays an important role for energy transfer. Although the result of this experiment was unexpected to us at first, careful analysis of the energy transfer process can explain our observation very well.

The molecules pumped into the $(v_3=2, J, k)$ rovibrational state of $^{12}\text{CH}_3\text{F}$ can undergo three process:



On both sides of the above equations, the first molecules are colliders (molecules pumped) while the second molecules are perturbers. The first process represents collisionally induced direct rotational energy transfer among the rotational levels within the $v_3=2$ vibrational state, which obeys the $\Delta k = 3n$ selection rule. The second and third processes describe vibrational swapping, where the colliding partners exchange vibrational energies and find themselves in different vibrational states. These two processes do not obey the k selection rules. For the

experimental conditions in Fig. 5.4 and 5.5, only the results of the first and second processes can be seen, since it is the rotational levels in the $v_3=2$ vibrational state that are probed. Therefore, although the third process can be very fast, it does not contribute to the spectra shown in the figures. However, the fact that only the transitions with $k=3+3n$ or $k=6+3n$ in the $3v_3 - 2v_3$ band are observed indicates that the second process is very slow, which is understandable if the near resonant vibration-vibration transfer obeys the dipole selection rule ($\Delta v = \pm 1$ for each collision partner).

As is mentioned earlier, the $Q_Q(9, 9)$ transition in the $2v_3 - v_3$ band is overlapped with the $Q_R(8,6)$ transition in the $3v_3 - 2v_3$ band. The double resonance effect of the $Q_Q(9,9)$ probe transition is worth examining since it is an example of a double resonance where both the pump and probe are in the $2v_3 - v_3$ hot band. In this case, the effects of the both collisionally-induced direct rotational energy transfer (process (5.8)) and the V-V process (process(5.10)) can contribute to the double resonance spectra. However, the direct rotational energy transfer increases the population of the upper level and decreases the population of the lower level of the probe while the V-V process only increases the population of the lower level of the probe. Therefore, the contributions of the two processes do not both increase the intensity of a double resonance effect but tend to cancel each other. Which process will win depends on which process is faster. It appears from Fig. 5.4 that the V-V process dominates. Figure 5.7 shows the double resonance spectra in $^{12}\text{CH}_3\text{F}$ for the $Q_Q(9,K)$ ($K=3, 4, 5, 6$) transitions in the $2v_3 - v_3$ hot band while the $Q_R(7,3)$ transition in the same band is pumped. The transferred spike in the $Q_Q(9,3)$ transition has an opposite sign compared with the other transitions indicating that the direct rotational energy transfer process for $\Delta K = 0$ is faster than the V-V transfer, but that rotational energy transfer for $\Delta K = \pm 3n$ ($n > 0$) is slower than the vibrational swapping process.

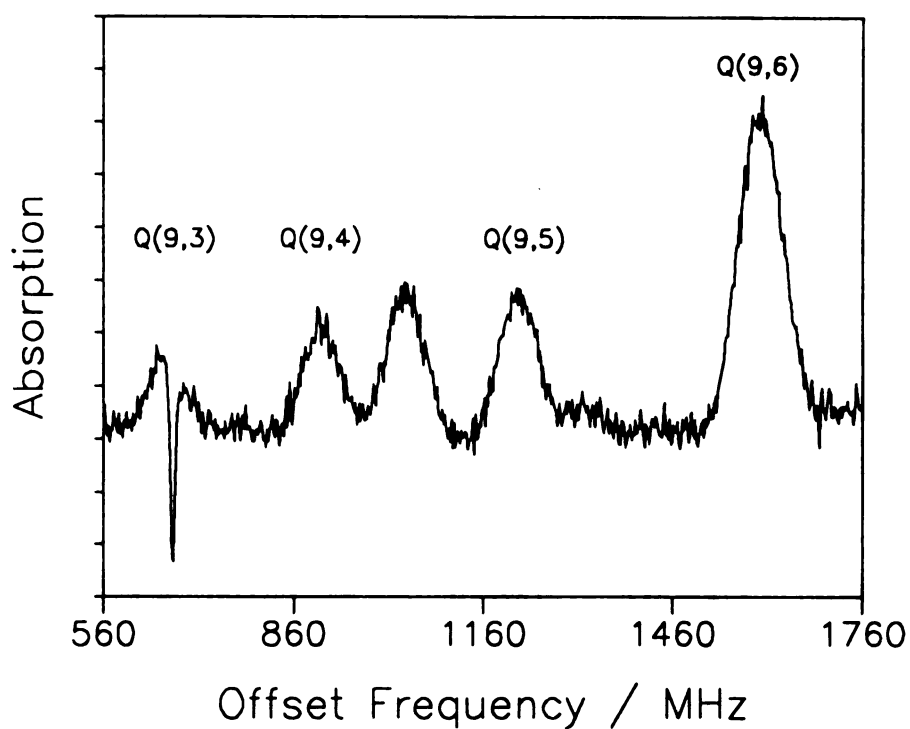


Figure 5.7. Double resonance spectrum for the $QQ(9,K)$ ($K=3, 4, 5, 6$) transitions in the $2\nu_3-\nu_3$ band in $^{12}\text{CH}_3\text{F}$. The $QR(7,3)$ transition in the $2\nu_3-\nu_3$ band was pumped. The horizontal axis is the offset frequency of the probe laser with the GHz part removed. The pump and probe lasers used are given in Table 5.1.

D. Precise frequencies in CH₃F

The $^Q Q(12, 1)$ and $^Q Q(12, 2)$ transitions in the ν_3 band of $^{12}\text{CH}_3\text{F}$, and the $^Q R(4,3)$ transition in the ν_3 band of $^{13}\text{CH}_3\text{F}$ are the most commonly used transitions for optical pumping in the study of laser induced phenomena in methyl fluoride. Prior to the present study, the best values for the frequencies of the $^Q Q(12, 1)$ and $^Q Q(12, 2)$ transitions in the ν_3 band of $^{12}\text{CH}_3\text{F}$ were measured by a wave guide laser Lamb dip technique and the reported accuracy was ± 0.5 MHz (17). In the work described in Chapter 4, we found it desirable to know pump laser offset frequencies to within ± 0.1 MHz. This can be achieved by measuring the frequency of the pump transition to within ± 0.1 MHz if the pump laser has been precisely calibrated. If the pump laser frequency is not precisely calibrated, the frequencies of both pump and probe transitions need to be measured to within that accuracy. By using counterpropagating and copropagating three-level infrared-infrared double resonance techniques, the frequencies of both pump and probe transitions can be easily determined to within an accuracy of ± 0.1 MHz.

Figure 5.8 shows the copropagating and counterpropagating three-level double resonance spectra for the $^Q R(12,1)$ and $^Q R(12, 2)$ probe transitions in the $2\nu_3 - \nu_3$ hot band when the $^Q Q(12,1)$ and $^Q Q(12,2)$ transitions in the ν_3 fundamental of $^{12}\text{CH}_3\text{F}$ are simultaneously pumped by the 9P(20) $^{12}\text{CO}_2$ laser. The spikes for the $^Q Q(12, 1)$ transition are much weaker than for $^Q Q(12, 2)$ transition because the pump offset for $^Q Q(12,1)$ is much larger than that for $^Q Q(12, 2)$. As a result, a substantially smaller number of molecules can be pumped into the probed level in the former case than in the latter. Each of the four spikes in Fig. 5.8 was recorded 5 times with a narrow band scan and the line shape was fit to a Lorentz function. The center frequencies from the fitting were averaged to obtain the final frequency of the spike. The values obtained in this way were used to determine the center frequencies of the pump and probe transitions and the pump laser offsets.

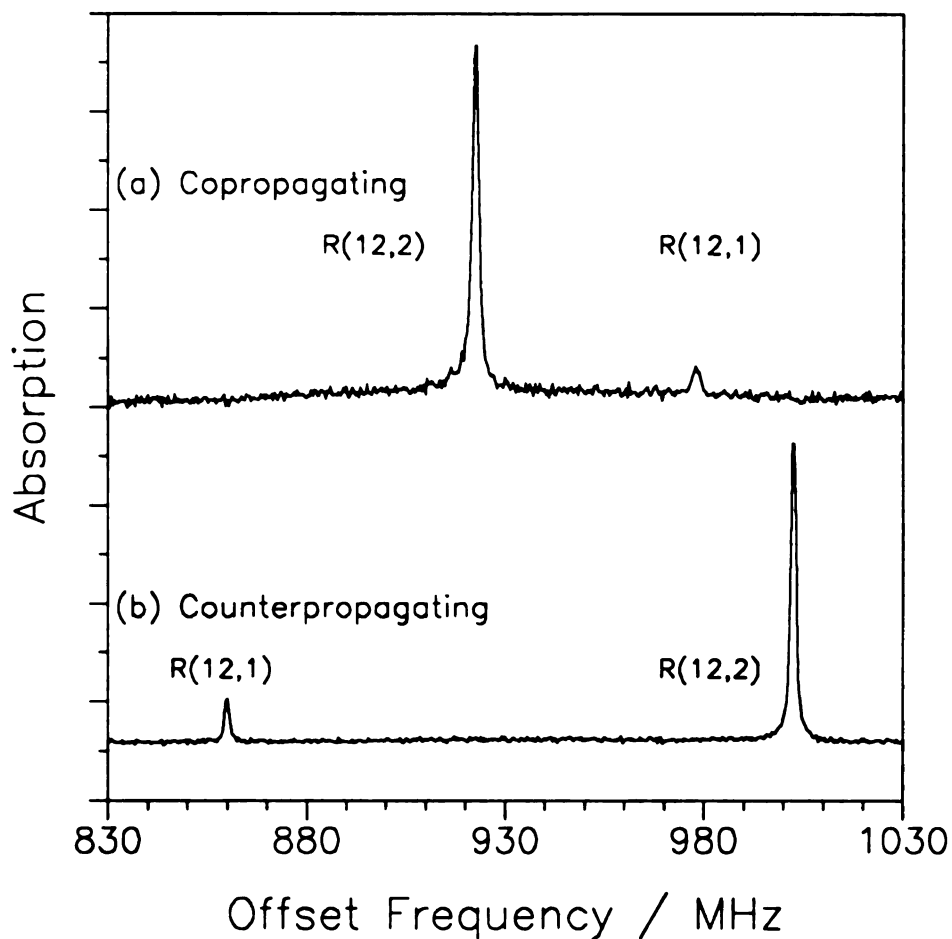


Figure 5.8. Counterpropagating and copropagating three-level double resonance spectra for the $QR(12,1)$ and $QR(12,1)$ transitions in the $2\nu_3-\nu_3$ band when the $QQ(12,1)$ and the $QQ(12,2)$ transitions in the ν_3 fundamental in $^{12}\text{CH}_3\text{F}$ are simultaneously pumped by 9P(20) $^{12}\text{CO}_2$ laser. The horizontal axis is the offset frequency of the probe laser with the GHz part removed.

TABLE 5.4

Precise Frequencies of Transitions in CH₃F

Transition	Band	Frequency ^a	Offset ^b	Laser
¹² CH ₃ F				
^Q Q(12,1)	ν_3	31 383 841. 69	-58. 72	¹² C ¹⁶ O ₂ 9P(20)
^Q Q(12,2)	ν_3	31 383 940. 19	39. 78	¹² C ¹⁶ O ₂ 9P(20)
^Q R(12,1)	$2\nu_3 - \nu_3$	31 556 947. 84	12 918. 96	¹² C ¹⁶ O ₂ 9P(14)
^Q R(12,2)	$2\nu_3 - \nu_3$	31 556 991. 49	12 962. 61	¹² C ¹⁶ O ₂ 9P(14)
¹³ CH ₃ F				
^Q R(4,3))	ν_3	31 042 693. 80	-24. 26	¹² C ¹⁶ O ₂ 9P(32)
^Q P(5,3)	$2\nu_3 - \nu_3$	30 092 980. 48	-14 572. 61	¹³ C ¹⁶ O ₂ 9P(16)
^Q P(6,3)	$2\nu_3 - \nu_3$	30 040 821. 28	-12 707. 45	¹³ C ¹⁶ O ₂ 9P(18)
^Q P(7,3)	$2\nu_3 - \nu_3$	29 988 049. 41	-10 600. 68	¹³ C ¹⁶ O ₂ 9P(20)

^aCenter frequency of the transition in MHz determined in this work. Estimated absolute accuracy is ± 0.1 MHz.

^bCenter frequency of the transition minus the CO₂ laser frequency in MHz. Laser frequencies calculated from the constants in References (24) and (25).

Similar measurements were also carried out in $^{13}\text{CH}_3\text{F}$ for the $^{\text{Q}}\text{R}(4,3)$ pump in the ν_3 band and the $^{\text{Q}}\text{P}(5,3)$, $^{\text{Q}}\text{P}(6,3)$, $^{\text{Q}}\text{P}(7,3)$ and $^{\text{Q}}\text{P}(8,3)$ probes in the $3\nu_3 - 2\nu_3$ hot band. The obtained Doppler-free frequencies are shown in Table 5.4.

Since the halfwidths at half height for the spikes observed in the experiments are less than 1 MHz, the center frequencies of the spikes can be determined to within ~ 0.02 MHz. However, a slight misalignment between the pump and probe beams can result in a discrepancy of the velocity components between the molecules pumped and molecules probed. This discrepancy can cause a shift in frequency for the spike in the three level double resonance spectra. Careful alignment can reduce the uncertainty to within ± 0.05 MHz. In fact, the frequencies of the spikes recorded in the same day are reproducible to within ± 0.02 MHz and on different days with different alignments are reproducible to within ± 0.05 MHz. The overall uncertainty in the absolute frequencies determined in this work is estimated to be $\sim \pm 0.1$ MHz, which is approximately one order of magnitude smaller than the values obtained from the previous experiment. A comparison of the frequencies determined from this work to that of previous work is shown in Table 5.5.

V. Conclusion

We have observed and assigned six transitions in the $3\nu_3 - 2\nu_3$ hot band of $^{12}\text{CH}_3\text{F}$ by infrared-infrared double resonance. The molecular constants for the $\nu_3=3$ vibrational state of $^{12}\text{CH}_3\text{F}$ have been obtained for the first time. These constants can provide frequencies for transitions in the $3\nu_3 - 2\nu_3$ hot band of $^{12}\text{CH}_3\text{F}$ with sufficient accuracy for reliable assignment. We have also measured laser pump frequency offsets for the $^{\text{Q}}\text{Q}(12,1)$ and $^{\text{Q}}\text{Q}(12,2)$ transitions in the ν_3 fundamental of $^{12}\text{CH}_3\text{F}$ to ± 0.1 MHz, which is one order of magnitude higher accuracy than the previously-reported values. The center frequencies for the

TABLE 5.5

Comparison of Frequencies of Transitions in CH₃F

¹² CH ₃ F				
Method	Q _Q (12,1) ^a	Q _Q (12,2) ^a	Q _R (12,1) ^b	Q _R (12,2) ^b
This work	31383841.69	31383940.19	31556947.84	31556991.49
Waveguide laser Lamb dip ^c	31383841.4	31383938.5		
IR-MW sideband laser ^d	31383841.7	31383940.1	31556957.2	31557000.4
FTIR ^e	31383843.4	31383942.0	31556949.7	31556993.6
¹³ CH ₃ F				
Method	Q _R (4,3) ^a	Q _P (5,3) ^b	Q _P (6,3) ^b	Q _P (7,3) ^b
This work	31 042 693. 80	30 092 980. 48	30 040 821. 28	29 988 049. 41
IR-MW sideband laser ^f	31 042 692. 24	30 092 976.1	30 040 816. 7	29 988 045. 1

^aCenter frequency of transition in the ν_3 band in MHz.^bCenter frequency of transition in the $2\nu_3 - \nu_3$ band in MHz.^cRef. (17).^dRef. (2).^eRef. (15).^fRef. (1)

$Q_R(12,1)$ and $Q_R(12,2)$ transitions in the $2\nu_3 - \nu_3$ hot band have also been determined to this accuracy. This work demonstrated further the usefulness and extremely high sensitivity of the double resonance technique for observation and assignment of very weak transitions, even though in a highly excited vibrational state.

References

1. S. K. Lee, R. H. Schwendeman, and G. Magerl, *J. Mol. Spectrosc.* **117**, 416-434 (1986).
2. S. K. Lee, R. H. Schwendeman, R. L. Crownover, D. D. Skatrud, and F. C. DeLucia, *J. Mol. Spectrosc.* **123**, 145-160 (1987).
3. J. M. Preses and G. W. Flynn, *J. Chem. Phys.* **66**, 3112-3116 (1977).
4. R. S. Sheorey and G. W. Flynn, *J. Chem. Phys.* **72**, 1175-1186 (1980).
5. Q. Song and R. H. Schwendeman, *J. Mol. Spectrosc.* **153** (1992).
6. W. H. Matteson and F. C. De Lucia, *IEEE J. Quantum Electron.* QE-19, 1284 (1983).
7. R. I. McCormick, F. C. De Lucia, and D. D. Skatrud, *IEEE J. Quantum Electron.* QE-23, 2060 (1987).
8. R. I. McCormick, H. O. Everitt, F. C. De Lucia, and D. D. Skatrud, *IEEE J. Quantum Electron.* QE-23, 2069 (1987).
9. Q. Song and R. H. Schwendeman, *J. Mol. Spectrosc.* **149**, 356-374 (1991).
10. P. L. Chapovsky, A. M. Shalagin, V. N. Panfilov, and V. P. Strunin, *Opt. Comm.* **40**, 129-134 (1981).
11. P. L. Chapovsky, L. N. Krasnoperov, V. N. Panfilov, and V. P. Strunin, *Chem. Phys.* **97**, 449-455 (1985).
12. Y. Matsuo and R. H. Schwendeman, *J. Chem. Phys.* **91**, 3966-3975 (1989).
13. U. Shin, Q. Song, and R. H. Schwendeman, *J. Chem. Phys.* **95**, 3964-3974 (1991).
14. U. Shin and R. H. Schwendeman, *J. Chem. Phys.* **94**, 7560-7561 (1991).

15. H. G. Cho, Y. Matsuo, and R. H. Schwendeman, *J. Mol. Spectrosc.* 137, 215-229 (1989).
16. D. Papousek, J. F. Ogilvie, S. Civis, and M. Winnewisser, *J. Mol. Spectrosc.*, 149, 109-124 (1991).
17. S. M. Freund, G. Duxbury, M. Romheld, J. T. Tiedje, and T. Oka, *J. Mol. Spectrosc.* 52, 38-57 (1974).
18. F. Herlemont, M. Lyszak, J. Lemaire, and J. Demaison, *Z. Naturforsch.* 36a, 944-947 (1987).
19. M. Romheld, Ph.D thesis, University of Ulm. 1979.
20. J. K. G. Watson, S. C. Foster, A. R. W. McKellar, P. Bernath, T. Amano, F. S. Pan, M. W. Crofton, R. S. Altman, and T. Oka, *Canad. J. Phys.* 62, 1875-1885 (1984).
21. P. Shoja-Chaghervand and R. H. Schwendeman, *J. Mol. Spectrosc.* 98, 27-40 (1983).
22. W. Demtroder, *Laser Spectroscopy*, edited by F. P. Schafer (Springer Series in Chemical Physics 5, 1982), pp. 86.
23. C. Freed and A. Javan, *Appl. Phys. Lett.* 17, 53-56 (1970).
24. F. R. Petersen, E. C. Beaty, and C. R. Pollock, *J. Mol. Spectrosc.* 102, 112-1122 (1983).
25. C. Freed, L. C. Bradley, and R. G. O'Donnell, *IEEE J. Quantum Electron.* QE-16, 1195-1206 (1980).
26. T. M. Goyette and F. C. De Lucia, private communication.

MICHIGAN STATE UNIV. LIBRARIES



31293010553281